Functional interfaces: Polymer brushes and their response to temperature and hydrostatic pressure

D i s s e r t a t i o n

zur Erlangung des akademischen Grades

d o c t o r r e r u m n a t u r a l i u m

(Dr. rer. nat.)

im Fach Physik

eingereicht an der

Mathematisch-Naturwissenschaftlichen Fakultät I
der Humboldt-Universität zu Berlin

von

Herr Dipl.-Phys. Matthias Reinhardt

Präsident der Humboldt-Universität zu Berlin
Prof. Dr. Jan-Hendrik Olbertz

Dekan der Mathematisch-Naturwissenschaftlichen Fakultät I
Prof. Dr. Stefan Hecht

Gutachter: Prof. Dr. Matthias Ballauff
Prof. Dr. Jürgen P. Rabe
Prof. Dr. Claus Czeslik

Tag der mündlichen Prüfung: 13.12.2013

Summary

The functionality of an interface can be modified by polymer brushes. Out of the variety of polymers which can be used to achieve this functional modification, the focus of this work is on brushes of either polyacrylic acid (PAA) or poly(N,N-dimethylaminoethyl methacrylate) (PDMAEMA). PAA brushes provide a soft interface that prevents the denaturation of adsorbed proteins. PDMAEMA is known to respond to external stimuli. The lower critical solution temperature (LCST) of PDMAEMA can be used to tune the hydrophobicity of the interface with temperature. For the first time, the effect of elevated hydrostatic pressure, up to 1000 bar, on the functionality of these systems is investigated.

Planar PAA and PDMAEMA brushes are prepared from precursor diblock copolymer Langmuir layers with varied grafting density σ utilizing the Langmuir-Schäfer transfer technique. For the PAA brushes, neutron reflectivity (NR) measurements are conducted in the solvent-swollen state at the solid-liquid interface after incubation in buffered D_2O and after the adsorption of bovine serum albumin (BSA) from the aqueous liquid phase at 1 bar and 900 bar. From these measurements the detailed volume fraction profiles of the PAA brush $\varphi_{PAA}(z)$ and adsorbed BSA proteins $\varphi_{BSA}(z)$ are extracted. The amount of adsorbed BSA is found to scale linearly with grafting density. An elevated hydrostatic pressure of 900 bar is found to have no impact on the structure of the PAA brush and its capability to bind BSA proteins.

The PDMAEMA brushes are investigated by NR at the solid-liquid interface in a temperature range of 20 to 60 °C for hydrostatic pressures from 1 to 1000 bar. A novel theoretical model of the brush density profile as a function of σ, T and P is used to fit the experimental NR data. Increasing the temperature causes a continuous decrease of the polymer brush thickness. The reason for this response is a hydrophobic coil to globule transition of the polymer chains when crossing the LCST. Hydrostatic pressure is found to act antagonistic to temperature. The hydrophobic collapse of the PDMAEMA brush that is caused by a temperature increase of 10 K is counterbalanced by a pressure increase of 1000 bar. While the value of the LCST of the polymer brush is found to decrease with the grafting density, the antagonistic effect of hydrostatic pressure is not affected.

Zusammenfassung

Viele Polymere können bei Verankerung auf einer Oberfläche deren Funktionalität beeinflussen. Der Schwerpunkt dieser Arbeit liegt auf der Untersuchung von Polymerbürsten aus Polyacrylsäure (PAA) und Poly(N,N-dimethylaminoethyl methacrylat) (PDMAEMA). Auf Oberflächen, die mit PAA Bürsten beschichtet sind, können Proteine adsorbieren, ohne im immobilisierten Zustand zu denaturieren. Für PDMAEMA ist eine Reaktion auf externe Reize bekannt. So kann die untere kritische Lösungstemperatur (LCST) von PDMAEMA zur Einstellung der Hydrophobizität von Oberflächen verwendet werden. Erstmalig im Rahmen dieser Arbeit wurde untersucht, wie sich hydrostatischer Druck von bis zu 1000 bar auf die Funktionalität der verwendeten Polymerbürsten auswirkt.

Aus Diblock-Kopolymeren wurden Langmuir-Filme unterschiedlicher Ankerdichte σ mit der Langmuir-Schäfer Technik auf feste Substrate übertragen. Die Funktionalität der so präparierten PAA Bürsten wurde vor und nach der Adsorption von Rinderserumalbumin (BSA) in gepufferter D_2O-Lösung mit Hilfe der Neutronenreflektometrie (NR) bei 1 bar und 900 bar an der fest-flüssig Grenzfläche untersucht. Es wurden Volumenfraktionsprofile der PAA Bürste und adsorbierten BSA extrahiert, woraus sich eine lineare Abhängigkeit zwischen Ankerdichte und Menge an adsorbiertem Protein feststellen ließ. Erhöhung des hydrostatischen Druckes auf 900 bar veränderte weder die Volumenprofile der PAA Bürsten noch die Immobilisierung von BSA.

Die PDMAEMA Bürsten wurden mittels NR bei Temperaturen von 20-60 °C und hydrostatischen Drücken von 1-1000 bar untersucht. Zur Analyse der Daten in Abhängigkeit der Parameter σ, T und P wurde ein neuartiges Dichteprofil-Modell verwendet. Mit Erhöhung der Temperatur wurde eine stetige Abnahme der Bürstendicke gefunden. Dies lässt sich durch den LCST induzierten Phasenübergang der Polymere vom hydrophilen in einen hydrophoben Zustand erklären. Es wurde gefunden, dass eine Erhöhung des hydrostatischen Druckes diesem Prozess entgegenwirkt. Strukturänderungen der Polymerbürsten bei Erhöhung der Temperatur um 10 K ließen sich durch Erhöhung des Druckes um 1000 bar rückgängig machen. Während für höhere Ankerdichten eine Senkung der LCST festgestellt wurde, ist der antagonistische Effekt zwischen Temperatur und Druck davon unbeeinflusst.

Contents

CHAPTER 1

Introduction

Polymer brushes are formed when long polymers are fixed at one end to a surface [1, 2]. At sufficient density the single polymer random coil conformations overlap and the polymer chains stretch away from the grafting interface. As any polymer system, dependent on their chemical architecture, polymer brushes can respond to external stimuli like changes in temperature [3, 4], pH [5, 6] or the ionic strength of the surrounding medium [7, 8] by a subsequent re-organization of the polymer chains within the brush [9]. The term *responsive brush* is reserved for systems in which strong and reversible changes in film thickness and polymer re-organization occur and for which this switching process can be repeated many times. Also a change of the conformation often results in modified interactions with the surrounding medium. An example is the pH controlled switching of the wetting behavior [10, 11]. Of special interest is also the interaction with bio-molecules with applications ranging from protein resistivity [12], to over selective binding [13], to the controlled release of drugs for carrier systems [14].

Most current applications of responsive polymer brushes utilize the external stimuli temperature, pH and ionic strength. Nothing is yet reported on the response of polymer brushes to elevated hydrostatic pressure. At first sight hydrostatic pressure does not appear to play a big part in everyday life, but there are numerous fields with huge impact. More than 70 % of the earth is covered by oceans with deep sea pressures of more than 1000 bar. Pressure affects proteins, lipids and membranes [15–18]. High pressure is used in food production for sterilization and conservation [19]. Polymer surface coatings are used to lubricate artificial joints, where for a knee replacement pressures up to 600 bar can occur [20, 21]. Additional information of pressure effects on biological structures and applications can be found in a recent review by Rivalain et al. [22].

Current knowledge of the effect of elevated hydrostatic pressure on polymer conformations

is mainly based on bulk systems [23–27]. Some information is available on microgels [28–30], but conformational pressure effects on solid supported inhomogeneous polymer brush coatings are completely unexplored. To examine these structures, a surface sensitive method is needed. Neutron and x-ray reflectometry can probe the laterally averaged density profile across the interface with Å-resolution. For the analysis of polymer brushes at a solid-liquid interface, neutron reflectometry (NR) is the method of choice. In principle x-rays are also capable of probing buried solid-liquid interfaces, but high intensities and high photon energies are needed to probe the interface through water [31]. These conditions can be realized at synchrotron radiation sources but beam damage is always a limiting factor. Neutrons will not lead to the problem of beam damage and, due to the transparency of Si crystals, are able to reach the solid-liquid interface through the substrates without severe loss of intensity. The recent success in building neutron reflectometry solid-liquid sample environments for hydrostatic pressures up to 2500 bar now allows scientists to probe the response of polymer brushes in the high pressure region [32–34].

This thesis starts with a short theoretical introduction to polymer brushes in Chapter 2 and the experimental details of sample preparation and characterization techniques in Chapter 3. The Langmuir-Schäfer transfer (Chapter 3.2.3) was utilized to prepare well-defined planar polyacrylic acid (PAA) and poly(N,N-dimethylaminoethyl methacrylate) (PDMAEMA) polymer brushes. These samples were characterized by x-ray and neutron reflectometry. The most important part of this work were neutron reflectometry measurements, using the Heidelberg high pressure cell [32], which made it possible to explore the response of planar polymer brushes to hydrostatic pressures up to 1000 bar.

In Chapter 4, first, pressure effects on pure polyelectrolyte PAA brushes are analyzed. As an additional subject, the second part of Chapter 4 elucidates whether an elevated hydrostatic pressure of 900 bar affects the adsorption of bovine serum albumin (BSA). It is known that hydrostatic pressure can change the structure of proteins and act to disfavor hydrophobic and electrostatic interactions that cause protein aggregation [35, 36], but no information is available on adsorption processes. The adsorption of BSA to PAA brushes was chosen as a standard model system for protein adsorption to polyelectrolyte brushes [14, 37–49]. PAA brushes provide a soft micro-environment for adsorbed proteins or enzymes preserving

structure and functionality of the immobilized species [37, 38, 50, 51]. If needed, a controlled release of immobilized bio-molecules is possible with the screening of electrostatic interactions at an increased ionic strength of the subphase [14, 41].

The results on PDMAEMA brushes are presented and discussed in Chapter 5. PDMAEMA exhibits a tunable (pH, molecular weight, conformation) lower critical solution temperature (LCST) in the range of $14-80\,^{\circ}\mathrm{C}$ in aqueous solution that comes along with a reversible swelling in water [4, 52, 53]. The polymer adopts a random coil structure below the LCST but forms a more collapsed globular structure above this temperature. Dehydration of the hydrophobic moieties is considered to be the major driving force for the observed coil-to-globule transition. For chemically different polymers, which also exhibit an LCST, pressure applications to isotropic bulk systems showed a significant swelling at elevated pressure, in particular close to the LCST, and below a threshold pressure of about 1000 bar [23–27, 29, 54]. In this regime, pressure P was found to act antagonistically to temperature T with a growth of the LCST with pressure in the $T(P)$ phase space [23–27, 54].

This work, using a PDMAEMA polymer brush, will elucidate how these observations transfer to the unknown pressure-response of an anisotropic polymer brush structure. To achieve this, NR measurements were performed at temperatures in the range of $20-60\,^{\circ}\mathrm{C}$ and hydrostatic pressures up to 1000 bar (Chapter 5.1). A new *local cavity* density functional theory (LC-DFT) (Chapter 2.3) was used for an analytical fit of the polymer brush density profile. It is argued that in the low pressure regime ($\lesssim 1000$ bar), hydrophobic interaction governs the polymer pressure response [23, 26, 54]. In fact, in 1959 Kauzmann surmised that in hydrophobic assemblies, *cavities* void of solvent have a large contribution to the partial molar volume that couples to external pressure [55]. Explicit-water computer simulations demonstrate that pressure swells polymers primarily by pushing solvent into solvent-inaccessible cavity regions [56–58], created by hydrophobic association. Based on this *cavity idea*, Kato introduced a volume-dependent free energy expression to successfully describe pressure effects on the LCST of hydrogels [26]. These ideas will now be used for spatially-varying, inhomogeneous polymer brushes. First it will be shown that the LC-DFT gives a thermodynamically consistent description of the brush structure with varying temperature, including the occurrence of a vertical phase separation above the LCST. It will be unequivocally

demonstrated that temperature and pressure effects on the detailed brush structure are perfectly antagonistic: structural changes of a temperature increase of 1 Kelvin is exactly canceled by a pressure increase of ~ 100 bar.

CHAPTER 2

Theory of polymer brushes

In 1953 Flory introduced a model to describe the conformational behavior of free polymers in a solvent by the free energy balance of two opposing effects.[59] The maximized configuration entropy gained from random walks of the polymer chains favors dense polymer structures, and is opposed by the osmotic pressure from polymer-solvent contacts in a good solvent. The average end-to-end distance R_F of this coil-like structure is given by

$$R_F \sim aN^{\frac{3}{5}} \tag{2.1}$$

with the Kuhn or monomer length a and degree of polymerization N.

Long chain polymers can be chemically or physically attached by one end to a surface or interface. This confinement results in a conformational behavior, quite different when compared to that of free polymers. An important factor is the interaction of the polymer with the interface (Figure 2.1). For strong attractive interactions, the polymer adopts a flat conformation. For weak or no interactions the polymer, fixed to the interface, is in the coil-like or mushroom state. A repulsive interactions repels the polymer from the interface and can lead to the formation of a depletion layer.
The concentration of polymers attached to an interface is defined by the grafting density

$$\sigma = \frac{\text{grafted polymers}}{\text{area}} \tag{2.2}$$

with an averaged grafted polymer-polymer distance

$$d_p \approx \frac{1}{\sqrt{\sigma}} \tag{2.3}$$

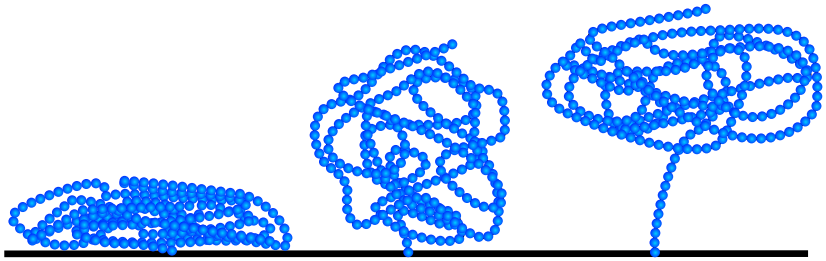

Figure 2.1: Conformation of grafted polymers for variate interaction with the interface - left: attractive interaction (pancake); middle: no or weak interaction (mushroom); right: repulsive interaction (depletion layer).

In the case of $d_p > R_F$, the grafted polymers are separated and do not interfere with each other (mushroom regime). With increasing grafting density the polymer surface packing is reaching a point where $d_p \leq R_F$. Further reduction of d_p results in polymer packing constraints and the polymer chains are obliged to stretch away from the interface (polymer brush) up to $H \gg R_F$ (Figure 2.2).

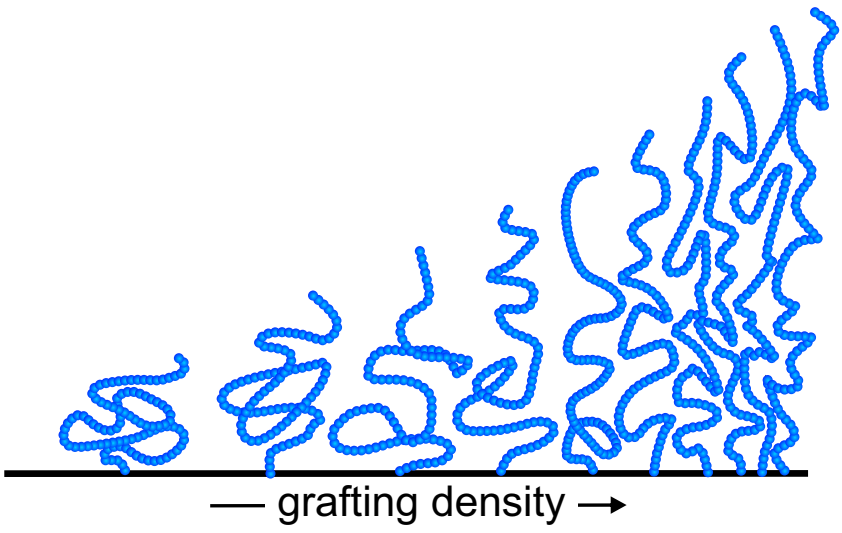

Figure 2.2: Conformation of surface anchored polymers with increasing grafting density.

2.1 Neutral brushes

Based on Flory's theory of free polymers in a solvent [59], Alexander and de Gennes presented the first theoretical model for neutral polymer brushes [60–62]. They calculated the reduction in configuration entropy from results for an ideal random walk of the polymer. To expand the work of Flory for free polymers, they postulated that the end-to-end distance of the grafted polymer covers a distance H from the grafting surface to the outer edge of the brush. This confinement resulted in a scaling prediction for the brush height H, which grows directly proportional to the degree of polymerization N. Thus the brush height $H \propto N$ grows much faster than the average Flory end-to-end distance $R_F \propto N^{\frac{3}{5}}$ of the free polymer. In this simple model no detailed information is given on the shape of the brush. All grafted polymers are stretched equally at a constant brush volume fraction density $\varphi(z)$, leading to a *block*-type density profile.

The Alexander- de Gennes model was further improved by Milner et al. [63, 64]. They took into account that the polymer chain free ends are not confined to the brush height H, but can be located at any distance from the interface. The result of their analytical self-consistent field (SCF) calculation is a *parabolic* shaped density profile $\varphi(z)$. The shape depends on the solvent quality for the brush polymers. In a good solvent, the brush is in a swollen state and will collapse when transferred to a bad solvent. The collapse is gradual for a continuous change of the solvent quality.

2.2 Charged brushes

Polyelectrolyte (PE) brushes consisting of charged polymers can exhibit physical properties fundamentally different from that of uncharged brushes [2]. The charge causes additional electrostatic interactions that dominate the brush structure and properties. Charged polymer segments can interact with the substrate and mutual repulsion strongly influences the interaction between the polymers. The strengths of these interactions is modified by external parameters of the surrounding medium. Counterions can screen electrostatic interactions, and if confined at high concentration inside the brush, add an additional osmotic pressure. This is especially important for strong (quenched) polyelectrolytes, where the number and position of charges on the chain is fixed. In the case of weak (annealed) polyelectrolytes brushes, the charges are not fixed and the average degree of dissociation depends on the pH value of the contacting aqueous phase.

In the last two decades, starting with Pincus [65], analytical and numerical SCF calculations have improved the theoretical understanding of PE brushes. The outcome of these simulations were complex phase diagrams with more diversified brush structures depending on chain length, ionic strength and grafting density of the respective systems. For example in the case of weak polyelectrolyte brushes, *Gaussian* shaped density profiles at low ionic strength and the *parabolic* form in the uncharged limit at high salt concentrations are theoretically predicted [66–68].

A more detailed overview of theoretical studies on the structure and properties of charged and neutral polymer brushes can be found in several review articles [1, 2, 9, 69, 70].

2.3 Stimuli responsive polymer brushes

Polymer brushes respond to their environment with a change of the polymer chain conformations [9]. A rearrangement of the polymer chains affects the density profile of the brush. In cooperation with Prof. Dr. Joachim Dzubiella (Humboldt Universität Berlin, Helmholtz-Zentrum Berlin), a new analytical LC-DFT model for the polymer density profile of stimuli responsive polymer brushes has been developed [71]. The analytical description of the brush density profile allows one to correlate the response of the structure of the polymer brush to changes of thermodynamically relevant parameters.

Within the standard Flory approach, all responses of polymers to temperature or pressure are condensed into the Flory interaction parameter $\chi(T,P)$ [59]. The latter describes the ratio of mean field polymer-polymer to polymer-solvent interactions. At θ-conditions ($\chi = 0.5$) all interactions cancel each other and the polymer adopts an ideal, non-interacting, conformation. When anchored at one end to an interface the ideal density distribution of a polymer brush is the starting point of the new theory. Instead of using the Flory interaction parameter χ, effective monomer-monomer interactions are included with a mean-field virial correction to the ideal brush density profile. The effect of elevated hydrostatic pressure is included with a separated correction, based on the theory of solvent-inaccessible cavities.

A polymer brush can be described by the monomer density profile $c_m(z)$ or the volume packing fraction

$$\varphi(z) = \frac{c_m(z)}{v_m} \tag{2.4}$$

where v_m is the monomer volume. The effective monomer diameter a is given by

$$a = \sqrt[3]{\frac{6v_m}{\pi}} \tag{2.5}$$

The polymer chains adopt a conformation $c_m(z)$, that minimizes the Gibbs free energy $G[c_m]$ of the brush:

$$G[c_m] = F_0[c_m] + F_{exc}[c_m] + PV[c_m] \tag{2.6}$$

F_0 is the entropic energy of the ideal brush, F_{exc} describes monomer interactions, P is the hydrostatic pressure, and V is the monomer and solvent accessible volume.
The term F_0 for the ideal brush is modeled by an ideal gas and a harmonic elastic term via

$$\beta F_0[c_m] = \int \mathrm{d}^3 r\, c_m(z) \left[\ln\left(\frac{c_m(z)}{c_{m0}} \right) - 1 \right] - \int \mathrm{d}^3 r\, c_m(z) \frac{(z)^2}{H_0^2} \tag{2.7}$$

with

$$\beta = \frac{1}{k_\mathrm{B} T} \tag{2.8}$$

After minimization $\delta F_0 / \delta c_m = 0$, eq. 2.7 leads to a purely Gaussian density profile

$$c_m(z) = c_{p0} e^{-\frac{(z)^2}{H_0^2}} \tag{2.9}$$

with the thickness H_0 of the ideal brush. The constant c_{p0} is determined by the normalization condition

$$\sigma = \frac{1}{N} \int c_m(z) \mathrm{d}z \tag{2.10}$$

Theoretical SCF calculations for non-interacting or very weakly interacting brushes have always led to a Gaussian decay of the density profile for intermediate to large distances $z \gtrsim H_0$ [69, 72, 73]. Directly at the grafting interface most theoretical simulations suffer from boundary effects that shift the maximum density away from the grafting point. Also important are the interactions with the grafting interface that cause considerable modifications of the profile for small z [73]. To describe the data of a complex experimental system, a heuristic approach is needed. Thus, all effects and interactions of the grafting interface are absorbed into the effective parameter H_0 of an assumed Gaussian profile.

A third order virial expansion of the monomer density $c_m(z)$ is used to model the effective monomer interactions:

$$F_{exc}[c_m] \simeq \int \mathrm{d}^3 r (B_2 c_m(z)^2 + \frac{1}{2} B_3 c_m(z)^3) \tag{2.11}$$

where B_2 and B_3 are the 2nd and 3rd virial coefficients. B_2 can be directly related to monomer interactions via

$$B_2 = -\frac{1}{2}\int \mathrm{d}^3 r \, (e^{-V(r)} - 1) \tag{2.12}$$

where $V(r)$ is the effective pair potential. Typically, the B_2 coefficient is on the order of the monomer size

$$|B_2| \sim v_m \tag{2.13}$$

and strongly dependent on the temperature T. For $B_2 = 0$ the brush is in a θ-solvent-like condition. In a good solvent ($B_2 > 0$), monomer interactions are less favored and the polymers try to avoid contacts. This is realized by a swelling of the brush. Under poor solvent conditions the monomer interaction is overall attractive with $B_2 < 0$ and the ideal brush collapses. A complete collapse of the brush is typically prevented by hard-core packing effects between the monomers. These effects are included in the 3rd virial coefficient which is on the order of

$$B_3 \simeq v_m^2 > 0 \tag{2.14}$$

The T-dependence of packing effects is typically small and thus B_3 is expected to be constant. Figure 2.3 shows simulated profiles in order to demonstrate how the virial expansions affects the brush under different solvent conditions.

Changing the pressure couples to the solvent accessible volume in the polymer brush system [26]. Recent computer simulations showed that pressure denatures proteins dominantly by pushing solvent into solvent-inaccessible cavity regions, presumably created by hydrophobic association [56–58]. This effect is transferred to the polymer brush system. In θ- to moderately poor solvent conditions, small clusters of aggregating chains are likely to be present. In those clusters, hydrophobic interactions create solvent-inaccessible cavities (SIC) that are influenced by hydrostatic pressure. For a SIC volume V_{SIC} the correction $PV[c_m] = P(V_{\mathrm{tot}} - V_{\mathrm{SIC}})[c_m]$ is applied to the inhomogeneous brush via

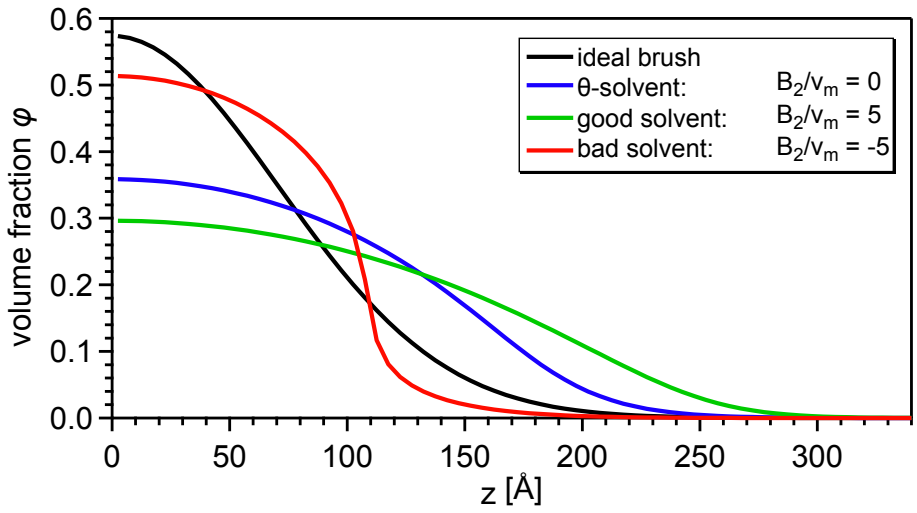

Figure 2.3: Simulated volume fraction profiles for $H_0 = 100\,\text{Å}$ and $\sigma = 0.2\,\text{nm}$. The ideal brush, without monomer interactions, is represented by a purely Gaussian profile (black). Including the hard-core packing effects via the third virial coefficient $B_3 = 10$ for hard spheres, the brush is swelling and adopts a volume fraction profile that is expected for θ-conditions (blue). The quality of the solvent influences the effective monomer interactions, represented by the second virial coefficient B_2. The brush is swollen in a good solvent ($B_2 > 0$; green) and collapsed in a bad solvent ($B_2 < 0$; red).

$$PV[c_m] \simeq PV_{\text{tot}} - Pv_0 \int \mathrm{d}z \, \frac{\partial p_{\text{SIC}}(c_m)}{\partial z} \tag{2.15}$$

where $p_{\text{SIC}}(c_m)$ is the probability to find two polymer segments at contact forming a SIC volume v_0. Close to θ-conditions the more unlikely clusters of more than two segments are to be neglected. The cavity volume v_0 should then be on the order of

$$v_0 \simeq v_m > 0 \tag{2.16}$$

as it reflects the cavity volume between a few segment monomers. For a pair of n particles in a volume v the probability p_{SIC} to meet in a contact volume $a^3 \simeq v_m$ is

$$p_{\text{SIC}} \simeq g(a) n^2 \frac{v_m}{v} \tag{2.17}$$

leading to

$$dp_{\mathrm{SIC}} \simeq g(a) c_m^2 v_m \mathrm{d}v \tag{2.18}$$

given a local (homogeneous) density $c_m = n/v$. At moderately poor to θ-conditions the contact value of the pair correlation function $g(a)$ is approximated by

$$g(a) \simeq 1 \tag{2.19}$$

Gathering all terms of the Gibbs free energy (equation 2.6), the minimization $\delta G/\delta c_m(z)$ yields the determining equation

$$c_m(z) = c_{p0} e^{-z^2/H_0^2} e^{-2B_2 c_m(z) - \frac{3}{2} B_3 c_m(z)^2 - 2\beta P v_0 c_m(z) v_m} \tag{2.20}$$

which has to be self-consistently solved under the normalization condition defined by the grafting density (equation 2.10).

The parameters H_0, $B_2(T)$, B_3 and v_0 are fitting parameters to describe the experimental polymer brush density profile. A temperature dependence should only be reliant on B_2. Both, the pressure P and the B_2 term are linear in $c_m(z)$. Thus effectively the pressure term just corrects the effective interaction between monomers. The fact that P and v_0 are always > 0 will effectively always lead to more repulsion between monomers at elevated hydrostatic pressure.

For small exponents ($z \lesssim H_0$), equation 2.20 can be expanded to

$$c_m(z) \simeq c_{p0} \left(1 - \frac{z^2}{H_0^2} (1 + 2(B_2 + \beta P v_0 v_m) c_m + \frac{3}{2} B_3 c_{p0}^2) \right) \tag{2.21}$$

thus having always a parabolic character for small z and a Gaussian decay for large z. SCF-motivated but empirical profiles of the sum of a parabolic profile plus a Gaussian tail have historically led to satisfactory fits of neutron scattering data in good solvents [74, 75]. The advantage of the current approach is that temperature and pressure effects are separately considered and physically relevant parameters are directly used in the fitting process.

CHAPTER 3

Experimental

3.1 Materials

Substrates

The substrates for the reflectivity experiments were polished silicon wafers with surface rms roughness < 6 Å. For neutron reflectometry disc-shaped silicon substrates (60 mm in diameter and 10 mm in height) were supplied by Siliciumbearbeitung Holm (Tann/Ndb., Germany). Preliminary X-ray reflectivity measurements were performed on smaller wafers (20 mm x 20 mm). The latter were cut from bigger wafers (150 mm in diameter and 0.625 mm in height, <100> orientation), bought from CrysTec GmbH (Berlin, Germany).
Before use, all substrates were cleaned for 30 minutes in ethanol and subsequently rinsed with ultra-pure water. During the rinsing process there was no adherence of water, thus pointing to a hydrophobic surface. Before second use, all substrates were cleaned and re-polished (Siliciumbearbeitung Holm; Tann/Ndb., Germany).

Polymers

Perdeuterated polystyrene (dPS) was purchased from Polymer Standard Service (Mainz, Germany - M_W 65400; PDI 1.02) and from Polymer Source (Montreal, Canada - M_W 60000; PDI 1.10). Diblock copolymer polystyrene$_{41}$ - b - poly acrylic acid$_{271}$ (PS-PAA; M_W 23800; PDI 1.09) and perdeuterated polystyrene$_{49}$ - b - poly acrylic acid$_{222}$ (dPS-PAA; M_W 21500; PDI 1.13) were bought from Polymer Source (Montreal, Canada). Diblock copolymer perdeuterated polystyrene$_{32}$ - b - poly 2-(dimethylamino) ethyl methacrylate$_{113}$ (dPS-PDMAEMA; M_W 21000; PDI 1.17) was synthesized and provided by André Gröschel and Axel Müller, University of Bayreuth [76]. All polymers were used as received.

Proteins

Bovine serum albumin (BSA; catalog number A-6003) was bought from Sigma-Aldrich and used without further purification.

Solvents

Ultra pure Water (H_2O) was obtained by using a Milli-Q purification system (Merck Millipore; resistance > 18.2 MOhm·cm). D_2O (>99 %), and all other organic solvents (absolute puriss. p.a.) were from Sigma-Aldrich. Before use, D_2O was degassed in an evacuated desiccator to minimize the probability of bubble formation at the solid-liquid interface for increased temperature or upon reduction of elevated hydrostatic pressure back to ambient conditions.

3.2 Sample preparation techniques

3.2.1 Diblock-copolymer Langmuir layers

The polymer brushes were prepared using the Langmuir-Schäfer transfer of free floating precursor Langmuir layers from amphiphilic diblock copolymers to silicon substrates, pre-spincoated with perdeuterated polystyrene (dPS). The advantage of this *grafting to* approach is that the polydispersity of the brush depends on the polydispersity (PDI) of the diblock copolymer (PDI 1.13 for dPS-PAA and PDI 1.17 for dPS-PDMAEMA). The polymer brush grafting density is adjusted by varying the surface density of the precursor Langmuir layer.

3.2.2 Spin coating

Spin coating is a technique to prepare thin and uniform films on flat solid substrates [77]. For the case of thin polymer films the polymer is dissolved in a volatile solvent. An excess amount of the solution is deposited on the substrate which is then rotated at high speed to spread the solvent by centrifugal force. Only a small layer of the solution remains and the solvent subsequently evaporates to leave a uniform thin polymer layer. The thickness of the layer depends on the polymer concentration and the rotational speed.

To prepare a dPS layer with a thickness of 15-30 nm, 6 mg/ml dPS were dissolved in toluene and spincoated (spincoater Model 6708D, SCS, US) at a speed of 3000-4000 revolutions per minute for 60 s. The rotational symmetry of the circular wafers guaranteed a homogenous coating. After the spincoating process, the dPS layer was annealed for 20 min at 130 °C above the glass transition of polystyrene ($\approx$ 100 °C) in an desiccator filled with argon. The resulting layers were optical homogenous and X-ray measurements in the center and at the boundary showed a layer thickness variation of only $\approx$ 2.5 % (Figure 3.1).

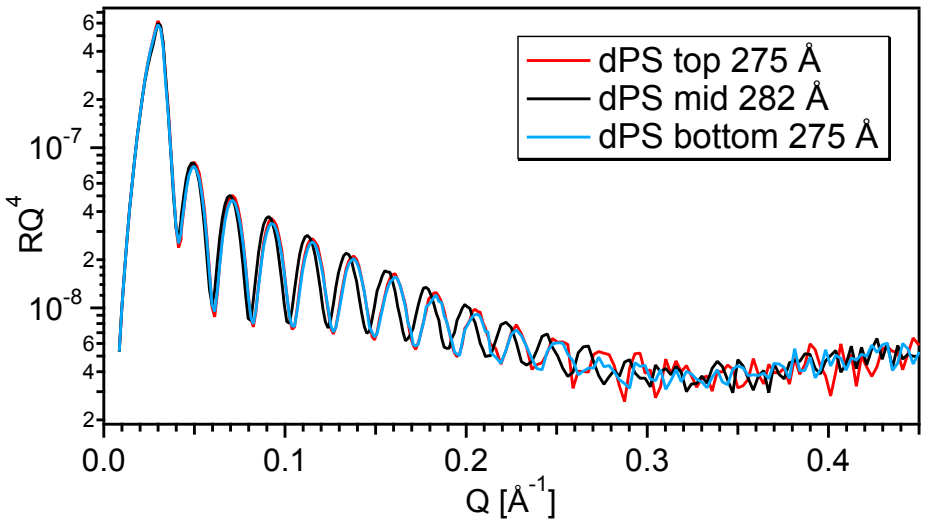

Figure 3.1: X-ray reflectivity data to evaluate the homogeneity of a spincoated dPS layer, prepared on disc-shaped substrate with a diameter of 60 mm. The data were measured in the center of the sample and 20 mm above and below the center with a beam width of 8 mm.

3.2.3 Langmuir-Schäfer transfer

The Langmuir-Schäfer transfer is variant of the familiar Langmuir-Blodget transfer [78]. A free floating Langmuir monolayer on a water surface is transferred to a flat sample by horizontally dipping the substrate on the water surface (Fig. 3.2). If the layer sticks to the substrate it can be removed with the sample. Perfect transfer is achieved if the polymer surface loss area on the water divided by the surface area of the sample equals unity. The polymer surface loss area at the transfer is accompanied by a drop in the surface pressure and is determined upon reducing the available area for the remaining polymers of the floating Langmuir layer until the value of the surface pressure before the transfer is regained.
A specific example is given in Figure 4.1 (Chapter 4.2) for the preparation of PAA brushes.

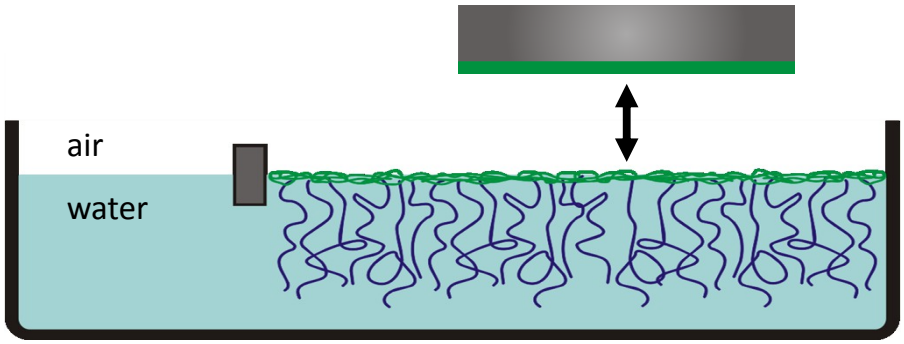

Figure 3.2: Schematic Langmuir-Schäfer transfer of an amphiphilic block copolymer, prepared as a free floating precursor Langmuir layer with defined surface density at the air-water interface of a Langmuir trough.

3.3 Sample characterization - Reflectivity

Neutron and X-ray reflectometry are analytical scattering techniques to probe laterally averaged density profiles across an interface. The following section includes brief introductions to the theory of reflectometry, analytical techniques and principle designs of reflectometry instruments [79, 80].

3.3.1 Single interface

A scattering process is defined by the momentum transfer $\vec{Q} = \vec{k}_r - \vec{k}_i$. In the case of specular reflectivity from stratified media, the angle of reflection with respect to the scattering plane θ_r equals the angle of the incoming beam with respect to the interface, θ_i:

$$\theta = \theta_i = \theta_r \tag{3.1}$$

For elastic scattering, $|k| = |k_i| = |k_r| = 2\pi/\lambda$, this results in a momentum transfer normal to the scattering plane:

$$Q = Q_z = \frac{4\pi}{\lambda} \sin\theta \tag{3.2}$$

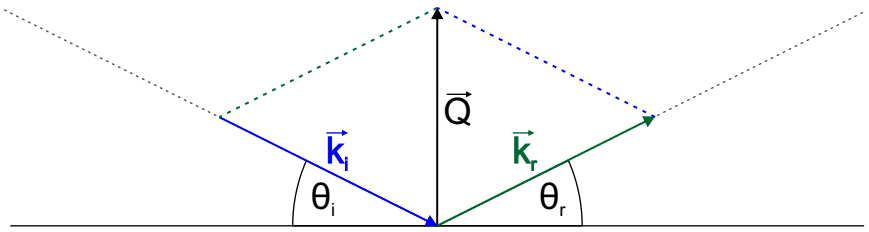

Figure 3.3: Scattering process at an interface. The scattering vector $\vec{Q}$ is defined as the difference between the scattered and the incoming wave-vector $\vec{Q} = \vec{k}_r - \vec{k}_i$. For an elastic, specular process $\theta_i = \theta_r$, the scattering vector $\vec{Q} = Q_z$ is normal to the *xy*-scattering interface.

X-ray and neutron reflectivity are defined as the reflected intensity $I_r(Q)$, normalized on the intensity of the incoming beam I_0. The resulting reflectivity

$$R(Q) = \frac{I_r(Q)}{I_0} \tag{3.3}$$

depends on the scattering length density, SLD, of the scattering media. The SLD is encoded in the refractive index n

$$n = 1 - \delta - i\gamma = 1 - \frac{\lambda^2}{2\pi}\mathrm{SLD} - \mathrm{i}\frac{\lambda}{4\pi}\mu \tag{3.4}$$

where μ is the linear adsorption coefficient, which can be neglected in this work. The SLD is different for neutrons and X-rays because neutrons interact with the nuclei and X-rays interact with the electron density ρ_e of the sample.

The neutron SLD is defined by the sum over M atoms with the coherent scattering length b_i of atom i in a volume V:

$$\mathrm{SLD_{neutron}} = \frac{1}{\mathrm{V}}\sum_{\mathrm{i=1}}^{\mathrm{M}} \mathrm{b_i} \tag{3.5}$$

Due to the interaction with the nucleus, the SLD changes for different isotopes of the same element [81]. The most prominent example is the hydrogen ($b_\mathrm{H} = -3.406\,\mathrm{fm}$) to deuterium ($b_\mathrm{D} = 6.671\,\mathrm{fm}$) contrast. It can be used to label and visualize hydrogen containing parts of a sample by deuterium isotope exchange.

Exemplary neutron SLD's are [81]:

$$\begin{aligned}
\mathrm{SLD_{air}} &= 0 \\
\mathrm{SLD_{Si}} &= 2.07 \cdot 10^{-6}\,\text{Å}^{-2} \\
\mathrm{SLD_{D_2O}} &= 6.36 \cdot 10^{-6}\,\text{Å}^{-2} \\
\mathrm{SLD_{H_2O}} &= -0.56 \cdot 10^{-6}\,\text{Å}^{-2}
\end{aligned}$$

Isotope exchange does not affect X-ray scattering. The X-ray SLD is defined as:

$$\mathrm{SLD_{X\text{-}ray}} = \mathrm{r_e}\rho_\mathrm{e} \tag{3.6}$$

where $r_e = 2.81$ fm is the classical radius of the electron.

So far, only the reflected wave $\vec{k_r}$ with reflectivity $R(Q)$ was discussed. Parts of the incoming plane wave k_i can also be transmitted into the second medium. Due to conservation of energy the intensity T of the transmitted wave is $T = 1 - R$. The angle of the transmitted wave with respect to the scattering plane, θ', is described by Snell's law:

$$n \cos\theta = n' \cos\theta' \tag{3.7}$$

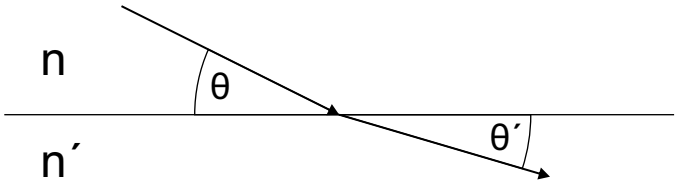

Typically, $1 - n = \delta \simeq \mathcal{O}(10^{-5})$ and $\theta \simeq \mathcal{O}(1^\circ)$, leading to the following approximations:

$$1 - n^2 \approx 2\delta \tag{3.8}$$

$$\frac{n - n'}{n} \approx n - n' \tag{3.9}$$

$$n \cdot (n - n') \approx n - n' \tag{3.10}$$

$$\sin\theta \approx \theta \tag{3.11}$$

$$\cos\theta \approx 1 - \frac{\theta^2}{2} \tag{3.12}$$

For the scattering at an interface to an optical thinner medium $n' < n$ a critical angle θ_c is found where $\theta' = 0$:

$$\cos\theta_c = \frac{n'}{n} \tag{3.13}$$

$$\Rightarrow \theta_c^2 = 2(n - n') = 2(\delta' - \delta) \tag{3.14}$$

$$\Rightarrow Q_c^2 = 16\pi(\mathrm{SLD}' - \mathrm{SLD}) \tag{3.15}$$

In the region $\theta < \theta_c$ all incoming intensity is reflected and $R(Q < Q_c) = 1$. For $\theta > \theta_c$ the reflectivity $R = rr^\star$ is given by Fresnel's law:

$$r = \frac{n\sin\theta - n'\sin\theta'}{n\sin\theta + n'\sin\theta'} \tag{3.16}$$

The usual experimental parameter is the angle of incidence, θ. Using Snell's law, equation 3.16 can be written as:

$$r = \frac{n\sin\theta - \sqrt{n'^2 - n^2 + n^2\sin^2\theta}}{n\sin\theta + \sqrt{n'^2 - n^2 + n^2\sin^2\theta}}$$

$$(3.4) \Rightarrow r = \frac{n\sin\theta - \sqrt{2(\delta - \delta') + n^2\sin^2\theta}}{n\sin\theta + \sqrt{2(\delta - \delta') + n^2\sin^2\theta}}$$

$$(3.14) \Rightarrow r(\theta) \approx \frac{\theta - \sqrt{\theta^2 - \theta_c^2}}{\theta + \sqrt{\theta^2 - \theta_c^2}} \tag{3.17}$$

$$(3.2) \Rightarrow r(Q) \approx \frac{Q - \sqrt{Q^2 - Q_c^2}}{Q + \sqrt{Q^2 - Q_c^2}} \tag{3.18}$$

For $Q \gg Q_c$ (after expansion of 3.18 with $Q + \sqrt{Q^2 - Q_c^2}$) the Fresnel-reflectivity from a simple single interface is described by the power law

$$R_F(Q) \approx \frac{Q_c^4}{16Q^4} \tag{3.19}$$

$$(3.15) \Rightarrow R_F(Q) \approx \frac{16\pi^2\Delta\mathrm{SLD}^2}{Q^4} \tag{3.20}$$

To illustrate the impact of SLD differences, ΔSLD, Figure 3.4 shows simulated neutron reflectivity data for four interfaces (air-Si, Si-air, air-H_2O, air-D_2O). A region of total reflection $R = 1$ is only visible for $\Delta\mathrm{SLD} = \mathrm{SLD}' - \mathrm{SLD} > 0$. This is given for the scattering at the interfaces air-Si ($\Delta\mathrm{SLD}_{\text{air-Si}} = 2.07$) and air-$D_2O$ ($\Delta\mathrm{SLD}_{\text{air-D}_2\text{O}} = 6.36$). As expected from equation 3.15, the critical edge Q_c shifts to higher Q with an increase of ΔSLD. At high Q the reflectivity of all interfaces follows the Q^{-4} power law decay (equation 3.20). The relative height of $R(Q)$ depends on the absolute difference $|\Delta\mathrm{SLD}|$. There is no difference in the high Q reflectivity for the scattering from an air-Si interface compared to a Si-air interface. An important implication of equation 3.20 is that the reflectivity is not sensitive to absolute

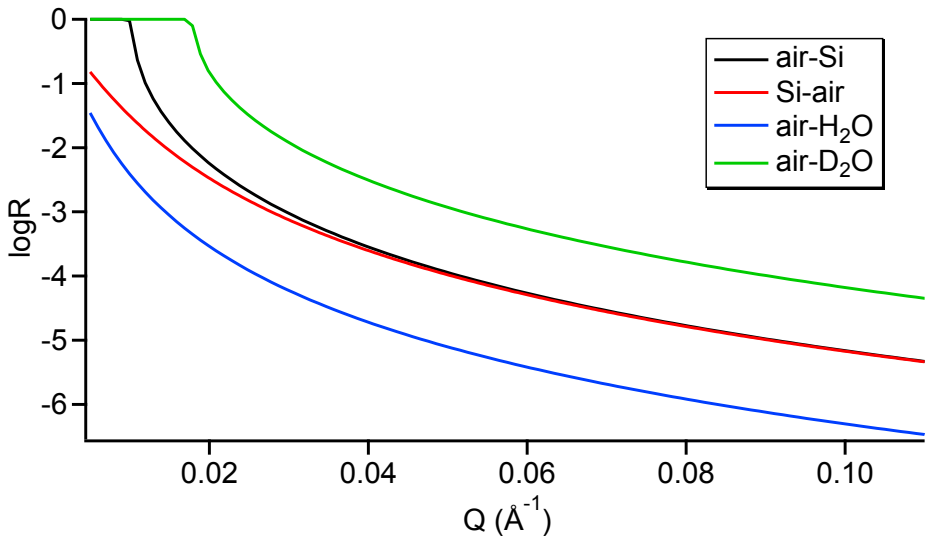

Figure 3.4: Simulated neutron reflectivity for several common interfaces.

values of the SLD but only on differences ΔSLD. To quantitatively evaluate reflectivity data, at least one reference SLD has to be well defined.

3.3.2 Single layer

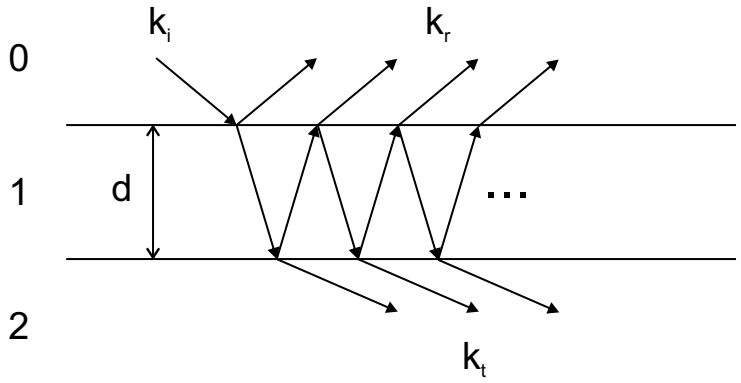

Figure 3.5: Schematic scattering process for a single layer. Inside the layer multiple reflections need to be taken into account to calculate the reflectivity.

A planar substrate coated with a single layer (Figure 3.5) consists of two interfaces (0-1;1-2) where neutrons or X-rays can be reflected and transmitted. The superposition of both reflected waves is constructive or destructive and is the reason for Kiesig oscillations in the reflectivity (Figure 3.6). In the kinematic limit $\theta > 3\theta_c$, the length of one oscillation ΔQ in

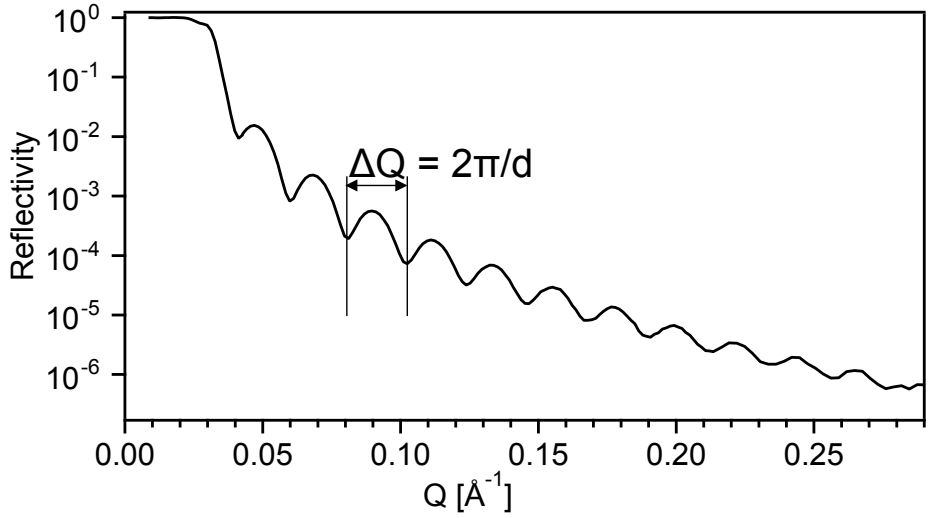

Figure 3.6: Reflectivity of a single dPS layer on a Si substrate.

reciprocal space is indirectly proportional to the thickness d of the coated layer in real space [79].

Using Bragg's law

$$2d\sin\theta = n\lambda \tag{3.21}$$

and equation 3.2, the thickness d of the layer is derived by

$$d = \frac{2\pi}{\Delta Q} \tag{3.22}$$

For the calculation of the reflectivity from a single layer multiple reflections have to be taken into account (Figure 3.5). After the reflection r_{12} from the second interface, the incident wave is transmitted t_{10} and reflected r_{10} from the first interface. Each time the wave passes the layer, a phase factor $p = exp(ik_1 d)$ is needed. All contributions to the reflectivity add up to:

$$
\begin{aligned}
r &= r_{01} + t_{01} r_{12} t_{10} p^2 + t_{01} r_{12}^2 r_{10} t_{10} p^4 + t_{01} r_{12}^3 r_{10}^2 t_{10} p^6 + ... \\
&= r_{01} + t_{01} r_{12} t_{10} p^2 \sum_{m=0}^{\infty} (r_{10} r_{12} p^2)^m \\
&= r_{01} + t_{01} r_{12} t_{10} p^2 \frac{1}{1 - r_{10} r_{12} p^2} \\
&= \frac{r_{01} + r_{12} p^2}{1 + r_{10} r_{12} p^2}
\end{aligned} \tag{3.23}
$$

In the last part of the derivation, the relations $r_{10} = -r_{01}$ and $t_{10} t_{01} - r_{10} r_{01} = 1$ were used. Finally the reflectivity R calculates to:

$$
R = r r^{\star} = \frac{r_{01}^2 + r_{12}^2 + 2 r_{01} r_{12} \cos(2 k_1 d)}{1 + r_{10} r_{12}^2 + 2 r_{10} r_{12} \cos(2 k_1 d)} \tag{3.24}
$$

and can be approximated for $Q \gg Q_c$ to

$$
\begin{aligned}
R(Q) \approx \frac{16\pi^2}{Q^4} [&(\mathrm{SLD}_1 - \mathrm{SLD}_0)^2 + (\mathrm{SLD}_2 - \mathrm{SLD}_1)^2 \\
&+ 2 (\mathrm{SLD}_1 - \mathrm{SLD}_0) (\mathrm{SLD}_2 - \mathrm{SLD}_1) \cos(Qd)]
\end{aligned} \tag{3.25}
$$

Note, that $R(Q)$ is invariant to a commutation of $(\mathrm{SLD}_1 - \mathrm{SLD}_0)$ with $(\mathrm{SLD}_2 - \mathrm{SLD}_1)$. To identify a unique profile, either SLD variations or additional constraints (density, thickness, ...) are needed.

3.3.2.1 Interface roughness

A real surface or interface most likely exhibit a certain roughness Σ. According to Névot and Croce [82], a graded interface $n(z) \propto \mathrm{erf}(z)$ can be described by the modified Fresnel-coefficients

$$
r_{\mathrm{rough}} = r \exp(-2 k k' \Sigma^2) \tag{3.26}
$$

To ensure correct calculation of the reflectivity, the roughness should not exceed $1/3$ of the thickness of adjacent layers.

3.3.3 Multiple layers

Most real samples consist of more than one layer or exhibit a continuously changing SLD profile that is divided and approximated by a stack of multiple layers (Figure 3.7).

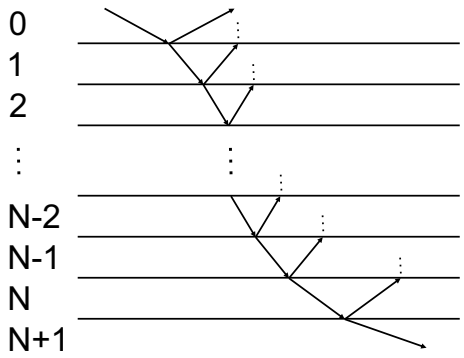

Figure 3.7: Schematic scattering process for a multi layer. Similar to the calculation of the reflectivity for a single layer, inside each layer multiple reflections need to be taken into account.

3.3.3.1 Parratts recursive formalism

The Parratt-formalism [83] is a recursive algorithm to calculate the reflectivity from a sample consisting of N layers with finite thickness between an infinite fronting and backing (Figure 3.7). Equation 3.23 can be generalized to the reflectivity of layer (N) and layer $N-1$:

$$r'_{N-1,N} = \frac{r_{N-1,N} + r_{N,N+1}\exp(2ik_N d_N)}{1 + r_{N-1,N} r_{N,N+1}\exp(2ik_N d_N)} \tag{3.27}$$

$$(3.16) \Rightarrow r_{N,N+1} = \frac{k_{N+1} - k_N}{k_{N+1} + k_N} \tag{3.28}$$

$r'_{N-1,N}$ includes the internal reflections at the interfaces between layer $(N-1)$ and layer N and between layer N and layer $(N+1)$. Further reflectivities are given by the recursion:

$$r'_{N-2,N-1} = \frac{r_{N,N-1} + r'_{N-1,N}\exp(2ik_{N-1} d_{N-1})}{1 + r_{N-2,N-1} r_{N-1,N}\exp(2ik_{N-1} d_{N-1})} \tag{3.29}$$

This formalism can be resumed until $r_{0,1}$. The recursion arises from the fact that due to infinite thickness of the backing, none of the transmitted intensity is reflected back to the sample layers.

Roughness between the layers is included using the modification to the reflectivity as described in equation 3.26.

3.3.3.2 Abeles transfer matrix method

Parratts recursive algorithm delivers an exact calculation of the reflectivity for a layered structure including multiple reflections. A mathematical equivalent, but computationally faster approach is given by the optical transfer matrix formalism, developed by Abeles [84]. Based on the linearity of the equation for the propagation of light, a plane wave traveling through a structure of N homogenous layers of finite thickness d_n can be described by the product of optical transfer matrices

$$\begin{pmatrix} E_0^+ \\ E_0^- \end{pmatrix} = M \cdot \begin{pmatrix} E_{N+1}^+ \\ 0 \end{pmatrix} \tag{3.30}$$

$$M = \prod_n c_n \tag{3.31}$$

where c_n is the characteristic transfer matrix for layer n, including the reflection and transmission at the interface between the layers n, $n+1$ and the propagation through layer n.

$$c_n = \begin{pmatrix} exp(ik_n d_n) & r_{n,n+1} exp(ik_n d_n) \\ r_{n,n+1} exp(-ik_n d_n) & exp(-ik_n d_n) \end{pmatrix} \tag{3.32}$$

The reflectivity of the whole system is finally calculated as:

$$R = \left| \frac{M_{12}}{M_{22}} \right|^2 \tag{3.33}$$

3.3.4 Reflectivity instruments

The reflectivity R is a function of the scattering vector Q. Under specular conditions:

$$Q = Q_z = \frac{4\pi}{\lambda} \sin\theta$$

For most reflectivity instruments a variation of the scattering vector is realized either via a beam of constant wavelength λ while scanning the angle of incidence θ (monochromatic) or vice versa (time-of-flight). In the following, a short introduction to both types of instruments is given.

For detailed information on the instrument that were used in this work please refer to section A.3 of the appendix.

3.3.4.1 Monochromatic

A monochromatic instrument uses a well defined constant wavelength λ and the reflectivity is measured as a function of the incident angle θ. This setup is realized for most X-ray reflectometers and some neutron reflectometers at reactor based neutron sources with a continuous neutron flux. Wavelength and resolution are set by a monochromator and thus in most cases are not tunable. An example for a monochromatic neutron reflectometer is the instrument V6 at the Helmholtz-Zentrum Berlin [85].

3.3.4.2 Time-of-flight

At time-of-flight (TOF) reflectometers the incident angle θ is held constant and the reflectivity is measured as a function of the wavelength λ. For the evaluation of the wavelength, the speed of the neutrons is used. According to the de Broglie relation

$$\lambda = \frac{h}{p} = \frac{h}{m_n v} \Rightarrow v = \frac{h}{m_n \lambda} \tag{3.34}$$

cold neutrons with a wavelength of 5 Å move with a speed of ≈ 800 m/s. The time a cold neutron needs to cover a distance of several meters is in the order of milliseconds. This

time-of-flight over a defined distance is a precisely measurable parameter to determine the neutron wavelength. In a TOF reflectometer like Bioref at the Helmholtz-Zentrum Berlin [86] a chopper system creates a pulsed white beam of neutrons with a well characterized wavelength spectrum. Knowing the starting point and starting time, the wavelengths λ of the reflected neutrons are encoded in their time-of-flight to the detector.
The advantage of a TOF reflectometer over to a monochromatic one is the simultaneous measurement of a broad Q-region instead of only one point in Q at a time. The wavelength resolution is set by the shape of the neutron pulse and can be modified with the chopper system (speed, position) to the requirements of the experiments. By relaxing the resolution, the neutron flux is increased and the time for a measurement can be reduced.

3.3.5 Data analysis

3.3.5.1 Box-model

In general, neutron reflectivity data can be well described and analyzed using an arbitrary box or layer model for the SLD profile $\mathrm{SLD(z)}$ with i boxes or layers of thickness d_i. Including roughness Σ_i between adjacent layers, each box i has up to three (neglecting adsorption) independent fitting parameters (d_i, $\mathrm{SLD_i}$, Σ_i). All interesting physical parameters of the measured system have to be extracted from the fitted SLD profile $\mathrm{SLD(z)}$.
The box-model was used for the X-ray sample characterization and the analysis of the neutron reflectivity for the PAA brush system.

3.3.5.2 Analytical model

It is always possible to fit reflectivity data with an arbitrary box-model that in most cases results in a good but not necessarily a unique SLD profile. If known, input from physical constraints can be used to restrict unlike fits and improve the reliability of the result. The best way to include these constraints is an analytical description of the measured system using parameters that are directly correlated to relevant physical properties (mass, shape, thickness, ...). If such a model exists, the SLD profile is described by an analytical function of physical parameters that are used as variables during the fitting process instead of

arbitrary box parameters. Thus, a good analytical description can also drastically reduce the number of fitting parameters.

For the explicit calculation of the reflectivity with Abeles transfer matrix formalism, the profile still has to be transferred into a box-like model. In this case however, the box parameters are not arbitrary, but a function of the analytical description.
In cooperation with Prof. Dr. Joachim Dzubiella, from the Soft Matter Theory group at the Helmholtz-Zentrum Berlin, a thermodynamically consistent density functional theory was used to describe the density profiles of stimuli responsive polymer brushes. The details of this theoretical model are given in Chapter 2.3.
The analytical description has been used to fit the neutron reflectivity data of the PDMAEMA brushes (Chapter 5.3). It was possible to directly transfer the fitted model parameters to structural and thermodynamic relevant properties of the brush.

3.3.6 The NR SLD model for solvent swollen polymer brushes

The reflectivity of a sample is defined by its SLD profile. A characteristic neutron reflectometry SLD profile for the samples in this work is shown in Figure 3.8.
The SLD profile can be divided in four parts. The first part $z < 0$ depicts the Si substrate, the last part the D_2O subphase. Both parts are modeled with infinite thickness on atomic length scales. Sandwiched between substrate and subphase are the dPS sublayer and the polymer brush. The dPS sublayer is modeled by a box of thickness $d_{\mathrm{dPS}} = z_0$, $\mathrm{SLD}_{\mathrm{dPS}}$ and roughness of the Si substrate Σ_{Si}. The the polymer brush region is characterized by an inhomogeneous SLD profile composed of a SLD mixture of the polymer brush $\mathrm{SLD}_{\mathrm{brush}}$ with the D_2O subphase $\mathrm{SLD}_{\mathrm{D_2O}}$. The values of all basic SLD's of this work are gathered in Table 3.1.
To calculate the reflectivity of the polymer brush, this part of the SLD profile is divided in n layers of equidistant thickness d_{brush}. The $\mathrm{SLD}_{\mathrm{brush}}(\mathrm{z})$ in each layer is connected to the volume fraction $\varphi(z)$ of the respective polymer brush in the D_2O subphase via

$$\mathrm{SLD}_{\mathrm{brush}}(\mathrm{z}) = \varphi(\mathrm{z}) \cdot \mathrm{SLD}_{\mathrm{polymer}} + (1 - \varphi(\mathrm{z})) \cdot \mathrm{SLD}_{\mathrm{D_2O}} \tag{3.35}$$

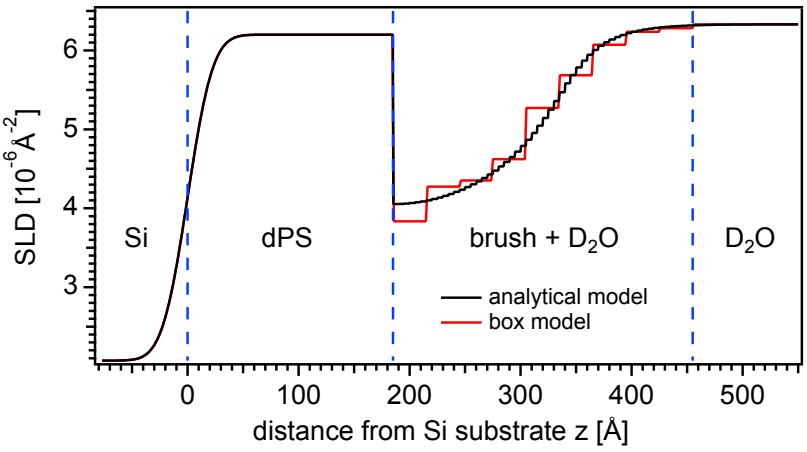

Figure 3.8: Exemplary scattering length density profiles SLD(z) used for fitting the NR data of a PDMAEMA brush (sample S1) at 20 °C. The sharp interface at $z_0 = 185$ Å is defined by the chemical bonds between the dPS and PDMEAMA blocks and is the starting point $\tilde{z} = z - z_0$ for plots of the analytical polymer brush volume fraction profile $\varphi(\tilde{z})$.

The thickness of the dPS sublayer z_0 depends on the sample preparation. For a sample independent comparison of the polymer volume fraction profiles $\varphi(z)$, all respective plots are shifted by z_0 to achieve a consistent start, $z - z_0 = \tilde{z} = 0$, of the polymer brush volume fraction profile

$$\varphi(\tilde{z}) = \varphi(z - z_0) \tag{3.36}$$

Table 3.1: Summary of all basic scattering length densities used in this work [81, 87].

Substance	SLD [10^{-6} Å^{-2}]
Si	2.07
D_2O (20 °C, 1 bar)	6.36
dPS (1 bar)	6.4
PAA	2.34
PDMAEMA	0.8

3.4 Neutron reflectometry sample environment

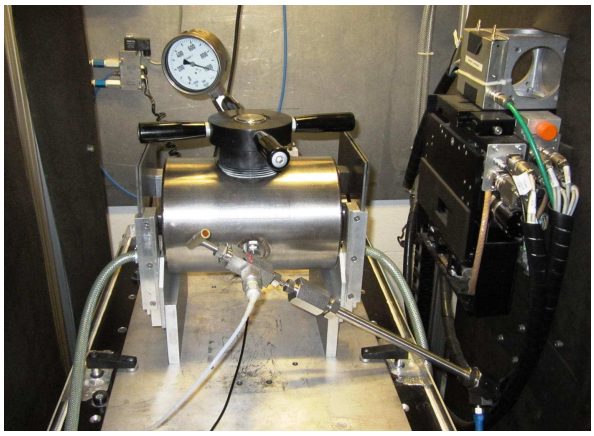

(a) NR high pressure cell @1000 bar

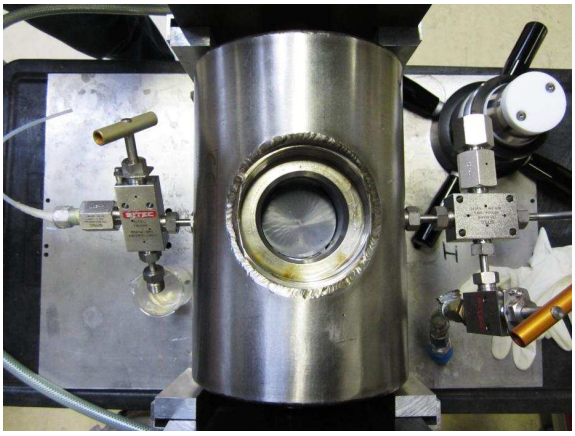

(b) Top view of open NR high pressure cell

Figure 3.9: Heidelberg high pressure cell for neutron reflectometry mounted to the sample stage at FIGARO (ILL).

For the NR measurements two sample cells were used. Experiments at elevated hydrostatic pressure were facilitated with the Heidelberg high pressure cell for neutron reflectometry (Figure 3.9). It was the first available cell for neutron reflectometry where a hydrostatic pressure up to 1000 bar could be applied. A detailed description of this cell is published by Kreuzer et al. [32]. Briefly, the main body consists of stainless steel and hosts disk-shaped silicon substrates with a diameter of 60 mm and height of 10 mm. The neutron optical windows are made from sapphire to withstand the pressure and provide high transparency for neutrons [88]. The solvent volume in the cell is 55 ml. The pressure is generated using a manual syringe pump and H_2O as hydraulic fluid. A separation piston cell, mounted between the pressure generation system and the high-pressure cell, reliably separates the sample fluid from the hydraulic fluid. An independent closed water circuit through the outer shell of the cylindrical main body of the cell, connected to an external water bath, enables temperature control in a range from 5 to 60 °C. When changing the temperature of the external water bath, an equilibration time of 30 min is needed to reach the desired target temperature, which is measured by a PT100 thermocouple within a tolerance of 0.2 K.

For temperature dependent measurements exclusively at ambient pressure a simple solid-liquid sample flow cell has been used (Figure 3.10). Here, the wafer is sandwiched between two thermostatic aluminum plates and a Teflon trough for the liquid subphase. The design was adapted for disk-shaped substrates from an earlier version of the flow cell [89]. The sample temperature is also controlled by a water-thermostat and measured by a PT100 thermocouple placed in the Teflon container underneath the liquid subphase. Changes to the temperature of the temperature stabilizing water bath (JULABO) required an equilibration time of 10 min.

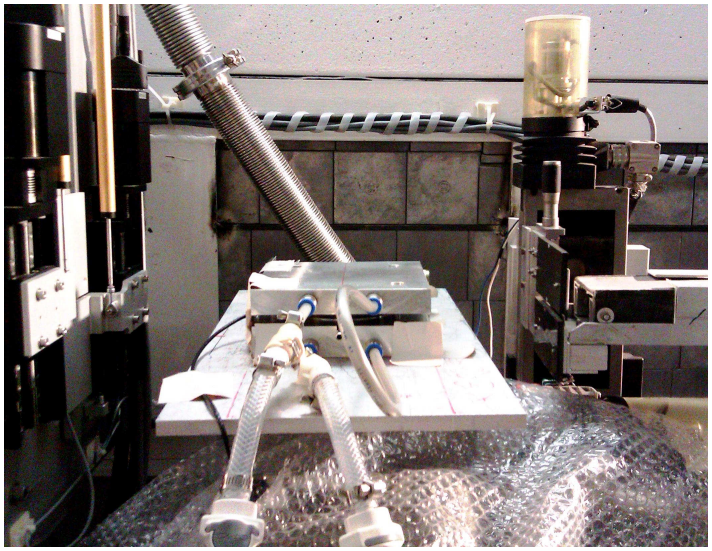

Figure 3.10: NR sample cell mounted to the sample position at the EROS reflectometer (LLB).

For both cells the incident neutron beam assesses the solid-aqueous interface through the solid silicon backing (Figure 3.11).

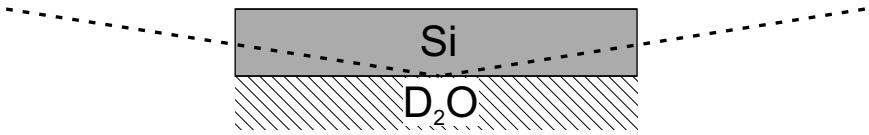

Figure 3.11: Schematic view of the neutron beam through the silicon substrate, reflected at the solid liquid interface.

CHAPTER 4

PAA brushes and proteins - response to elevated hydrostatic pressure

4.1 Outline of experiments

This chapter deals with the adsorption of bovine serum albumin (BSA) to planar polyacrylic acid (PAA) brushes of varied grafting density σ_{PAA} as studied by neutron reflectivity (NR). The PAA brushes were prepared by a Langmuir-Schäfer based grafting of perdeuterated poly(styrene)-b-poly(acrylic acid) block copolymer (dPS-PAA) to dPS pre-coated silicon supports and characterized in their collapsed state at the air-solid interface by X-ray reflectometry (Chapter 4.2). In their solvent-swollen state, NR measurements were conducted at the solid-liquid interface after incubation in buffered D_2O and after the adsorption of BSA from the aqueous liquid phase. From these measurements, detailed volume fraction profiles of the solvent swollen brush $\varphi_{\mathrm{PAA}}(z)$ and the adsorbed BSA $\varphi_{\mathrm{BSA}}(z)$ proteins were obtained. The impact of elevated hydrostatic pressure of 900 bar on the brushes with and without protein uptake was studied, utilizing the Heidelberg high pressure cell for neutron reflectometry [32].

An overview of the samples, investigated by NR at the AMOR time-of-flight reflectometer at SINQ/PSI [90], is given in Table 4.1. Detailed instrumental setup and raw data reduction are given in appendix A.3.2.1.

For all samples A1-A3, at first, the neutron reflectivity of the pure PAA brush was measured in a 10 mM MES D_2O buffered subphase, set to pD 6.1. Second, the hydrostatic pressure was increased to 900 bar to analyze the pressure response of the PAA brush. Third, the pressure was relaxed back to ambient conditions and the reflectivity was measured again to

check for reversibility. After the characterization of the pure PAA brushes, the samples were incubated ex-situ in a 0.5 mg/ml BSA solution for 30 min, followed by subsequent rinsing with the pure D_2O buffer. With the BSA adsorbed to the PAA brush, the samples were remounted to the sample cell and analyzed in a similar pressure sequence of 1 bar, 900 bar and 1 bar. For temperature stability, the sample environment was connected to a water bath at 20 °C.

Details on chemicals, preparation techniques, sample environment and sample characterization are given in Chapter 3.

Table 4.1: Sample overview

Sample	σ_{LB} [nm^{-2}]	σ_{XR} [nm^{-2}]
A1	0.05	-
A2	0.1	0.081 ± 0.008
A3	0.2	0.110 ± 0.010

4.2 Preparation of PAA brushes

The preparation of the PAA brushes utilized the LS transfer (Chapter 3.2.3) of free floating dPS-PAA block copolymer precursor layers with defined grafting densities to dPS pre spin-coated Si substrates.

The amphiphilic diblock-co-polymer dPS_{49}-PAA_{222} was first dissolved for 2 days at 60 °C in dioxane, after which toluene was added to obtain a solution of 1 mg / ml in a 60 % dioxane and 40 % toluene mixture [91]. A defined amount of the solution was spread on the surface of a 10 mM MES buffer subphase in a Langmuir trough (R&K) using a Hamilton syringe. The pH of the buffer was adjusted to 6.1 using NaOH. With movable barriers at a compression of 0.6 cm^2/s the grafting density of the dPS-PAA monolayer for samples A1-A3 was adjusted to values of A1: $\sigma_1 = 0.05\,nm^{-2}$, A2: $\sigma_2 = 0.1\,nm^{-2}$ and A3: $\sigma_3 = 0.2\,nm^{-2}$ and transferred to the dPS coated Si substrate utilizing the Langmuir-Schäfer technique (Chapter 3.2.3). During the preparation, the surface pressure was monitored with a Wilhelmy plate (Figure 4.1).

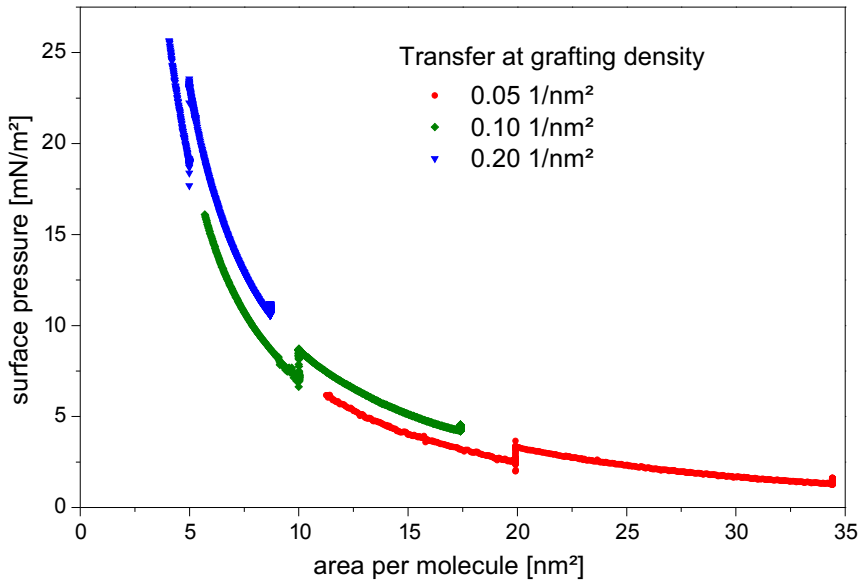

Figure 4.1: Surface pressure - area isotherm of free floating dPS-PAA monolayers at 20 °C and subphase pH of 6.1. Langmuir-Schäfer transfer of the monolayers to dPS-precoated silicon wafers at three different grafting densities is indicated by concurrent drops of the surface pressure in the isotherm.

Analysis of the surface loss area lead to an averaged transfer ratio of 1.3 ± 0.1. Following the brush transfer, the samples were exposed to a second annealing at 120 °C for 15 min. Success of the preparation was confirmed by X-ray reflectometry measurements (Figure 4.2) at the solid-air interface of the coated silicon supports before and after the transfer of the dPS-PAA brushes, with the samples in a dried state. From the SLD profiles in the bottom part of Figure 4.2, the grafting density σ_{XR} is extracted by

$$\sigma_{XR} = \frac{1}{Zr_e} \int_z \left(SLD''(z) - SLD'(z) \right) dz \tag{4.1}$$

$SLD'(z)$ and $SLD''(z)$ are the SLD profiles across the solid-air interface before and after transfer of the dPS-PAA brush, respectively, $Z = 11572$ is the total number of electrons for one dPS_{49}-PAA_{222} polymer molecule and $r_e = 2.82 \cdot 10^{-15}$ m is the classical radius of the electron.

The extracted grafting densities are summarized in Table 4.2. The values measured after the transfer of the brush and the second annealing step were found to be a factor of two higher than expected. This can be explained by the fact that with the transfer of the PAA brush a small film of excess water is attached to the substrate. This water evaporates in the following annealing steps but any dissolved MES buffer salt remains on the samples. By a subsequent extensive rinsing with ultra-pure water, remaining buffer and any nonfixed polymer was removed. The results of the consequent X-ray reflectometry measurements are summarized in the last row of Table 4.2.

Table 4.2: Extracted grafting densities σ from X-ray reflectometry measurements of the samples A1-A3 in the dried state before and after the final rinsing with ultra-pure water.

Sample	grafting density σ [nm^{-2}]			
	prepared	transferred	annealed	rinsed
A1	0.05	0.065 ± 0.005	0.13 ± 0.01	-
A2	0.10	0.13 ± 0.01	0.22 ± 0.02	0.081 ± 0.008
A3	0.20	0.26 ± 0.02	-	0.110 ± 0.010

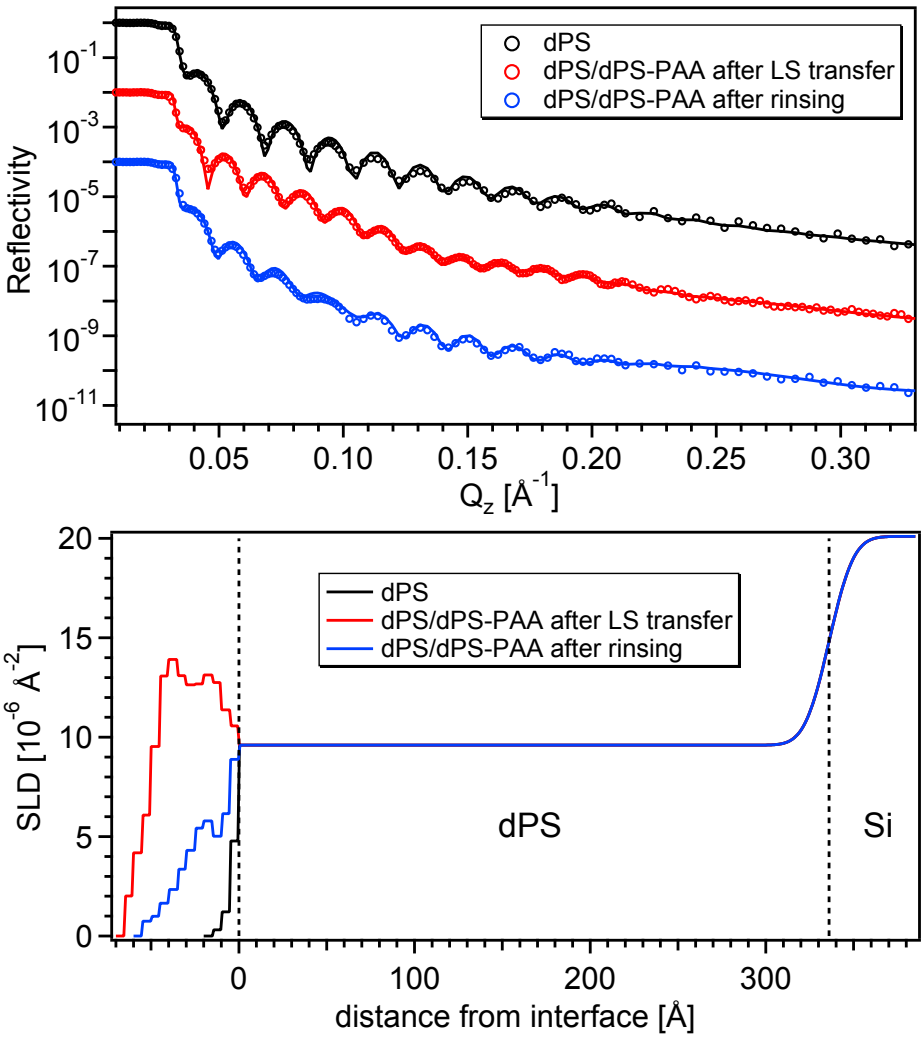

Figure 4.2: X-ray reflectivity and fits (top) and extracted SLD profiles (bottom) of sample A2, grafted at $\sigma_{LB} = 0.1\,\mathrm{nm}^{-2}$.

4.3 Description of PAA brushes - the box model

A polymer brush is formed by the attachment of long polymer chains at one end to an interface. When exposed to a solvent, the free ends of the polymer are stretched into the subphase. The conformation is controlled by polymer-polymer and polymer-solvent interactions, as well as interactions with the grafting interface. Due to confinement, the polymer chains adopt an inhomogeneous volume fraction profile, $\varphi(z)$, normal to the grafting plane [64]. The latter is analyzed by neutron reflectivity. To calculate the reflectivity, the inhomogeneous profile is described by a stack of multiple layers (Chapter 3.3.3). In the SLD profile each layer is represented by a box with the parameters thickness, SLD and roughness to the adjacent layers.

A standard approach for describing polymer brushes is a model with boxes of fixed thickness and roughness. In this model, the reflectivity is fitted by a variation in the number of strata and the SLD for each stratum [40, 46]. It is also possible to fix the number of boxes and fit thickness, SLD and roughness [92].

In this work, the PAA brushes, grafted on a dPS sublayer, are modeled as follows: The dPS sublayer is represented by a box of thickness z_0 as extracted from the precursor X-ray sample characterization (Chapter 4.2). Exclusively at the Si-dPS interface, roughness was incorporated to model the small SiO_2 layer and deviations of the dPS thickness, caused by the spincoating preparation process (Figure 3.1). The profile of the PAA brush was divided into layers, each with 20 Å thickness and no inter-layer roughness. The reciprocal width of the chosen slices is twice the the maximum momentum transfer, $Q_{\max}$, probed experimentally and avoids artificial interferences in the calculated reflectivity curves used for fitting. The required number of strata, representing the PAA brush, are determined in the fitting process. The SLD of PAA was calculated to $\mathrm{SLD_{PAA}} = 2.34 \cdot 10^{-6}\,\text{Å}^{-2}$ at an acrylic acid monomer mass density of 1.051 g/cm^3 [87] and the hydrogen of the acid group exchanged by deuterium in contact with the D_2O liquid fronting phase. The SLD's of all substances in this work are summarized in Table 4.3

Table 4.3: SLD values for the box model describing the planar PAA brushes in D_2O, grafted on a dPS sublayer [81, 87].

Substance	SLD [10^{-6} Å^{-2}]
Si	2.07
dPS	6.4
PAA	2.34
D_2O	6.36

Starting at the grafting plane $\tilde{z} = z - z_0 = 0$, the value of the scattering length density of any given slice of 20 Å thickness of the solvent-swollen PAA brush in D_2O is compiled from the binary mixture of PAA and D_2O in that layer.

$$\mathrm{SLD}_{\mathrm{brush}}(\tilde{z}) = \varphi(\tilde{z}) \cdot \mathrm{SLD}_{\mathrm{PAA}} + (1 - \varphi(\tilde{z})) \cdot \mathrm{SLD}_{\mathrm{D_2O}} \tag{4.2}$$

For the analysis of the reflectivity the Motofit package based on Abeles transfer matrix method was employed [84, 93, 94].

4.4 Results

4.4.1 Planar PAA brushes

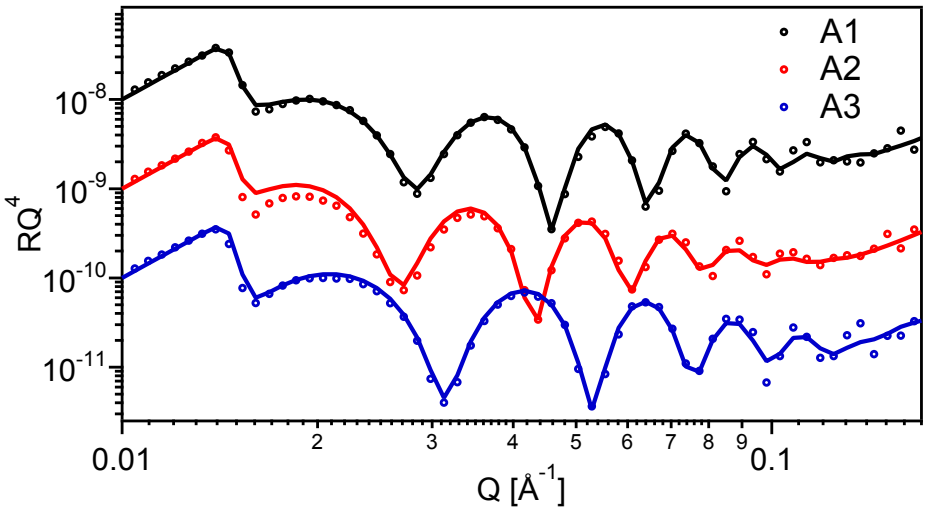

Figure 4.3: NR data and fits for the PAA brushes of samples A1-A3. For visualization, respective data are separated by factors of 10.

Figure 4.3 shows NR data and fits for PAA brushes (A1-A3), grafted on a dPS sublayer, at ambient pressure conditions. The subphase is buffered D_2O. The NR data for all samples exhibit characteristic Kiesig oscillations. The width of these oscillations depends on the thickness of the dPS sublayer. The SLD of dPS ($6.4 \cdot 10^{-6}$ Å^{-2}) and D_2O ($6.36 \cdot 10^{-6}$ Å^{-2}) are nearly perfectly matched. Thus, the shape and height of the Kiesig oscillations are related to the conformation of the protonated PAA brush ($SLD_{PAA} = 2.34 \cdot 10^{-6}$ Å^{-2}).

Figure 4.4 shows the extracted SLD profiles for the PAA brushes, utilizing the box model as described in Chapter 4.3. The extracted SLD profiles of the pure PAA brushes directly yield the information on the polymer brush volume fraction profile, shown in Figure 4.5:

$$\varphi_{PAA}(\tilde{z}) = \frac{SLD(\tilde{z}) - SLD_{D_2O}}{SLD_{PAA} - SLD_{D_2O}} \tag{4.3}$$

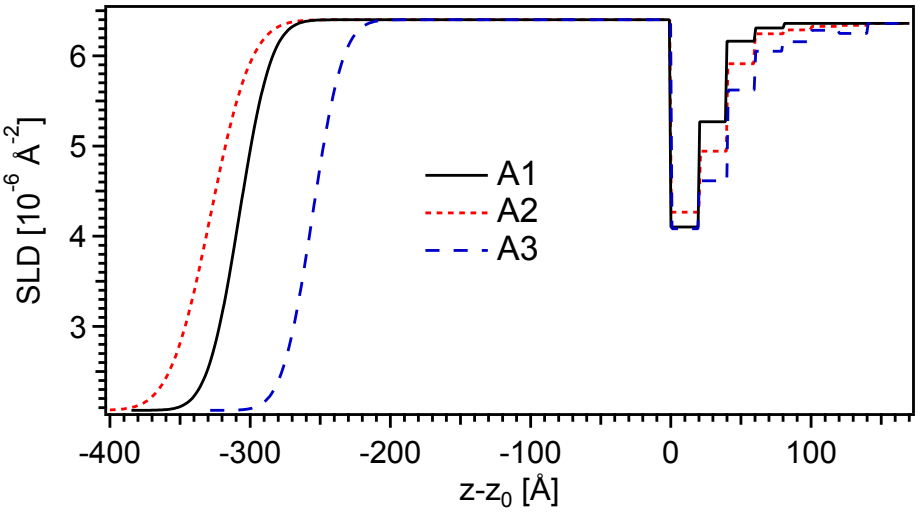

Figure 4.4: Extracted SLD profiles of solvent-swollen brushes A1-A3.

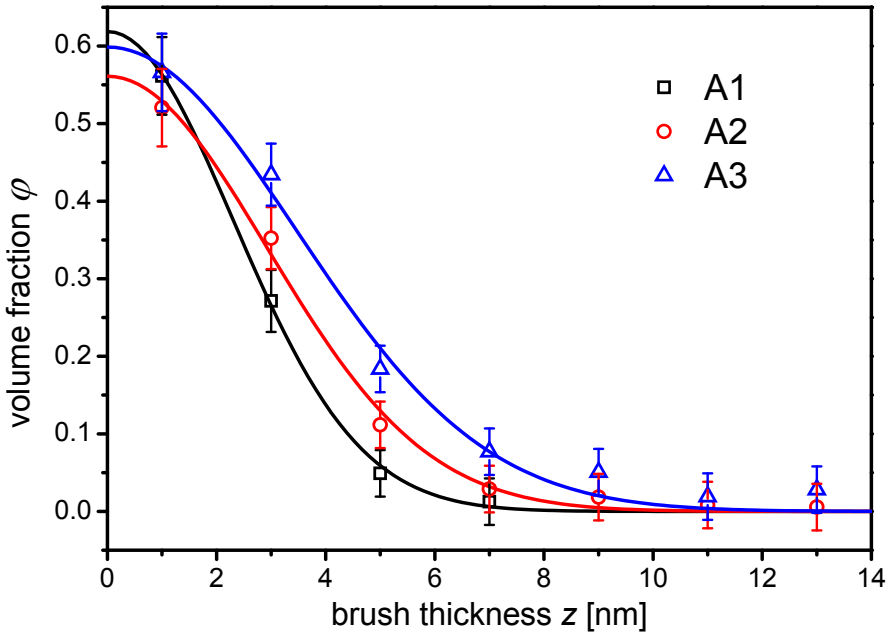

Figure 4.5: Extracted PAA brush volume fraction profiles for samples A1-A3. To improve the visualization of the brush profile, fitted Gaussian peak functions (solid lines) were added to the data.

The extracted PAA brush volume fraction profiles $\varphi_{\mathrm{PAA}}(\tilde{z})$ in Figure 4.5 exhibit a characteristic Gaussian shape. To improve the visualization of this presumption, the discrete experimental volume fraction profile is fitted by a Gaussian peak function

$$\varphi_{\mathrm{Gauss}}(\tilde{z}) = \varphi_0 e^{-\frac{1}{2}\frac{\tilde{z}^2}{\omega^2}} \tag{4.4}$$

The extracted parameters are gathered in Table 4.4. At the grafting interface ($\tilde{z} = z - z_0 = 0$), the PAA brush profiles feature a maximum volume fraction of $\varphi_0 \approx 60 \pm 5\,\%$, independent of the grafting density σ. The latter value is extracted by an integration over the volume fraction profile $\varphi_{\mathrm{PAA}}(\tilde{z})$:

$$\sigma_{\mathrm{NR}} = \frac{1}{N v_{\mathrm{PAA}}} \int_{\tilde{z}} \varphi_{\mathrm{PAA}}(\tilde{z}) \mathrm{d}\tilde{z} \tag{4.5}$$

Where $v_{\mathrm{PAA}} = 115.4\,\text{Å}^3$ is the acrylic acid monomer volume and $N = 222$ the degree of polymerization [87]. For a Gaussian profile with a constant maximum volume fraction $\varphi_0 \approx 60 \pm 5\,\%$ an increasing grafting density is directly related to an increasing thickness ω of the PAA brush.

Table 4.4: Parameters that describe the volume fraction density profile of the PAA brush by a Gaussian peak function (Equation 4.4)

sample	σ [nm^{-2}]	φ_0	ω [nm]
A1	0.070 ± 0.007	0.62 ± 0.06	2.3 ± 0.1
A2	0.082 ± 0.008	0.56 ± 0.06	2.9 ± 0.2
A3	0.106 ± 0.010	0.60 ± 0.06	3.5 ± 0.2

4.4.2 Response to elevated hydrostatic pressure

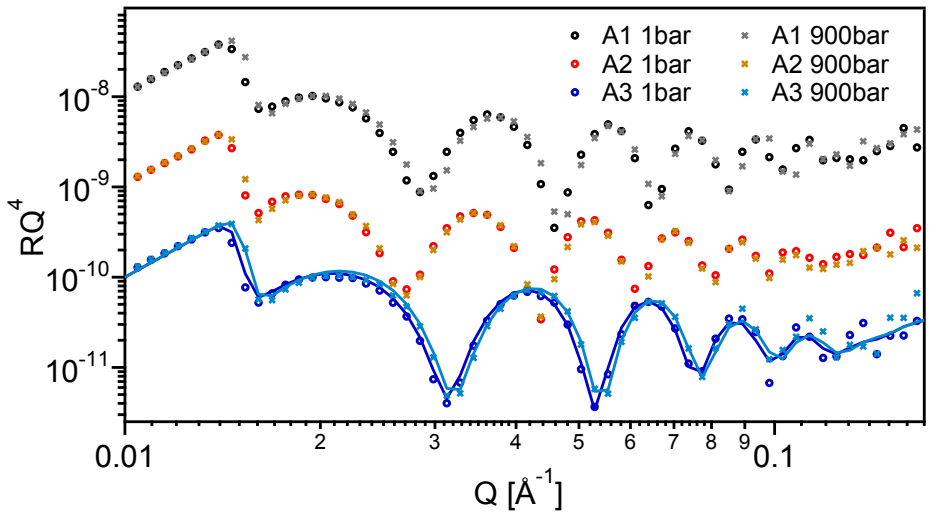

Figure 4.6: NR data for the PAA brushes of samples A1-A3 at 1 and 900 bar. Exemplary fits are added for the NR data of sample A3. For visualization, respective data are separated by factors of 10.

The response of planar PAA brushes to elevated hydrostatic pressure has been examined after the measurements at ambient condition. Figure 4.6 shows the NR data and exemplary fits for sample A3. Increasing the hydrostatic pressure to 900 bar caused a small change of the reflectivity signal. Those changes proved to be fully reversible after pressure relaxation back to ambient conditions.

Two differences in the reflectivity signals at 1 bar and 900 bar are directly visible. First, the total reflection edge is shifted to higher Q-values. This is due to the compression of the D_2O solvent. The SLD of D_2O increased from $SLD_{D_2O}(1\,bar) = 6.36 \cdot 10^{-6}\text{Å}^{-2}$ to $SLD_{D_2O}(900\,bar) = 6.57 \cdot 10^{-6}\text{Å}^{-2}$ and thus shifted the critical angle to higher values (equation 3.15). The second small difference is a shift of the minima positions of the Fresnel oscillations. These positions are related to the total thickness of all layers on the substrate. Here, the main contribution is the thickness of the dPS sublayer. At 1000 bar, bulk polystyrene is compressed by $\approx 2 - 2.5\,\%$ [95, 96]. The respective reduction of the dPS sublayer thickness at an elevated hydrostatic pressure of 900 bar thus yields the shift of the minima positions of $\Delta Q/Q \approx 2\,\%$.

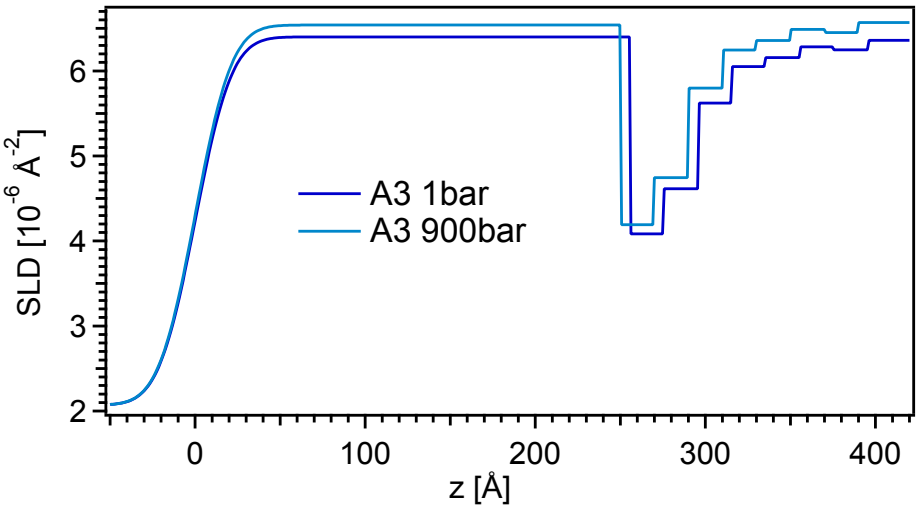

Figure 4.7: SLD profiles for sample A3 at 1 and 900 bar.

The compressibility of D_2O and polystyrene are well described physical parameters that were used to modify the fitted SLD profiles for all samples at 1 bar to match the conditions at 900 bar. Figure 4.7 displays exemplary the modification for sample A3. The SLD of D_2O increased to $6.57 \cdot 10^{-6}$Å^{-2}, the SLD for dPS increased from $6.4 \cdot 10^{-6}$Å^{-2} to $6.53 \cdot 10^{-6}$Å^{-2} and the thickness of the dPS sublayer was reduced by 2 %. Without further adjustment to the structure of the PAA brush, these modifications to the SLD profile resulted in a calculated reflectivity that fits the measured data as shown for sample A3 in Figure 4.6.

In conclusion, elevated hydrostatic pressure of 900 bar does not alter the structure of the solvent-swollen PAA brush.

4.4.3 Protein adsorption

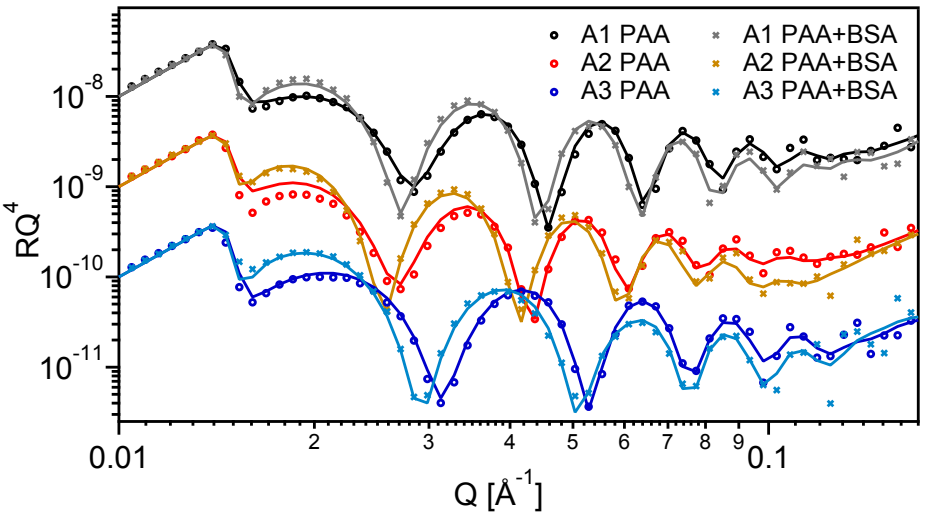

Figure 4.8: NR data and fits for the PAA brushes A1-A3 before and after the adsorption of BSA proteins. For visualization, respective data are separated by factors of 10.

Figure 4.8 shows the change of the NR data and fits after the adsorption of BSA to the PAA brushes. The differences are more distinct compared to the changes of the PAA brush at elevated hydrostatic pressure. The shift of the Kiesig oscillations to lower Q-values is related to an increase of the brush thickness. This is a direct indication of the successful binding of BSA proteins to the PAA brush.

The extracted SLD profiles are displayed in Figure 4.9. When BSA adsorbs into the PAA brush, D_2O inside the brush is replaced by protein [40, 46]. The neutron SLD of BSA, $SLD_{BSA} = 3.19 \cdot 10^{-6}$ Å^{-2} [97], is lower than that of D_2O, $SLD_{D_2O} = 6.36 \cdot 10^{-6}$ Å^{-2}, resulting in a decreased SLD of the respective slab in the box model (Figure 4.9).

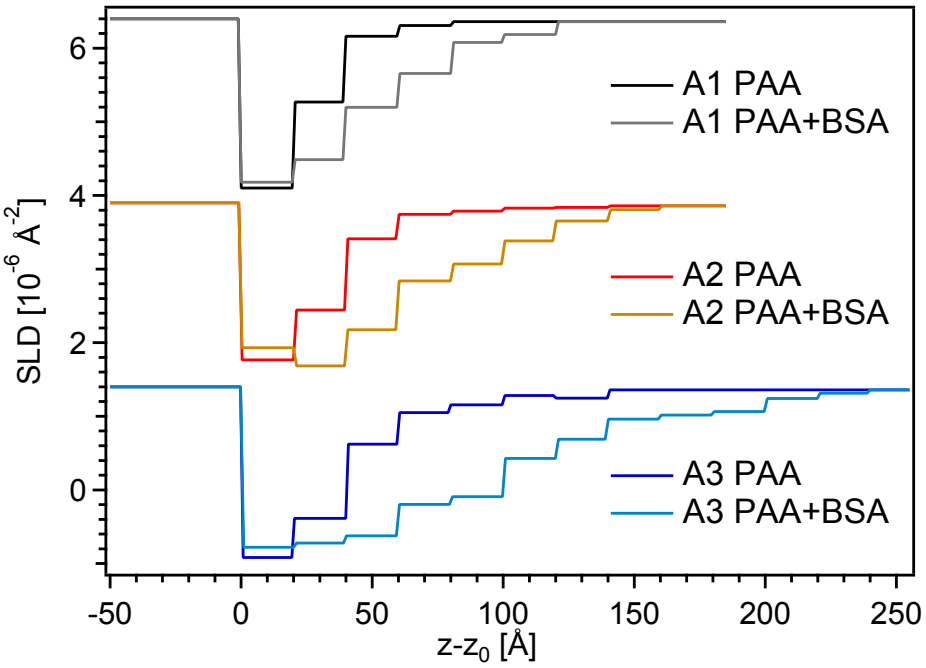

Figure 4.9: SLD profiles of the PAA brushes A1-A3 before and after the adsorption of BSA proteins. For visualization, respective SLD data are separated by values of $2 \cdot 10^{-6}$ Å^{-2}.

Integration over the difference of the SLD profiles before and after adsorption of BSA yields the adsorbed mass of BSA per surface area Γ_{NR}

$$\Gamma_{NR} = \frac{M_{BSA}}{V_{BSA}} \int_{\tilde{z}} \frac{SLD^{\star}(\tilde{z}) - SLD(\tilde{z})}{SLD_{BSA} - SLD_{D_2O}} dz \tag{4.6}$$

where $SLD(\tilde{z})$ and $SLD^{\star}(\tilde{z})$ are the extracted SLD profiles before and after protein adsorption, $M = 66267$ g/mol is the molar mass and $V = 48574\,cm^3$/mol (80660 Å^3/molecule) is the molar volume of BSA [97]. The calculated amount of adsorbed protein per surface area for the three measured grafting densities is shown in Figure 4.10. A linear correlation between adsorbed amount of protein and grafting density is found.

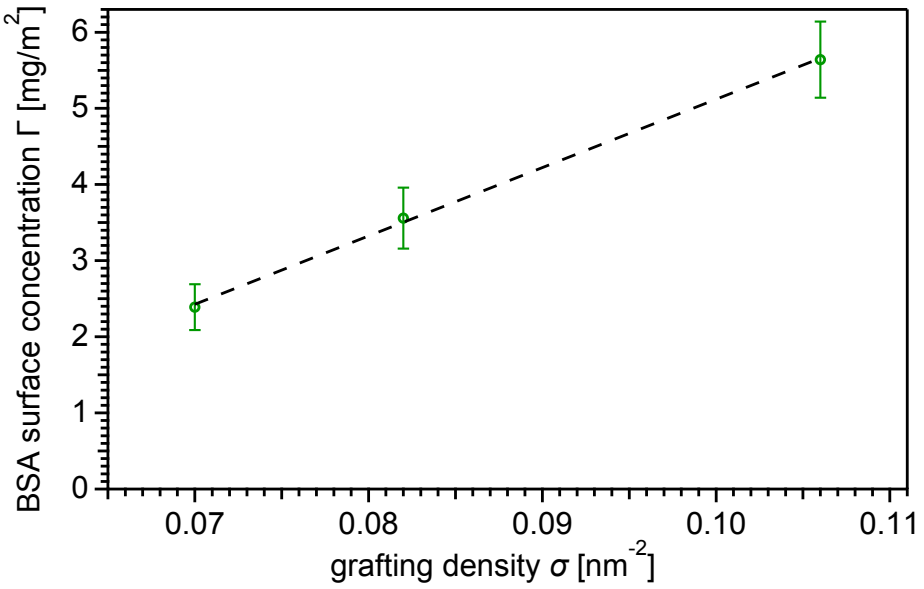

Figure 4.10: Adsorbed amount of BSA per surface area for samples A1-A3. Note the linear correlation of Γ_{BSA} and σ.

The difference of the SLD profiles before and after adsorption also provides information on the spatial distribution of adsorbed BSA. For the explicit calculation of the BSA volume fraction profile further assumptions concerning the PAA brush after completion of the adsorption process have to be made. The extended analysis in that respect is part of the discussion in Chapter 4.5.2.

4.4.4 Proteins and pressure

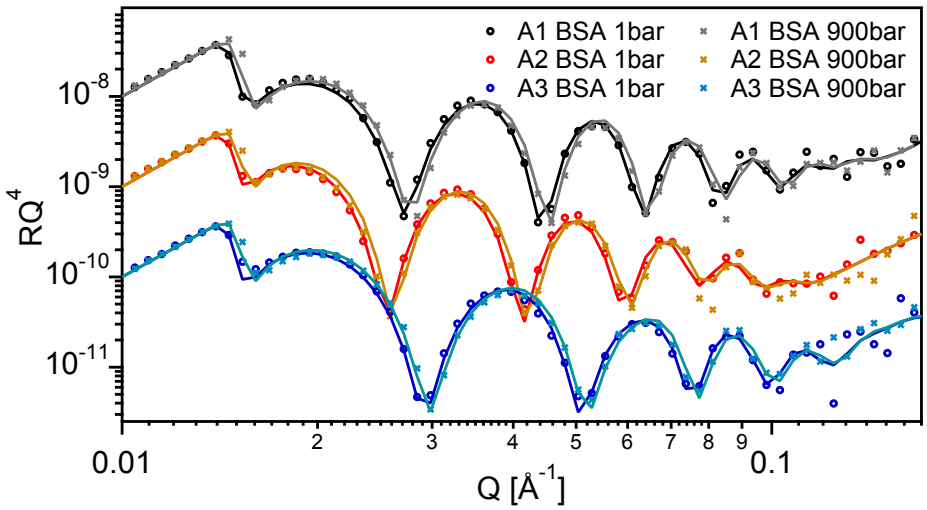

Figure 4.11: NR data from the PAA brushes A1-A3 after adsorption of BSA at 1 and 900 bar. For visualization, respective data are separated by factors of 10.

Figure 4.11 shows the NR data at 1 and 900 bar for the PAA brushes (A1-A3) after the adsorption of BSA proteins. The changes of the reflectivity are comparable to the results obtained from the pure PAA brush at 900 bar (Chapter 4.4.2). All changes of the reflectivity are fully explained by the compression of the dPS sublayer and the D_2O solvent. The profiles of the BSA containing PAA brushes are not affected by an elevated hydrostatic pressure of 900 bar. In conclusion, elevated hydrostatic pressure does not affect the binding of BSA.

4.5 Discussion

4.5.1 Planar PAA brushes

The extracted volume fraction profiles of the PAA brushes, Figure 4.5, exhibit a characteristic Gaussian shape with a maximum volume fraction $\varphi_0 \approx 60\,\%$ at the grafting plane. The Gaussian polymer brush conformation is in line with theoretical SCF calculations [68, 69, 73] and experimental results from NR [74, 75]. For dPS-PAA brush systems, as prepared in this work, NR data is available on samples utilizing the same preparation technique and comparable block copolymers [50]. Hollmann et al. extracted density profiles that featured a maximum volume fraction $\varphi_0 \approx 45\,\%$ at a distance of $\tilde{z} \approx 5\,\text{nm}$ away from the grafting plane. For higher distances a comparable Gaussian like decay of the brush density was found. The differing results for the brush volume fraction near the grafting plane in this work and the publication by Hollmann et al., might arise from utilizing different substrates. Hollmann et al. worked with rectangular silicon blocks ($80\,\text{x}\,50\,\text{x}\,15\,\text{mm}^3$). Spincoating of polymers on non rotation-symmetric substrates produces visibly increased layer thicknesses at the edges. A pre-characterization of the samples with X-ray reflectometry only probes the homogeneous center of the substrate. In contrast, the footprint of NR measurements covers nearly the whole sample and thus a variation of thickness of the dPS sublayer at the sides of the samples contributes to the specular reflectivity in the same way as roughness at the grafting plane between dPS and PAA would do. This effect might explain the extracted volume fraction profiles as published by Hollmann et al., where the maximum brush density is shifted away from the expected grafting plane. In this work, the substrates were changed to rotation-symmetric circular silicon disks to achieve more uniform spincoated dPS sublayer. The improved homogeneous coating resulted in well defined dPS-PAA grafting interfaces with sharp transitions between dPS and PAA.

Experimental PAA brush profiles compared to theoretical results

Polymer brushes of PAA belong to the class of weak annealed polyelectrolyte brushes. Hence, the diagram of states of such systems as derived by Zhulina and Borisov [68] should apply to the system experimentally investigated here. For comparison of experimental and theoretical results, the physical parameters of the PAA brushes were transferred into the reduced dimensionless parameter space of Zhulina and Borisov, with the relation between the volume fraction $\varphi(\tilde{z})$ and the monomer density profile $c_{\mathrm{AA}}(\tilde{z})$ of the brush segments being

$$c_{\mathrm{AA}}(\tilde{z}) = \frac{\varphi(\tilde{z})}{V_{\mathrm{AA}}} \tag{4.7}$$

$V_{\mathrm{AA}} \approx 0.115\,\mathrm{nm}^3$ is the monomer volume of an acrylic acid monomer at a mass density of $1.051\,\mathrm{g/cm}^3$ [87]. A single PAA polymer chain consists of $N = 222$ monomers with monomer length a.

$$a \approx \sqrt[3]{\frac{6V_{\mathrm{AA}}}{\pi}} \approx 0.58\,\mathrm{nm} \tag{4.8}$$

The chains are grafted to the interface with the grafting density $\sigma = 1/s$, where s is the grafting area per chain. For an experimentally extracted $\sigma \approx 0.1\,\mathrm{nm}^{-2}$, $s \approx 10\,\mathrm{nm}^2$. The ionic strength of a 10 mM monovalent MES buffer at pH 6.1 is $C_s \approx 5$ mM. The concentration of hydrogen C_{H^+}, here the concentration of deuterium ions $C_{\mathrm{D}^+} \approx 8 \cdot 10^{-7}$ mol/l, is set by the pD = 6.1 of the D_2O buffer. The dissociation constant K_a of the PAA monomer unit is given by its pK_a value. The value for free acrylic acid monomers is $pK_a = 4.35$ [98]. For polymerized acrylic acid the pK_a shifts to higher values depending on salt concentration and degree of polymerization [99]. For the experimental values used in this work, the pK_a approximately equals the pD value of the buffer solution, thus $K_a \approx 8 \cdot 10^{-7}\,\frac{\mathrm{mol}}{\mathrm{l}}$. The degree of ionization $\alpha_b \approx 0.5$ of an acidic group of the free PAA polymer in a buffered solution is given by the mass action law

$$\frac{\alpha_b}{1-\alpha_b} = \frac{K_a}{C_{\mathrm{D}^+}} \tag{4.9}$$

The physical properties can now be transformed to dimensionless parameters as defined by

Zhulina and Borisov (equation 38-41 of reference [68]), namely

reduced distance:

$$t = b\tilde{z} = \sqrt{\frac{3\pi^2}{8}}\frac{\tilde{z}}{aN} \tag{4.10}$$

reduced polymer surface coverage with Bjerrum length $l_B = 0.71\,\text{nm}$ for water at 25°C:

$$\nu = 4\sqrt{\frac{2}{3}}\frac{a l_B N^2}{s} \tag{4.11}$$

"strength" of tethered polyacid :

$$u = \frac{16}{3\pi}a^2 l_B K_a N^2 \tag{4.12}$$

relative salt content:

$$\Phi = \frac{C_s}{C_{H^+}} \tag{4.13}$$

With the experimentally specified set ($b \approx 0.015\text{nm}^{-1}$, $\nu \approx 6630$, $u \approx 9.6 \cdot 10^{-3}$, $\Phi \approx 6250$) the PAA brush is located in the *osmotic annealing regime* of the Zhulina-Borisov diagram of states. In this regime, both polymer density and electrostatic potential vary substantially throughout the brush. The degree of ionization $\alpha(\tilde{z})$ also varies and the value $\alpha(0)$ at the grafting point differs significantly from the value $\alpha(H) \approx \alpha_b$ for the chain ends, stretched into the buffer solvent. The theoretically calculated density profiles for a brush in the osmotic annealing regime exhibit a characteristic Gaussian shape, which in fact compares well with the experimental results. Explicit calculation, using the derived reduced parameters, produces a theoretical brush with a density profile 4-5 times more stretched than the experimental one (Figure 4.12). To match the calculated profile with the experimental one, the degree of ionization of the PAA brush in its buffer solvent has to be reduced to $\alpha_b \approx 0.1$ which is reached at a pD ≈ 5.2. This is in contradiction to the experimentally adjusted value of pD 6.1.

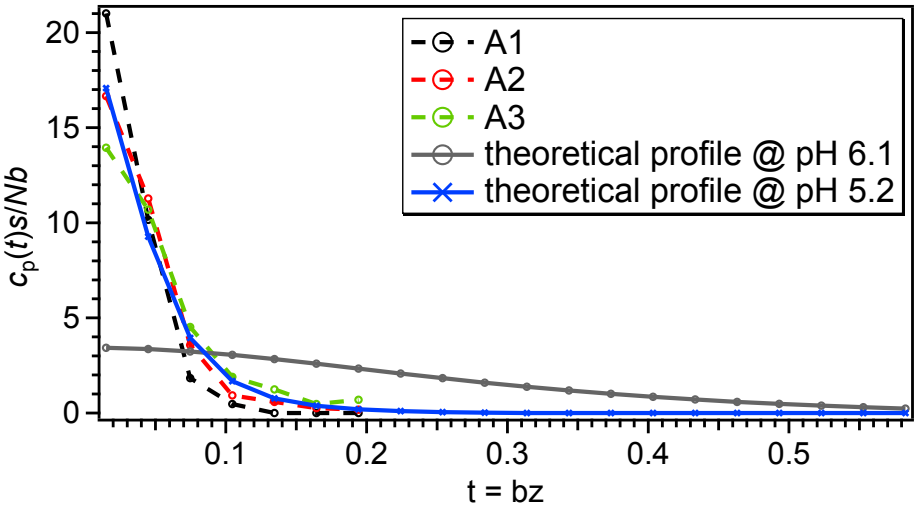

Figure 4.12: Reduced experimental density profiles for samples A1-A3 compared to theoretical profiles calculated with the analytical PB-SCF model by Zhulina and Borisov [68] for two buffer pH values.

A trivial experimental explanation for the discrepancy might be an error in the measurement of the pH value. The difference of $\Delta\text{pD} = 0.9$ is more than the typical error of a glass electrode (± 0.1), but a malfunction of the instrument due to prior treatment can not be excluded completely.

On the theoretical side it must to noted, that the approximations in self consistent field theory are only eligible for very long polymer chains ($N \to \infty$). The limited lengths of the polymer chains of the experimental PAA brush might cause the different results. An important aspect here are boundary effects, not included in the theoretical calculations. No attractive or repulsive forces with respect to the interface were taken into consideration in the latter case. Those however can strongly influence the shape of the brush profile [73].

The dPS sublayer exhibits a hydrophobic interface. NR studies on the solid-liquid dPS/D_2O interface revealed a D_2O depletion layer with a thickness of 2-5 nm [100]. In this work, the dense PAA layer with a thickness of ≈2-4 nm might act as a screening layer between the hydrophobic dPS sublayer and the D_2O solvent. This confinement could produce a carpet layer that prevents further stretching of the PAA brush. For higher grafting densities or longer polymer chains such high density screening layers (carpet layers) have been observed experimentally and are found to remain at a constant thickness [101]. In a good solvent the

additional polymer material, which is not needed to screen the hydrophobic interface, creates the undisturbed stretched polymer brush part [101–103]. In conclusion of this work, the degree of polymerization $N = 222$ of the PAA polymers and the grafting density $\sigma \approx 0.1\text{nm}^{-2}$ are not large enough to create more than a dense screening layer. This screening layer has a Gaussian shape with chain ends partly stretched into the D_2O solvent.

Electrostatic properties of the PAA brush

Key to the understanding of the adsorption of proteins is the knowledge of the electrostatic properties of the polyelectrolyte brushes. A characteristic of weak polyelectrolyte brushes in the osmotic annealed regime is the inhomogeneous ionization $\alpha(\tilde{z})$ of the monomers along the brush, normal to the grafting plane (z-direction). The high monomer density within the brush results in a local suppression of charges. The relative PAA monomer charge profile $\alpha(\tilde{z})$ can be calculated by applying the local electroneutrality approximation (LEA) in combination with the Langmuir-Boltzmann relation

$$\alpha(\tilde{z}) = \frac{\mathrm{C}e^{\phi(\tilde{z})}}{1+\mathrm{C}e^{\phi_D(\tilde{z})}} \tag{4.14}$$

with

$$\mathrm{C} = \frac{K_\alpha}{\mathrm{C}_D^+} \tag{4.15}$$

and the Donnan Potential $\phi_D(\tilde{z})$

$$e^{\phi_D(\tilde{z})} = \frac{\alpha(\tilde{z})c_m(\tilde{z})}{2\mathrm{C_s}} + \sqrt{\left(\frac{\alpha(\tilde{z})c_m(\tilde{z})}{2\mathrm{C_s}}\right)^2 + 1} \tag{4.16}$$

Utilizing the Donnan Potential in eq. 4.14, the relative monomer charge profile $\alpha(\tilde{z})$ can be solved self consistently. An exemplary result for sample A3 is shown in Figure 4.13 (top). The charge ratio of the acidic groups is highly suppressed at the grafting plane. For a volume fraction density $\varphi_0 \approx 60\,\%$ (Table 4.4) at the grafting point only $\approx 3\,\%$ of the acidic monomers are dissociated. Thus, the effective pD inside the brush is also reduced when compared to the equilibrium value of the buffer solution. The minimum effective pD within the brush is ≈ 4.6.

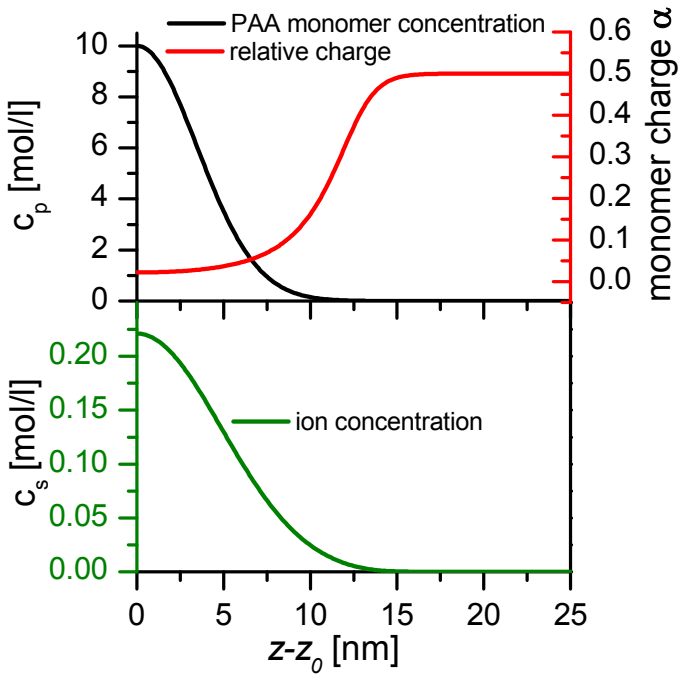

Figure 4.13: Analytical Gaussian monomer density profile $c_m(\tilde{z})$ for sample A3 together with the self consistently solved relative monomer charge profile $\alpha(\tilde{z})$ (top) and counterion distribution $c_s(\tilde{z})$ (bottom).

With decreasing monomer density, i.e. moving away from the grafting plane, the relative charged fraction of monomers is increasing to finally reach the value $\alpha_b = 0.5$ of the free polymer at pD 6.1. In the LEA the sum of all positive charges equals the sum of all negative charges on a local scale. In this approximation the local counterion concentration $c_s(\tilde{z})$ in the brush equals the local density of charged monomers $\alpha(\tilde{z}) \cdot c_m(\tilde{z})$ (Figure 4.13, bottom panel). Despite the suppression of charges, the counterion concentration at the grafting point is increased by a factor of 8 as compared to the buffer solution, simply due to the enrichment of acrylic acid monomers. The increased concentration of counterions inside the brush is an important feature in the interpretation of the adsorption of BSA at the wrong side of the isoelectric point (IEP) [40, 104].

4.5.2 Protein adsorption

PAA polyelectrolyte brushes are net negatively charged in the buffer solution at adjusted pD 6.1. The experimental IEP for BSA is in the range of 4.7-5 [105] resulting in a similarly net negative protein charge. Working against electrostatic repulsion, BSA adsorbs into the PAA brush on the wrong side of the IEP [39, 40, 43, 46–49], as also observed in this work. A reasonable explanation is given by an entropically driven process based on the release of confined counterions in the adsorption process [39, 40, 104].
A second reason for the adsorption of BSA to the osmotic annealed PAA brush is the reduced effective pD inside the brush. Resultant charge regulation also affects the electrical properties of the BSA protein. The minimum effective pD of 4.6 inside the brush is below the IEP of BSA. The impact on the protein is a neutralization and thus a reduced effective electrostatic repulsion. Even an inversion of the protein charge seems possible [47, 106, 107].
Counterion release and charge regulation both contribute to the overall adsorption process. As long as the ion concentration in the brush is substantially higher than the equilibrium concentration in the buffer solution and the protein exhibits patches of positive and negative charges, there is an entropic component to the adsorption based on the release of counterions [108]. In the osmotic annealed regime, charge regulation causes a reduced effective pD inside the brush compared to the buffered value. Thus, protein neutralization or charge inversion are also reasonable factors for the adsorption process.

Integral amount of adsorbed BSA

Figure 4.10 showed the integral amount Γ of BSA adsorbed on planar PAA brushes as a function of grafting density σ. With increasing σ, more proteins were found to bind to the PAA brush. This result can be explained by the increasing number of binding sites with increasing brush thickness, consistent with the results by de Vos et al. [47].
The extracted values of $\Gamma = 2.4$ to $5.6\,\mathrm{mg/m^2}$ are comparable to values reported for similar planar PAA brushes [46, 47]. At pD $= 6$ and $\sigma = 0.1\,\mathrm{nm^{-2}}$ Hollmann et al. extracted $\Gamma = 1.4\,\mathrm{mg/m^2}$ for a 10 times lower concentration of BSA (0.05 mg/ml in buffer solution). A reduced amount of bound BSA for a lower concentration of dissolved BSA is in line with

the results from parametric studies concerning this issue [39, 47]. In conclusion, the overall results for the integral amount of adsorbed BSA proteins Γ to planar PAA brushes in this work are consistent with literature.
In the following, the discussion on the spatial distribution of bound BSA with respect to the PAA brush conformation will give further insight in the adsorption process.

Spatial distribution of BSA inside planar PAA brushes

The information on the integral amount of adsorbed proteins to polymer brushes is available using lab methods such as ultra-filtration for spherical polyelectrolyte brushes [39] or optical reflectometry [47] and surface plasmon resonance spectroscopy [48] for planar brushes. The advantage utilizing NR is the information on the spatial distribution of bound proteins inside the polymer brush. In this work however, with only one D_2O/H_2O contrast, it was not possible to directly distinguish the $\tilde{z}$-resolved mixing ratio of BSA, PAA and D_2O. The profile for one of the components had to be fixed by an initial presumption. The first intuitive assumption is that there is no conformational change of the PAA brush upon loading with BSA [40]. In the case of a conserved PAA brush, the $\tilde{z}$-resolved BSA volume fraction profile $\varphi(\tilde{z})_{\mathrm{BSA}}$ can be extracted directly from the difference of the SLD profiles [40].

$$\varphi(\tilde{z})_{\mathrm{BSA}} = \frac{\mathrm{SLD}^{\star}(\tilde{z}) - \mathrm{SLD}(\tilde{z})}{\mathrm{SLD}_{\mathrm{BSA}} - \mathrm{SLD}_{\mathrm{D_2O}}} \tag{4.17}$$

The isolated profiles are shown in Figure 4.14. Within the absolute error of the calculated values, the assumption of a conserved PAA brush results in a small negative adsorbed amount of protein close to the anchoring plane of the brush. This result may hint to a stretching of the PAA brush with the adsorption process. An assumed stretching of the PAA brush profile also changes the BSA volume fraction profile. This leads to a second model with a stretched PAA brush.
First, the results for the conserved PAA brushes will be discussed (Figure 4.14), followed by the results for the stretched PAA brush profiles.

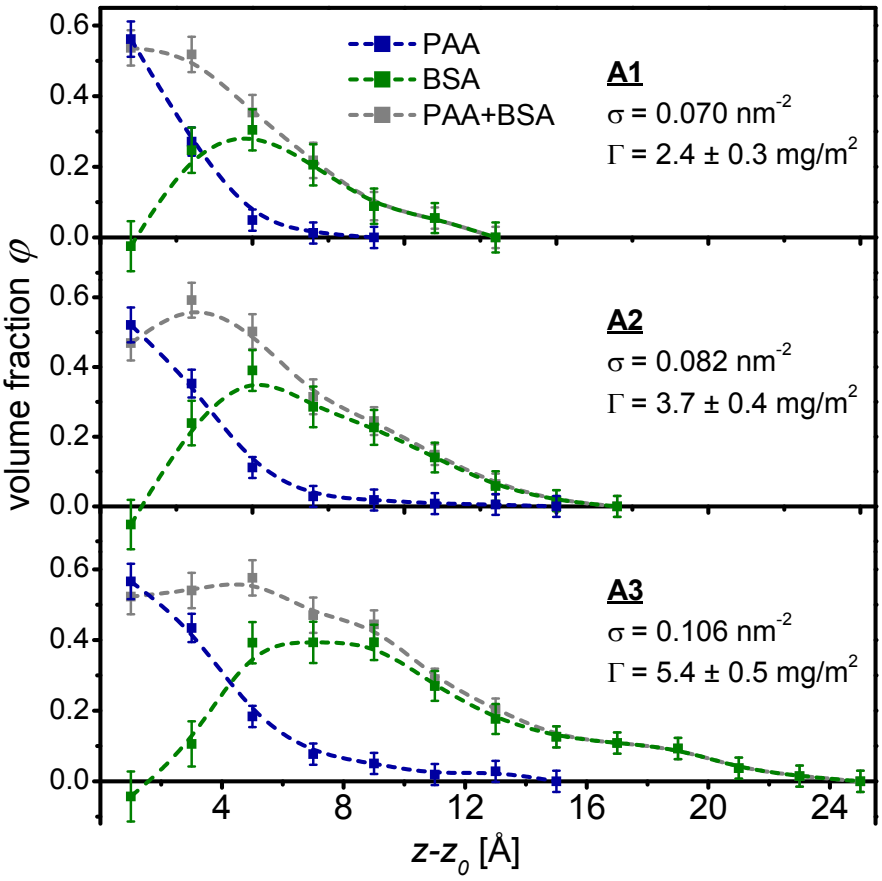

Figure 4.14: Volume fraction profiles of the conserved PAA brush and adsorbed BSA for samples A1-A3 with increasing grafting density. Smoothed lines were added to guide the eye.

Conserved PAA brush

The PAA brush adopts a very dense structure with PAA volume fractions $\varphi > 50\,\%$ in the first 2 nm slab, near the grafting interface to the dPS sublayer. Dense polymer brushes are known to be resistant to protein adsorption [109]. Compared to the brush, BSA is a relatively big molecule (Figure 4.15) with dimensions in the range of 6-8 nm [97, 110, 111].

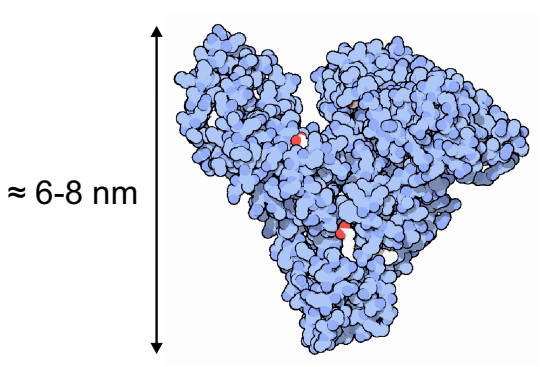

Figure 4.15: Heart shaped structure of serum albumin proteins, from RCSB Protein Data Base [112].

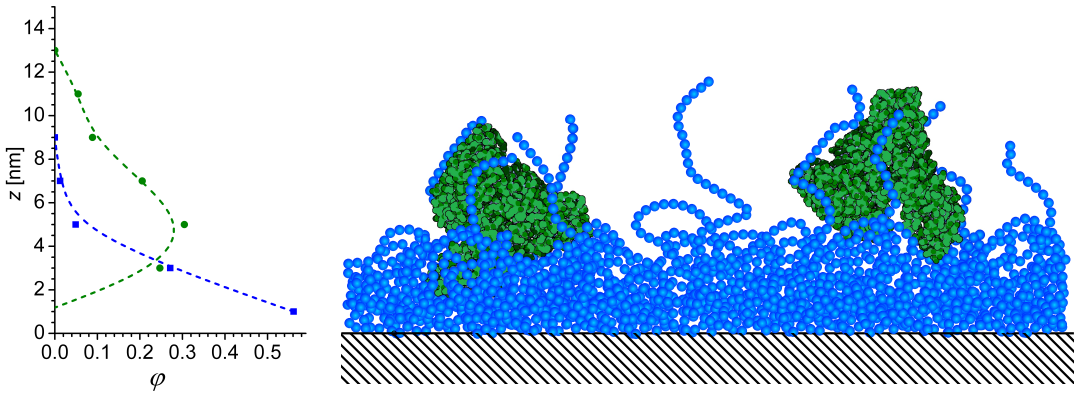

Figure 4.16: Schematic PAA and BSA volume fraction profile for the conserved PAA brush model based on the analysis of sample A1 (see also Figures 4.5 and 4.14).

Large proteins can approach the surface only by compression of the polymer brush. The free energy penalty, associated with further compression and compaction of the brush, favors adsorption of the protein at the outer surface of the brush [109]. The extracted protein volume fraction profiles of Figure 4.14 directly support this model. Especially for the lowest grafting

density $\sigma = 0.07\,\mathrm{nm}^{-2}$ (A1), the volume fraction profile of adsorbed BSA describes the adsorption of a BSA monolayer on top of the dense part of the PAA brush (Figure 4.16). The diluted Gaussian PAA chain ends provide a soft environment for the adsorbed protein, while the dense PAA inner layer screens the hydrophobic dPS sublayer and thus also helps to preserve the native protein structure [37, 38].

Stretched PAA brush

If the brush is stretched during the adsorption process, an assumption has to be made to describe the resultant PAA brush profile. A simple model is the linear stretching of the PAA brush by a factor depending on the differences of the rms thickness of the brush before and after protein adsorption (Figure 4.17).

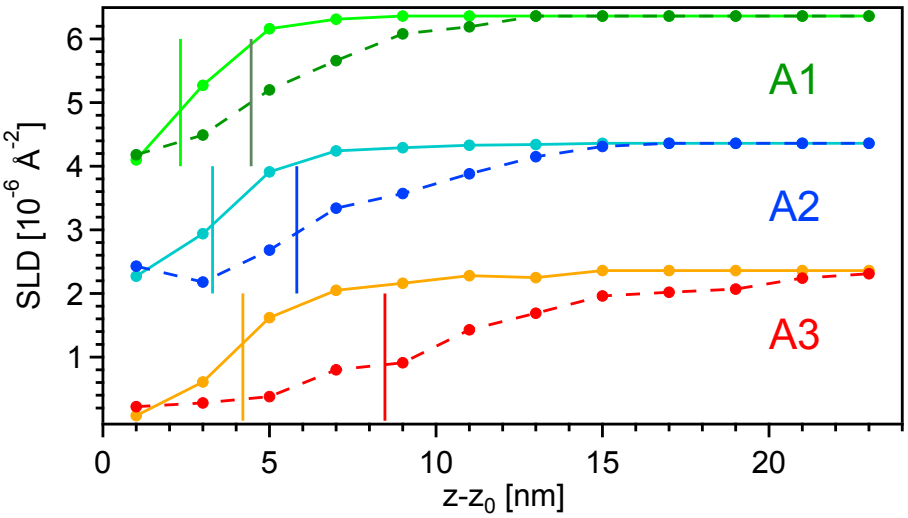

Figure 4.17: SLD profiles of the PAA brushes A1-A3 before (solid lines) and after (dashed lines) the adsorption of BSA. The SLD values for sample A2 and A3 are shifted by $-2 \cdot 10^{-6}$ Å^{-2} and $-4 \cdot 10^{-6}$ Å^{-2}, respectively, to avoid overlapping. The vertical bars denote the position of the respective rms thickness that were used to calculate a stretching factor for the PAA brush with bound BSA proteins.

A mean stretching factor of 1.9 ± 0.2 was extracted, resulting in a brush that is extended to nearly twice its original length upon adsorption of BSA. The specific modification was applied to the Gaussian fits of the PAA brush profiles with the respective stretching factor calculated individually for each sample A1-A3. Figure 4.18 shows the resulting profiles and

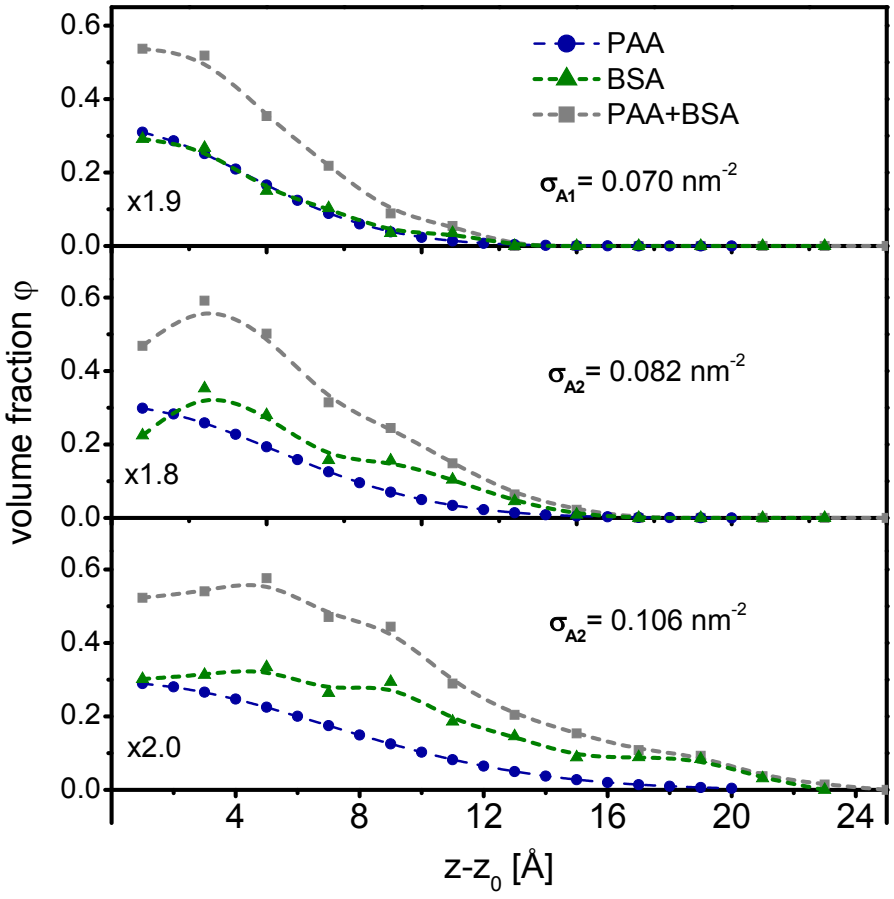

Figure 4.18: Volume fraction profiles of stretched PAA brushes and adsorbed BSA with increasing grafting density. Smoothed lines were added to guide the eye.

also includes the modified results for BSA. The density profiles of adsorbed BSA follow the density of the PAA brush. A non-zero volume fraction of the BSA is found directly at the grafting interface to the dPS sublayer.

Comparison of conserved and stretched PAA brush model after protein adsorption

Figures 4.14 and 4.17 show the volume fraction profiles of PAA and BSA after the adsorption process for the assumptions of conserved and stretched PAA brushes. The main difference of both models is the adsorption of BSA either on top of the dense PAA screening layer for the conserved PAA brush or the penetration of BSA into this layer down to the dPS grafting plane in case of the stretched PAA brush. Purely based on the available

experimental data both models are valid to describe the adsorption of BSA. In the case of the conserved brush, the non-physical negative amount of adsorbed BSA can be set to zero within the absolute error of the determined value. The adsorption on top of the dense PAA screening layer is consistent with the protein resistance of dense polymer structures [109]. The preservation of the protein structure also supports zero adsorption next to the hydrophobic dPS sublayer, in-line with literature [37, 38].
The adsorption on top of the planar PAA brush seems to contradict measurements on spherical polyelectrolyte brushes (SPB). There, BSA was found deep inside the PAA brush [43, 44]. Those results favor the extracted BSA density profiles as based on the stretched PAA brush model. However, direct comparison of SPB brushes and the planar brushes of this work is not straightforward. The thickness of the spherical PAA brushes was larger than 50 nm and thus 3-5 times larger than the maximum thickness of the planar PAA brushes before adsorption in this work. In a brush with a thickness of > 50 nm a dense 2-3 nm screening layer at the grafting plane is negligible. The accessible diluted part of the spherical PAA brush for protein adsorption amounts to 95 %. For the smaller planar brushes in this work the dense screening or carpet layer covers up to 30 % of the total brush thickness and thus directly affects the adsorption process. The adsorption of BSA on top of dense, thin PAA brushes, as suggested by the model of the conserved brush, is not in contradiction to existing results on the adsorption of BSA inside thick colloidal PAA brushes. With the protein resistance of dense polymer brushes, the conserved PAA brush model seems to be preferable to the model of the stretched brush.

Up to this point the comparison between the conserved and stretched brush model is exclusively based on the protein distribution related to the PAA brush profile, irrespective of the integral amount of bound BSA. With increasing grafting density σ the integral amount Γ of adsorbed BSA also increases in a linear fashion (Figure 4.10). That is not true for the ratio $\kappa = \frac{\Gamma}{\sigma m_{\mathrm{BSA}}}$ of the average relative number of bound BSA proteins per PAA chain, where $m_{\mathrm{BSA}} = 1.1 \cdot 10^{-19}$ g is the mass of a single BSA molecule [97]).

With increasing grafting density σ also κ increases (Table 4.5). If BSA can bind to any

Table 4.5: Number κ of bound BSA proteins per grafted PAA monomer, related to the grafting density σ. The mass of one BSA protein is $m_{\mathrm{BSA}} = 1.1 \cdot 10^{-19}$ g (M = 66267 g/mol).

sample	σ [nm^{-2}]	Γ [mg/m^2]	$\kappa = \frac{\Gamma}{\sigma m_{\mathrm{BSA}}}$ [$\frac{\mathrm{BSAproteins}}{\mathrm{PAAchain}}$]
A1	0.070 ± 0.007	2.4 ± 0.3	0.31 ± 0.06
A2	0.082 ± 0.008	3.6 ± 0.4	0.40 ± 0.08
A3	0.106 ± 0.010	5.6 ± 0.5	0.48 ± 0.09

position inside the PAA brush, as is the case for the stretched PAA brush model, κ is expected to be constant. In case of the conserved PAA brush model, the dense PAA screening layer is not penetrated by BSA. Adsorbed proteins are found purely in the diluted outer part of the brush. With the completion of the screening layer, its relative contribution to the total brush thickness should decrease with increasing grafting density. Thus, κ should converge to a plateau value in the long chain limit. The experimental results gathered in Table 4.5 are in-line with expectation. In conclusion, the extracted integral amount of adsorbed BSA proteins also supports the model of the conserved PAA brush.

4.5.3 Effects of elevated hydrostatic pressure

PAA brushes and pressure

As demonstrated in Chapter 4.4.2, the application of hydrostatic pressure of 900 bar does not change the conformation of the solvent-swollen PAA brushes. All changes to the reflectivity are fully explained by the increased density of the D_2O subphase and dPS sublayer, concomitant with a pressure-induced reduction of thickness of the latter. The PAA brush is hydrophilic at pD 6.1. Thus, in a fully solvated PAA brush there are no solvent inaccessible cavities that are affected by elevated pressure (Chapter 2.3).

Adsorbed proteins and pressure

The results compiled in Chapter 4.4.4 also showed no response of the combined PAA and BSA volume fraction profiles to elevated hydrostatic pressure of 900 bar after the adsorption of BSA. No measurable desorption or re-ordering of the bound proteins was found. As hydrostatic pressure weakens hydrophobic interactions, this result supports the view that the latter does not contribute to the adsorption process of BSA to hydrophilic PAA-brushes under good solvent conditions.

Possible small changes of the BSA protein secondary and ternary structure at elevated pressure [113] that do not affect the adsorption process are not observable by neutron reflectometry.

4.6 Summary

Using neutron reflectometry, SLD profiles of planar PAA brushes at three different grafting densities before and after incubation with BSA proteins were measured. The extracted Gaussian volume fraction profiles are in line with theoretical predictions by Zhulina and Borisov. Differences were found for the detailed stretching of the brush. These might be caused by neglected hydrophobic interactions at the grafting interface in the theoretical approach. A reason for an increased density of the PAA layer near the grafting plane is seen in the screening of the hydrophobic dPS sublayer from the D_2O subphase.

BSA proteins were found to adsorb to the PAA brushes from solution. A linear increase of the BSA protein adsorption capability with increasing grafting density of the planar PAA brushes was extracted from the NR data. Counterion release and protein charge regulations due to reduced local pD values inside the brushes are considered the main driving forces for this adsorption process on the wrong side of the isoelectric point of the brushes.

To evaluate the distribution of BSA within the PAA brush, assumptions on the brush structure had to be made. If the structure of the PAA brush was conserved, the BSA proteins would not penetrate into the brush but were adsorbed at the surface of the brush. For the assumption that the PAA brush is stretched by the adsorption of BSA to approximately twice its original size, a more homogenous distribution of BSA inside the brush was calculated. Due to the lack of contrast it is not possible to directly exclude one of the models, but as dense polymer brushes are known to be protein resistant, adsorption of BSA on top of the PAA brush is favored.

Elevated hydrostatic pressure of 900 bar was found to have no impact on the structure of the PAA brush and its capability to bind BSA proteins.

CHAPTER 5

PDMAEMA brushes - response to temperature and pressure

5.1 Outline of experiments

Six samples of multi stimuli-responsive PDMAEMA polymer brushes with varied grafting density are investigated by neutron reflectivity as a function of temperature and hydrostatic pressure (Table 5.1).

The response of PDMAEMA brushes to temperature is qualitatively known [4]. In this work however, new insights are gained from the analysis of the NR data. Utilizing the novel LC-DFT model, the analysis of the PDMAEMA brush structure is directly connected to intrinsic physical parameters. The response to temperature is described by a thermodynamically consistent phase diagram that includes a definition of the PDMAEMA brush lower critical solution temperature (LCST).

Table 5.1: Sample overview

Sample	σ [nm^{-2}]	T-range [°C]	p [bar]	Instrument
S1	0.2	20 - 50	1	V6
S2	0.2	30 - 60	1	V6
S3	0.2	20 - 40	1; 500; 1000	FIGARO
S4	0.2	20 - 40	1; 1000	FIGARO
S5	0.1	20 - 40	1; 1000	FIGARO
S6	0.3	20 - 40	1; 1000	FIGARO

So far, the response of hydrostatic pressure has been studied solemnly on homogenous polymer networks such as polymer gels. This work expands the knowledge to the inhomogeneous structure of polymer brushes. The response to elevated hydrostatic pressure up to 1000 bar is described by the pressure effect on solvent inaccessible cavities in the brush and thus analyzed independent of the response to temperature.

5.2 Preparation of PDMAEMA brushes

The preparation of the PDMAEMA brushes utilized the LS transfer (Chapter 3.2.3) of free floating dPS-PDMAEMA block copolymer precursor layers with defined grafting densities to dPS pre spincoated Si substrates.

The block copolymer dPS_{32}-$PDMAEMA_{113}$ was dissolved in toluene at a concentration of 1 mg/ml. At first, the samples were prepared with the same process as the PAA brushes (Chapter 4.2) and similarily monitored with X-ray reflectometry (Figure 5.1).

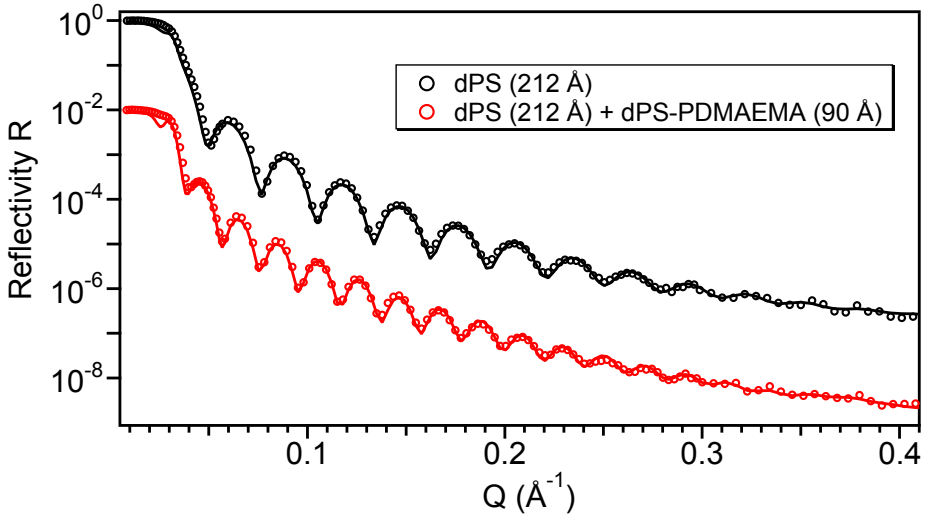

Figure 5.1: Fitted X-ray reflectivity of a dPS spincoated sample before and after LS transfer of the dPS-PDMAEMA block copolymer at a grafting density $\sigma = 0.3\,\mathrm{nm}^{-2}$.

These test samples were prepared before the beamtime and transported in the dried state. First neutron measurements at the EROS reflectometer at LLB showed a response of the rehydrated PDMAEMA brushes to temperature (Figure 5.2) but also revealed a likely mixing or interdiffusion of dPS and PDMAEMA at the grafting interface. The thickness of the spincoated dPS sublayer, as measured with X-ray reflectometry, was 212 Å (Figure 5.1). This thickness was expected to increase by ≈ 14 Å to 226 Å due to the dPS part of the block copolymer. The extracted SLD profiles of the NR measurements (Figure 5.2) revealed a drop of the SLD already at 180 Å instead of the expected 226 Å. Most likely an interdiffusion of dPS and PDMAEMA was caused by the annealing of the sample after the transfer of the

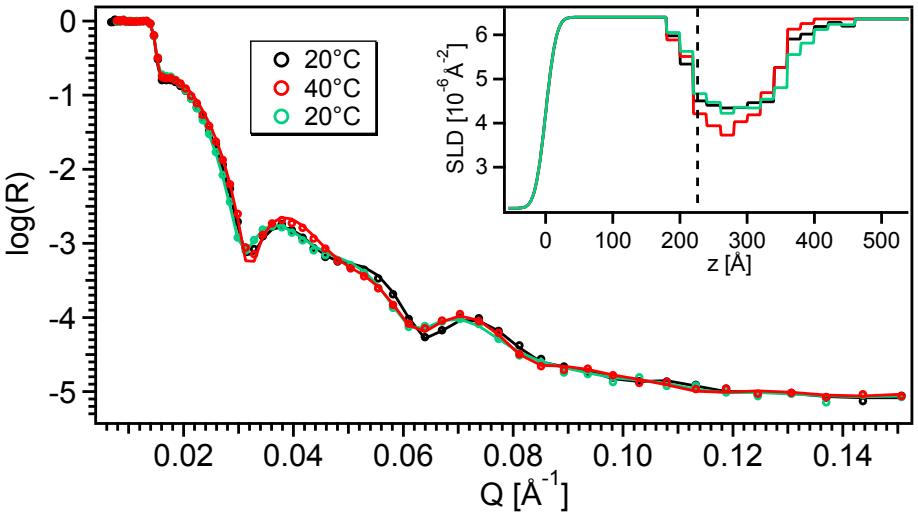

Figure 5.2: NR data for a PDMAEMA brush ($\sigma = 0.3\,\mathrm{nm}^{-2}$) at 20 °C and 40 °C. As expected, the brush responds to increasing temperature with a decrease in brush thickness. But the brush is not fully functional. From prior X-ray reflectivity measurements, a thickness of the dPS sublayer of 226 Å was expected (dashed line), but upon drying and annealing of the sample after the LS transfer, parts of PDMAEMA seemed to diffuse into the dPS sublayer.

dPS-PDMAEMA block copolymer to the dPS spincoated substrate.

To solve the issue of interdiffusion, the annealing and drying after the LS transfer was discarded. This change lead to the following final preparation sequence for the samples S1-S6 (details in Table 5.1): The polymer containing toluene solvent was spread on a clean D_2O surface of $2800\,\mathrm{mm}^2$ by using a Hamilton syringe. The liquid surface area was precisely matching the surface area of the silicon substrates. This way, the grafting density was controlled by the amount of spreading solution, deposited on the water surface. The subphase pD (pD = pH + 0.4 [114]) was adjusted to 9.3 ± 0.3 with a 10 mM borate buffer (H_3BO_3, KCl, NaOD). After minimum 10 min delay time, allowing for solvent evaporation, the resultant dPS-PDMAEMA Langmuir monolayer was transferred from the air-water interface to the dPS pre-coated Si substrate by applying the Langmuir-Schäfer technique (Chapter 3.2.3). The final preparation step was performed near the neutron reflectometer for immediate mounting of the substrates into the NR sample cell. Neither intermediate drying nor annealing was applied and thus contamination and damage of the brush upon drying and

rehydration could be avoided. The results of the NR measurements (Chapter 5.4) showed no stability problems in the solvent swollen state for at least 2 days and temperatures up to 55 °C.

5.3 The LC-DFT model for PDMAEMA brushes

The full theoretical derivation of the LC-DFT model for responsive polymer brushes can be found in Chapter 2.3. The volume fraction profile of a PDMAEMA brush is related to the monomer density via the DMAEMA monomer volume $v_m = 225\,\text{Å}$ [115]. To account for the dPS sublayer with thickness z_0 the volume fraction profiles of the polymer brush are parametrized by $\tilde{z} = z - z_0$. The determining equation 2.20 is transferred into a more adequate form for the fitting process:

$$\varphi(\tilde{z}) = \varphi_0 \exp\left(-\frac{(\tilde{z})^2}{H_0^2}\right) \exp\left(-2\frac{B_2}{v_m}\varphi(\tilde{z}) - \frac{3}{2}\frac{B_3}{{v_m}^2}\varphi(\tilde{z})^2 - 2\frac{1}{\mathrm{k_B}T}P\frac{v_0}{v_m}\varphi(\tilde{z})v_m\right) \tag{5.1}$$

Equation 5.1 has to be solved self-consistently. In this process φ_0 is a normalization factor that is adjusted to the grafting density:

$$\sigma = \frac{1}{N v_m}\int \varphi(\tilde{z})\mathrm{d}\tilde{z} \tag{5.2}$$

Temperature T and pressure P are external experimental parameters. The monomer volume $v_m = 225\,\text{Å}$ is a fixed parameter of polymer. The remaining free parameters of the analytical model of the brush volume fraction $\varphi(\tilde{z})$ are σ, H_0, B_2, B_3 and v_0.

The grafting density σ relates to the mass of the brush and ideally is kept constant for all fits on a given sample. H_0 describes the thickness of the undisturbed ideal Gaussian brush. In a perfect theoretical description this thickness is expected to be globally constant, but the current state of the analytical model does not include all possible interactions. Not explicitly included are electrostatic and osmotic forces, as well as interactions of the polymer brush with the grafting interface. For a consistent determination of the relevant parameters all unknown interactions are absorbed into H_0 upon description of the experimental results. The third virial coefficient B_3 is governed by packing effects and thus was globally set to the value of hard spheres, that is

$$\frac{B_3}{{v_m}^2} = 10 \tag{5.3}$$

The remaining two parameters are related to the response of the inhomogeneous PDMAEMA volume fraction profile to temperature and pressure. The response to temperature depends solely on the value of the second virial coefficient $B_2 \Rightarrow B_2(T)$. The pressure effects are coupled to the value of the solvent inaccessible cavity volume v_0. Thus, temperature and pressure are completely separated.

To include the analytical description in the NR SLD model for polymer brushes in the solvent swollen state (Chapter 3.3.6), the PDMAEMA brush profile has been divided into 120 layers of 5 Å thickness each. The reciprocal width of the chosen slices is larger than 6 times the maximum momentum transfer probed experimentally and ensured avoiding artificial interferences in the calculated reflectivity curves used for fitting. Roughness between the dPS sublayer and the polymer brush is simulated by a Gaussian convolution of SLD(z).

The source code for the calculation of the analytical brush profile and the translation to the layer model is given in Appendix A.4. The reflectivity was fitted in R vs. Q including the resolution ΔQ and a weighting based on the reciprocal statistical error of the reflectivity δR.

5.4 Results

5.4.1 Response to temperature

PDMAEMA polymers in solution undergo a hydrophobic coil to globule transition for increasing temperature around the LCST [53]. The resultant effect on polymer brushes is a decreasing brush thickness [4]. The LCST for polymers in solution is well defined by the onset of the phase separation between polymer and solvent. The latter can be analyzed by turbidity measurements. For polymer brushes a phase separation manifests itself in the structural response of the polymer brush. In their work, Jia et al. confirmed on ATRP grown PDMAEMA brushes that around the the LCST the brush thickness is reduced [4]. In this work, in addition to the phenomenological observation of the polymer brush thickness reduction, the characterization of the response to temperature utilizing the new analytical LC-DFT model allows for a deeper understanding of the process on monomer level.

The response to temperature in a range of 20 to 60 °C was measured by neutron reflectometry on PDMAEMA brushes with a prepared grafting density $\sigma = 0.2\,\mathrm{nm}^{-2}$ (samples S1+S2). The pD of the D_2O sub-phase was chosen to 9.3 ± 0.3 to adjust the LCST to a value around 40 °C [53].

Figure 5.3 shows the NR data from two PDMAEMA brushes (S1 + S2) as a function of sample temperature. The reflectivity changes continuously upon heating in steps of 5 K from 20 °C to 50 °C for sample S1 (top graph) and from 30 °C to 55 °C for sample S2 (middle graph). The changing reflectivity is a consequence of the underlying changes of the brush structure (bottom graph). With increasing temperature up to 40 °C the PDMAEMA brushes show a continuous collapse. They transform from a purely Gaussian volume fraction profile at 20 °C to a state at 40 °C, that shows a parabolic high density profile close to the dPS buoy layer and a low density Gaussian tail close to the D_2O fronting phase. The temperature induced transition is found to be fully reversible (Figure 5.4). For temperatures above 40 °C and thus above the expected LCST, a distinctive vertical phase separation in high and low density phases of the brush occurs. The extracted grafting density for both samples is $\sigma = 0.22 \pm 0.2\,\mathrm{nm}^{-2}$ and thus confirms the successful brush preparation. The brushes were

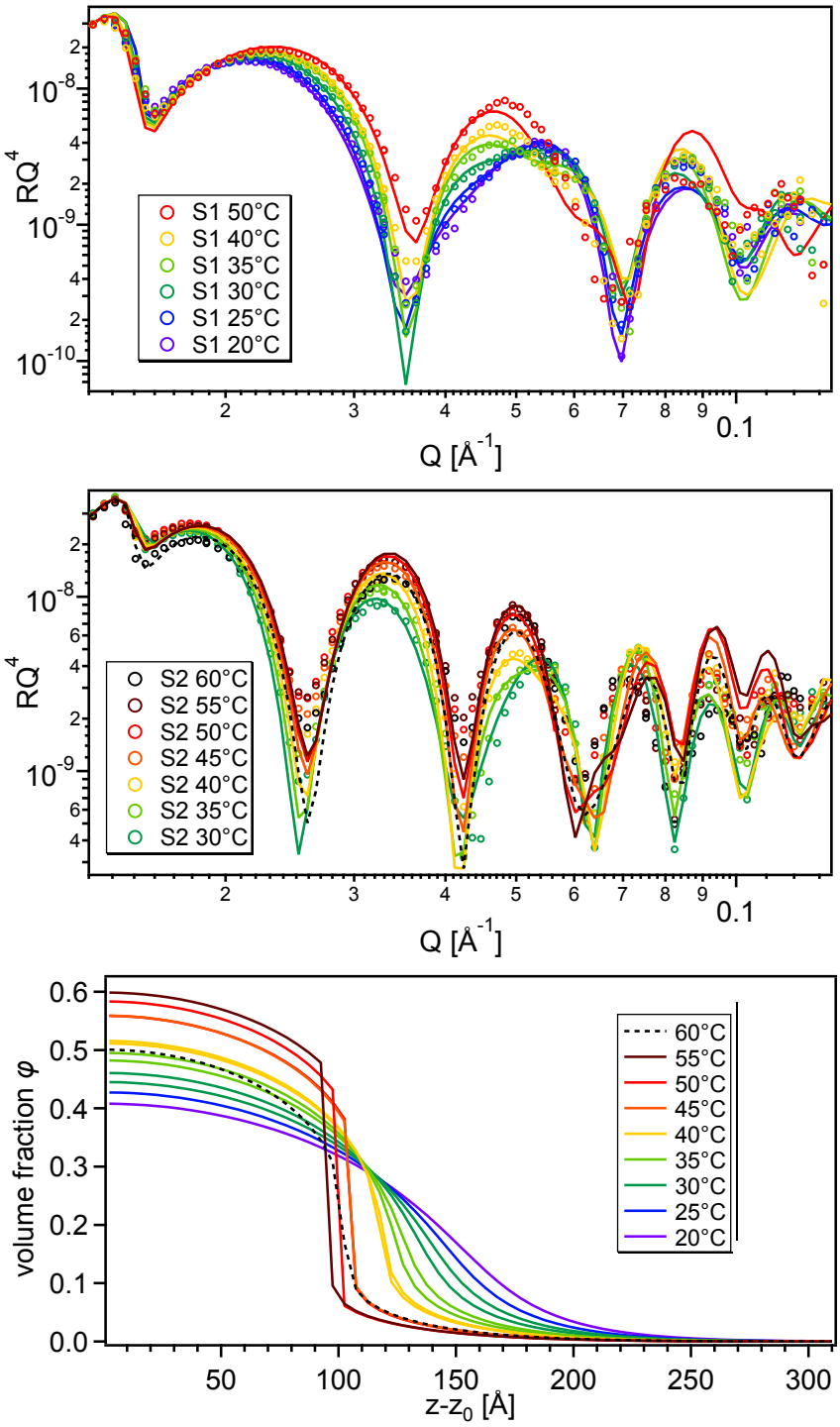

Figure 5.3: Neutron reflectivity from two PDMEAMA brushes (S1:top; S2:middle) grafted to dPS pre-coated silicon support at a graft density of 0.22 nm^{-2} against a D_2O liquid phase at pD 9.3 as a function of sample temperature. The bottom graph displays the extracted volume fraction profiles of the brushes.

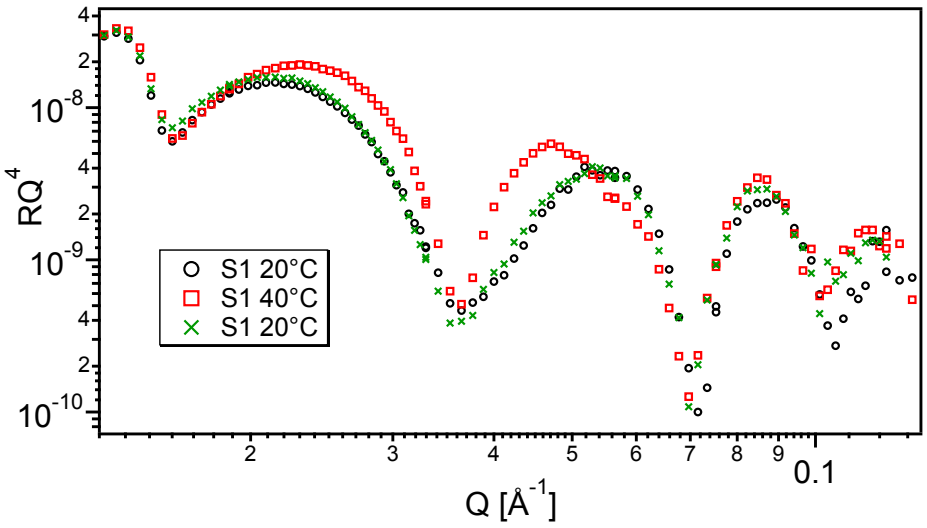

Figure 5.4: Neutron reflectivity from a PDMEAMA brush (S1) grafted to a dPS pre-coated silicon support at a graft density of 0.22 nm^{-2} against a D_2O liquid phase at pD 9.3. The sample was measured first at a temperature of 20 °C, then heated and measured at 40 °C and subsequently cooled back to 20 °C.

stable up to at least 55 °C. At the highest measured temperature of 60 °C (sample S2) the extracted grafting density dropped to $\sigma = 0.19 \pm 0.2\,nm^{-2}$. This implies a loss of $\approx 15\,\%$ of the PDMAEMA brush at highest experimental temperature, which is also visible in the decrease of the brush volume fraction profile (dashed line bottom Figure 5.3).

Taking advantage of the analytical model, a deeper understanding of PDMAEMA brush collapse is gained by the analysis of the extracted brush parameters. The data sets were analyzed as described in Chapter 5.3. The only local fitting parameter changing with temperature is the second virial coefficient $B_2(T)$.

The values for the extracted second virial coefficient $B_2(T)$ are summarized in Table 5.2 and visualized in Figure 5.5. In the temperature region from 20 to 45 °C B_2 scales linearly with T as denoted by the dashed line in Figure 5.5 with a slope of

$$\frac{B_2(T)}{v_m} = 32.7 - 0.12\,T/\mathrm{K} \tag{5.4}$$

Table 5.2: B_2/v_m as a function of sample temperature T for samples S1 and S2

T [°C]	20	25	30	35	40	45	50	55
S1	-2.60 ±0.25	−3.21 ±0.21	−4.09 ±0.16	−4.83 ±0.12	−5.15 ±0.15		−5.88 ±0.15	
S2			−3.70 ±0.22	−4.57 ±0.19	−5.22 ±0.18	−5.84 ±0.23	−6.24 ±0.24	−6.31 ±0.22

Above 45 °C, in the region of the vertical phase separation, the values for the second virial coefficient deviate from the linear behavior.

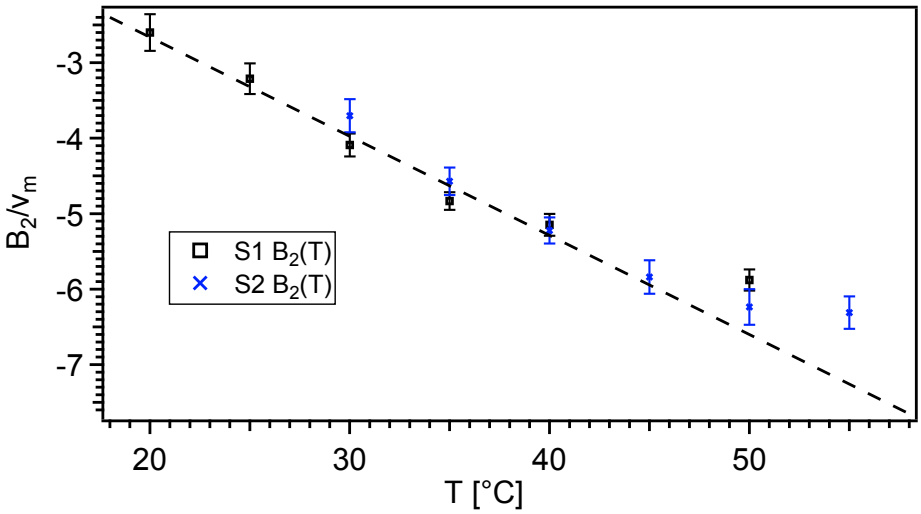

Figure 5.5: Plot of the normalized second virial coefficient, B_2/v_m, of PDMAEMA brushes S1 and S2 of grafting density 0.22 nm^{-2} versus sample temperature T. The dashed line denotes a linear fit to the data between 20 °C and 40 °C with slope $b = -0.12 \pm 0.01\,\mathrm{K}^{-1}$.

Evaluation of fit quality

To evaluate the NR data the Levenberg-Marquardt least square fitting method was performed on χ^2 values, weighted by the inverse statistical error of the reflectivity. This weighting sets the priority of the fit to the lower Q region, where a high reflectivity results in low statistical errors. This region exhibits the most pronounced changes of the reflectivity with temperature and pressure. The minimized χ^2 values of the respective NR data are gathered in Table 5.3. For comparison, Table 5.3 also includes the calculated (not minimized) χ^2 values based on the logarithm of the reflectivity and weighted on the fitted reflectivity.

Table 5.3: χ^2 values for the analytical fit to the neutron reflectivity data. The weighting scheme applied was $w = 1/\delta R$ (error in R). For comparison the χ^2 values were also calculated (not minimized) for the logarithm of the reflectivity ($w = 1$) and for a weighting based on the reciprocal fitted reflectivity ($w = 1/R_{\text{fit}}$).

Sample	T [°C] (P [bar])	χ^2 $w = \frac{1}{\delta R}$	χ^2 of log$R$ $w = 1$	χ^2 $w = \frac{1}{R_{\text{fit}}}$
S1	20	11.2	0.0113	0.106
	25	8.2	0.0083	0.050
	30	8.4	0.0127	0.084
	35	8.5	0.0202	0.161
	40	13.2	0.0383	0.195
	50	31.1	0.0480	0.327
S2	30	13.9	0.0141	0.106
	35	15.4	0.0128	0.118
	40	19.6	0.0203	0.241
	45	32.6	0.0222	0.214
	50	49.9	0.0310	0.254
	55	52.2	0.0407	0.252

The quality of the analytical fits deteriorates with temperature. The fit to the data at 50 °C is a factor of 3 worse than the fit at 20 °C. The latter is a natural outcome of the constraints applied in the course of fitting. Subtle changes in the brush profile cannot be accommodated for in the analytical model. The advantage of the latter is that it describes all observed effects self-consistently in concordance with reasonable physical boundary conditions.

Physical constraints on thickness and SLD of the dPS sublayer and the SLD of the D_2O

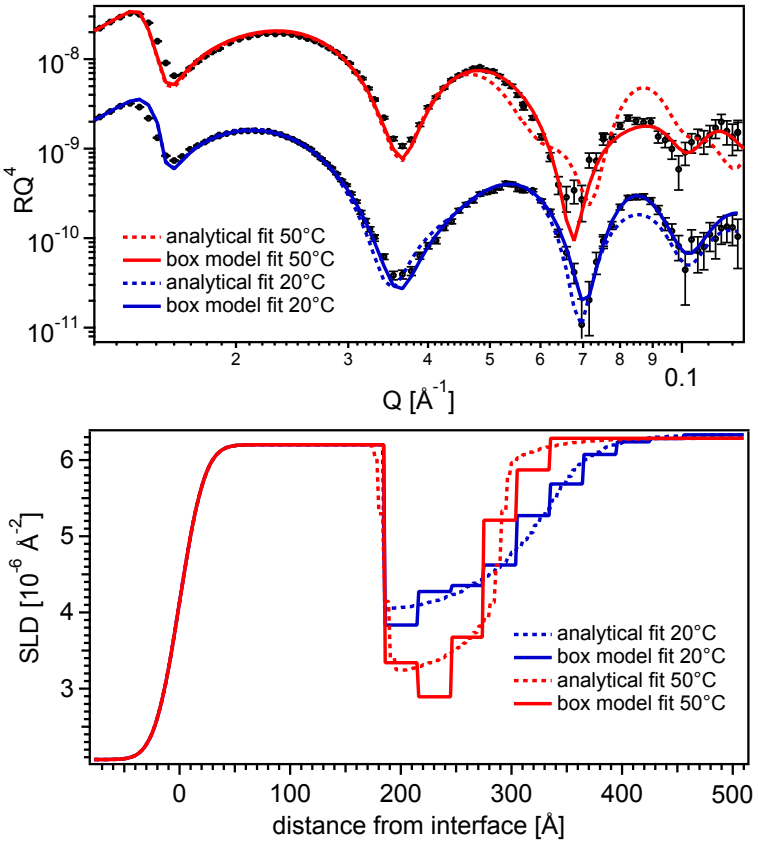

Figure 5.6: Comparison of the box-model with the analytical model fits for sample S1 at temperatures of 20 °C and 50 °C.

solvent when changing temperature or pressure were regarded in all fits. From individual analytical fits on the NR data mean values for the parameters σ, H_0 and v_0 were extracted and globally fixed. In the final fits B_2 was the only remaining fitting parameter. All other parameters, namely dPS thickness, SLD of dPS, D_2O and Si, roughness to silicon, grafting density σ (φ_0), pressure P, temperature T, H_0, v_0, B_3 and the roughness of the brush, through a Gaussian convolution, were globally fixed or set according to physical constraints.

To evaluate the reliability of the analytical profiles, a comparison of the data at 20 and 50 °C with a standard box-model was performed (Figure 5.6). The arbitrary box-model is able to reduce the χ^2 values, when compared to the analytical description, by factors of 3.5 and 2.6, respectively. This is a consequence of the high flexibility to fit the SLD profiles with a larger number of free fitting parameters. Despite the distinct reduction of the χ^2 value,

the extracted SLD profile at 20 °C for the box model is comparable to the analytical result (bottom Figure 5.6). At 50 °C the most prominent difference is a small region of reduced SLD for the second slab of the box model. Both models do show a vertical separation of the brush at 50 °C into an overall high density slab for 185 Å $< z <$ 285 Å and an overall low density slab for $z >$ 285 Å.

A further detailed discussion and direct comparison of both models is given in Chapter 5.5.1.

5.4.2 Response to pressure

The results of the previous chapter showed a response, i.e. a decrease in thickness for PDMAEMA brushes with increasing temperature, due to hydrophobic collapse of the polymer chains. It is known that hydrophobic associated polymers create solvent inaccessible cavities (SIC) [116]. These cavities are influenced by elevated pressure. Hydrostatic pressure forces the water back into the cavity volumes and thus leads to a dissociation of hydrophobic polymer assemblies (Figure 5.7) [26, 29, 56].

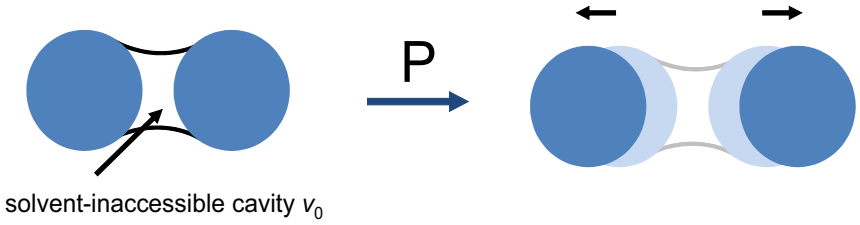

Figure 5.7: Schematic model of the dissociation of assembled monomers of the polymer at elevated hydrostatic pressure which forces solvent into a void volume that was created by hydrophobic interactions.

The reduction of hydrophobicity between monomers then causes a re-swelling of the brush. The LC-DFT model, used for analytical fitting of the NR data, refers to the impact of SIC volumes with the parameter v_0.

Samples S3 and S4 were studied by neutron reflectivity at varied combinations of temperature in the range of 20 to 40 °C and hydrostatic pressure up to 1000 bar. The NR data and fits are shown in Figure 5.8, with the extracted PDMAEMA brush volume fraction profiles in Figure 5.9. As for the samples S1 and S2, the extracted grafting density for S3 and S4 is $\sigma = 0.22 \pm 0.2\,\mathrm{nm}^{-2}$.

At all temperatures the brush volume fraction profiles $\varphi(\tilde{z})$ exhibit a characteristic re-swelling, when the pressure was increased to 1000 bar (Figure 5.9). Within the analytical LC-DFT model pressure induced changes to the PDMAEMA brush volume fraction profiles are described by the pressure effect on the SIC volume v_0. Consistent for all temperatures, the re-swelling of the PDMAEMA polymer brushes of sample S3 and S4 at elevated hydrostatic pressures originates from an extracted SIC volume of $v_0/v_m = 0.2 \pm 0.05$.

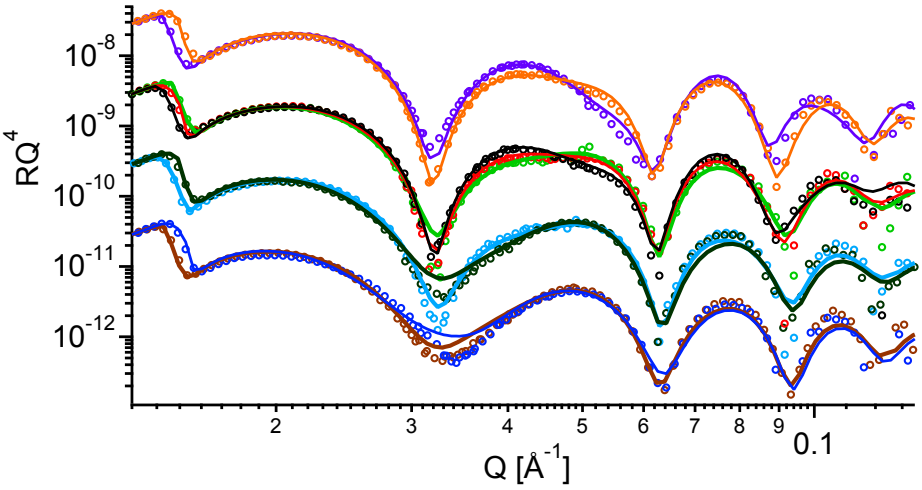

Figure 5.8: NR data and fits showing the response of PDMAEMA brushes to elevated hydrostatic pressure. For better visualization, data from different samples or temperatures were separated by factors of 10 each. From top to bottom the following data are shown: S4 40 °C (1 bar, 1000 bar); S3 40 °C (1 bar, 500 bar, 1000 bar); S3 30 °C (1 bar, 1000 bar) and S3 20 °C (1 bar, 1000 bar). From the pressure induced changes to the PDMAEMA brush a SIC volume $v_0/v_m = 0.20 \pm 0.05$ at constant $B_2(T)$ is extracted. Note that, the compression of the D_2O fronting phase at 1000 bar causes a shift of the total reflection edge.

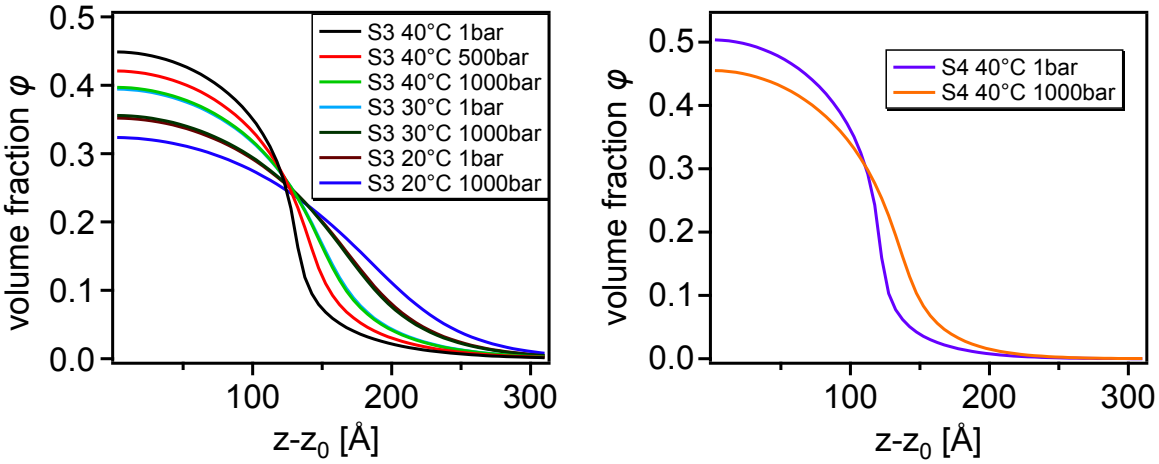

Figure 5.9: Volume fraction profiles $\varphi(\tilde{z})$ extracted from fits of the LC-DFT model to the experimental reflectivities in Figure 5.8. The profiles (left: S3; right: S4) illustrate the re-swelling of the polymer brush when elevated hydrostatic pressure is applied.

Table 5.4: Second virial coefficients $B_2(T)$ for samples S3 and S4 ($\sigma = 0.22\,\mathrm{nm}^{-2}$).

Sample	H_0 [Å]	T [°C]	$B_2(T)/v_m$
S3	150	20	2.7 ± 0.2
		30	3.9 ± 0.2
		40	5.0 ± 0.2
S4	120	40	5.0 ± 0.2

In addition to the pressure effects on the brush structure at 1000 bar the dPS sublayer is compressed by 2 % [95, 96], reducing its thickness and increasing its SLD from $\mathrm{SLD_{dPS}}(1\,\mathrm{bar}) = 6.2 \cdot 10^{-5}\,\mathrm{Å}^{-2*}$ to $\mathrm{SLD_{dPS}}(1000\,\mathrm{bar}) = 6.32 \cdot 10^{-5}\,\mathrm{Å}^{-2}$. The D_2O solvent is also compressed by $\approx 3.6\,\%$, changing its SLD at 20 °C from $\mathrm{SLD_{D2O}}(1\,\mathrm{bar}) = 6.3 \cdot 10^{-5}\,\mathrm{Å}^{-2}$ to $\mathrm{SLD_{D2O}}(1000\,\mathrm{bar}) = 6.53 \cdot 10^{-5}\,\mathrm{Å}^{-2}$ [117, 118]. These changes were taken into account in the respective NR fits at elevated pressure (Figure 5.8).

The extracted values of the second virial coefficient $B_2(T)$ of samples S3 and S4, gathered in Table 5.4, are consistent with the extracted results from samples S1 and S2 (Table 5.2). The only difference for the sample S3 is an increased value $H_0 = 150\,\mathrm{Å}$, needed to fit the data, compared to $H_0 = 120\,\mathrm{Å}$ for samples S1, S2 and S4. At the same temperature the polymer brush on sample S3 is slightly more stretched than to the polymer brushes on samples S1, S2 and S4 (Figure 5.9). The origin of this effect is not known and might be attributed to slightly different experimental conditions during the preparation of the brush.

*The SLD of the dPS sublayer (dPS supplied by Polymer Source) had to be reduced to $6.2 \cdot 10^{-5}\,\mathrm{Å}^{-2}$ from to the theoretical value of $6.4 \cdot 10^{-5}\,\mathrm{Å}^{-2}$ as used in Chapter 4 (dPS supplied by Polymer Standard Service). The difference can be explained by a reduced degree of deuteration.

5.4.3 Varied grafting densities

The results described in Chapter 5.4.1 & 5.4.2 were achieved from samples with a constant grafting density of $\sigma = 0.2\,\mathrm{nm}^{-2}$. By changing the grafting density, it is possible to further tune the properties of the polymer brush. Plamper et al. found a decreasing LCST with increasing branching number of star-shaped PDMAEMA polymers [53]. The branching number of star-shaped polymers can be compared to the grafting density of polymer brushes. To evaluate the effect of confinement at the grafting plane on the response to temperature and pressure, samples S5 and S6 were prepared with a reduced (S5: $\sigma = 0.1\,\mathrm{nm}^{-2}$) and an increased (S6: $\sigma = 0.3\,\mathrm{nm}^{-2}$) grafting density and measured by NR in the following temperature, pressure sequence:

$$[20\,^{\circ}\mathrm{C},\,1\,\mathrm{bar}] \Rightarrow [40\,^{\circ}\mathrm{C},\,1\,\mathrm{bar}] \Rightarrow [40\,^{\circ}\mathrm{C},\,1000\,\mathrm{bar}] \Rightarrow [40\,^{\circ}\mathrm{C},\,1\,\mathrm{bar}] \Rightarrow [20\,^{\circ}\mathrm{C},\,1\,\mathrm{bar}]$$

Figure 5.10 displays NR the data and respective fits for samples S5 and S6. The extracted brush volume fraction profiles are displayed in Figure 5.11. For direct comparison, Figure 5.11 also includes related data for sample S3 with the intermediate grafting density $\sigma = 0.22\,\mathrm{nm}^{-2}$ (the respective NR data for S3 can be found in Figure 5.8). All fits were achieved using the analytical LC-DFT model as described in Chapter 5.3. The extracted parameters for the polymer brush are gathered in Table 5.5.

In concordance with the previous results, increasing temperature causes a fully reversible collapse of the investigated brushes, which is counterbalanced by elevated hydrostatic pressure.

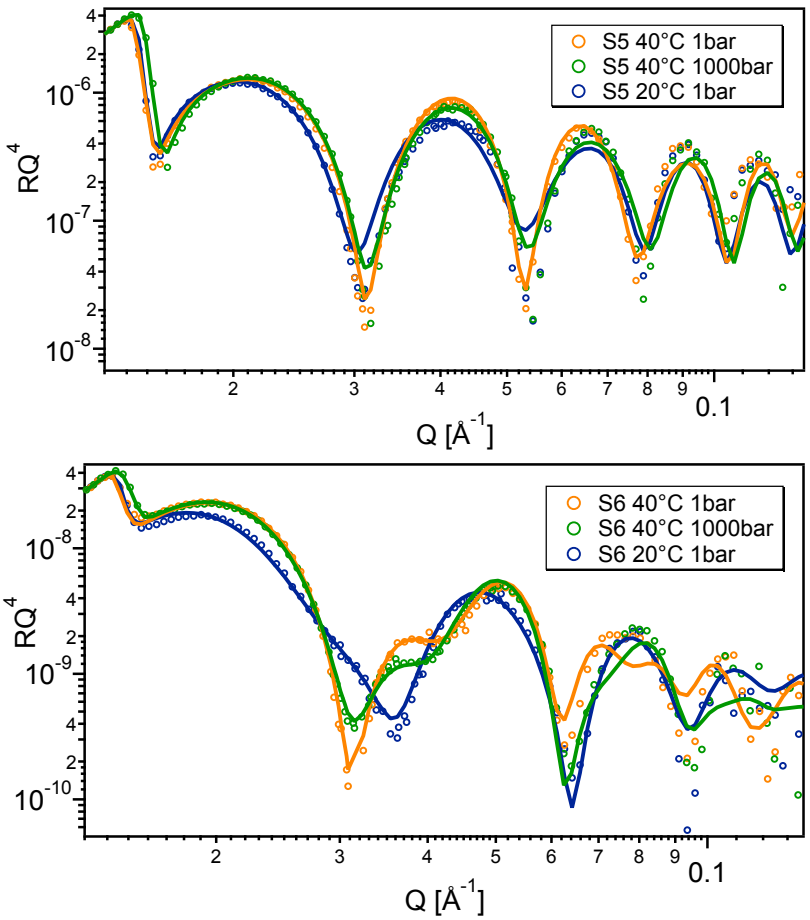

Figure 5.10: NR data and fits for sample S5 (top) and S6 (bottom) at several combinations of temperature and pressure.

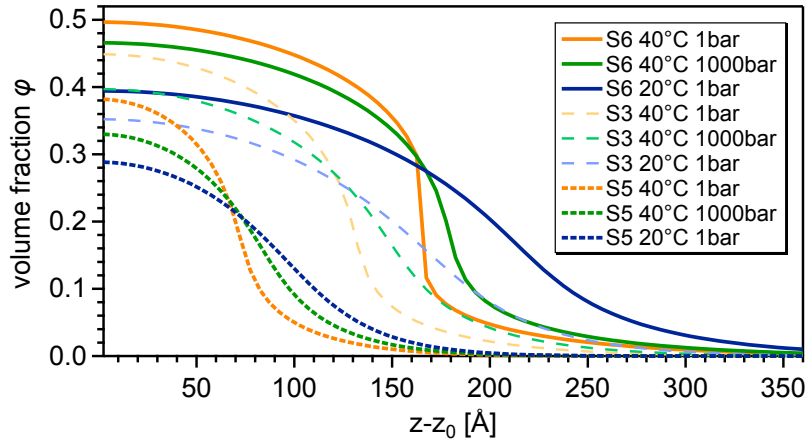

Figure 5.11: Extracted PDMAEMA brush volume fraction profiles for three samples with increasing grafting density ($\sigma(\mathrm{S5}) = 0.11\,\mathrm{nm}^{-2}$; $\sigma(\mathrm{S3}) = 0.22\,\mathrm{nm}^{-2}$; $\sigma(\mathrm{S6}) = 0.32\,\mathrm{nm}^{-2}$).

Table 5.5: Extracted brush parameters for the NR data of samples S3, S5 and S6.

Sample	σ [°C]	T [bar]	P [nm^{-2}]	H_0 [Å]	v_0 [v_m]	B_2 [v_m]	B_3 [v_m^2]
S5	0.11	20	1	100	0.2	-2.5	10
		40	1			-4.8	
		40	1000			-4.8	
S3	0.22	20	1	150	0.2	-2.7	10
		40	1			-5.0	
		40	1000			-5.0	
S6	0.32	20	1	200	0.1	-3.6	10
		40	1			-5.6	
		40	1000			-5.6	

5.5 Discussion

5.5.1 LC-DFT vs. box model

The NR data was analyzed using the novel analytical LC-DFT model and a standard box model. A direct comparison of both models was made for exemplary NR data of sample S1 at 20 °C and 50 °C (Figure 5.6). The extracted volume fraction profiles of both models consistently describe the collapse of the brush from a purely Gaussian profile at 20 °C to a brush structure at 50 °C that exhibits a vertical phase separation into high and low density regions. Concerning the reduction of the χ^2 value, the box model was able to outperform the analytical model by a factor of ≈ 3. The improved quality of the fit is a result of the higher flexibility in the model of the structure of the brush. The box model includes the arbitrary fit of the SLD of up to 9 individual brush layers for each NR measurement. For the analytical model the second virial coefficient B_2 is the only local fit parameter. A handicap of the box-model is the inability to conserve the mass of the brush. This results in extracted grafting densities of $\sigma = 0.21\,\mathrm{nm}^{-2}$ at 20 °C and $\sigma = 0.23\,\mathrm{nm}^{-2}$ at 50 °C. In the analytical model the grafting density is a direct input parameter for the polymer brush profile. Another drawback of the box model is the purely qualitative character of the extracted brush profiles. There is no physical justification for the box-model. The latter is obeyed by the analytical model. The analytical model covers most of the figures of the box-model which describes the interface without any bias. In conclusion, with the effective reduction of the fitting parameters and their physical relevance, the analytical model is considered superior to the box model.

The analytical model allows an examination of the brush properties on a thermodynamically consistent level. The full potential of the theory will be demonstrated and discussed in the following chapters.

5.5.2 Construction of the phase diagram for PDMEAMA brushes

The extracted negative values for $B_2(T)$ are consistent with an attractive hydrophobic interaction between the monomers. These hydrophobic attractions increase with temperature [119] and thus trigger the gradual collapse of the brush. Increasingly negative $B_2(T)$ with increasing T have been observed also for methane molecules in computer simulations and solubility experiments [120, 121]. There, B_2/v_m was found to decrease from about $B_2/v_m = -2$ to -6 in the range from 20 to 80 °C, with the assumed diameter of the methane monomer of $a = 3.5$ Å. Thus, the fitted values of B_2 are very reasonable and support the idea of a hydrophobic collapse of the brush. Within the LC-DFT (Chapter 2.3), the structure of the polymer brush is derived from an ideal undisturbed conformation of the grafted polymer molecules by a virial expansion of the monomer density. The ideal brush is modeled by an ideal gas of monomer segments confined by a harmonic elastic term via equation 2.7. The result is a purely Gaussian density distribution. The real PDMAEMA polymer brush can thus be considered as a van der Waals (vdW) gas of monomer segments, constrained by an external harmonic potential, which expresses the elastic energy of the brush polymers that are fixed to the grafting interface. The equation of state of the monomer vdW gas at density ρ is described by a virial expansion up to third order via

$$\beta P = \rho + B_2(T)\rho^2 + B_3\rho^3 \tag{5.5}$$

where B_2 is essentially linear in temperature T, that is $B_2/v_m(T) = 32.7 - 0.12\,T/\mathrm{K}$ (equation 5.4). By scaling equation 5.5 with the monomer volume v_m it can be rewritten into the dimensionless volume fraction φ

$$\beta P v_m = \varphi + (B_2(T)/v_m)\varphi^2 + (B_3/v_m^2)\varphi^3 \tag{5.6}$$

The critical point of a high(h)-low(l) density coexistence and the full binodal can be calculated by a *Maxwell construction* [122] (Figure 5.12). The constriction on pressures, $P_h = P_l$ and chemical potentials $\mu_h = \mu_l$ in the coexisting states leads to the Maxwell construction for isotherms in the pressure-volume ($P - V$) space, where equality of integrated areas in the non-monotonic part of the isotherms must be established. The spinodal is defined by the

stability limits that identify a diverging compressibility. The latter are given by the minimum and the maximum of the isotherms above the critical point in temperature. For numerical evaluation, equation 5.6 is written in the more appropriate form

$$\tilde{P}(x) = 1/x + (B_2(T)/v_m)/x^2 + (B_3/v_m^2)/x^3 \tag{5.7}$$

where $\tilde{P}(x) = \beta v_m P$ and $x = 1/\varphi \propto V$. An example for isotherms $\tilde{P}(x)$ below (40 °C) and above (50 °C) the critical point, including the Maxwell construction (dashed line) is given in Figure 5.12. The function $\tilde{P}(x)$ was numerically evaluated. $B_3/v_m^2 = 10$ [123] is T-independent. Integrals of $\tilde{P}(x)$ were computed Gaussian quadratures. The minima and maxima of $\tilde{P}(x)$ for every temperature T were evaluated by a Newton-Raphson scheme that identified the roots of $P'(x) = \partial P/\partial x$. The results for the spinodal and binodal are displayed in Figure 5.13.

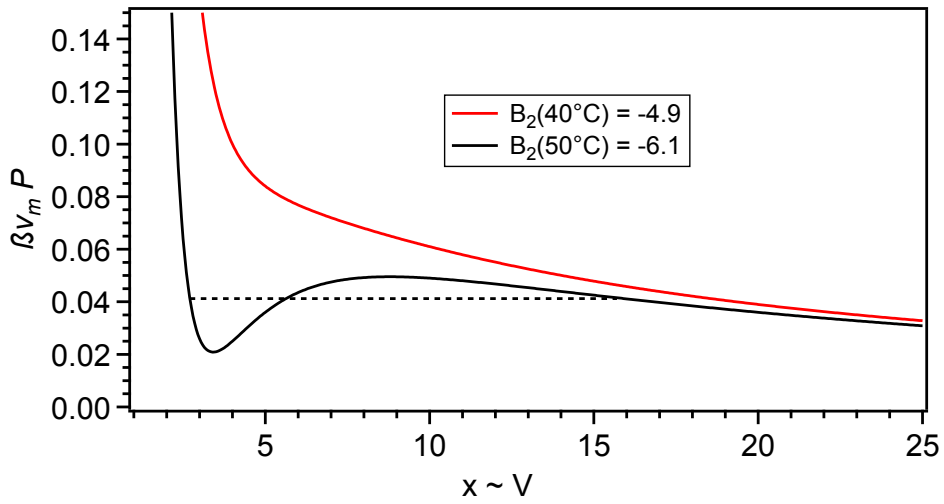

Figure 5.12: Example isotherms $\tilde{P}(x)$ for temperatures below (40 °C) and above (50 °C) the critical point. In the non-monotonic region for the isotherm at 50 °C a Maxwell construction is used to identify the critical points of a high-low density coexistence (binodal).

The vertical phase separation in high and low density phases is quantified by the binodal/spinodal phase diagram in Figure 5.13. The important conclusion from Figure 5.13 is that the critical point is located at a temperature of about 44 °C. This value is consistent with the expected cloud point (LCST) of PDMEAMA polymers at pD 9.3 in solution [53].

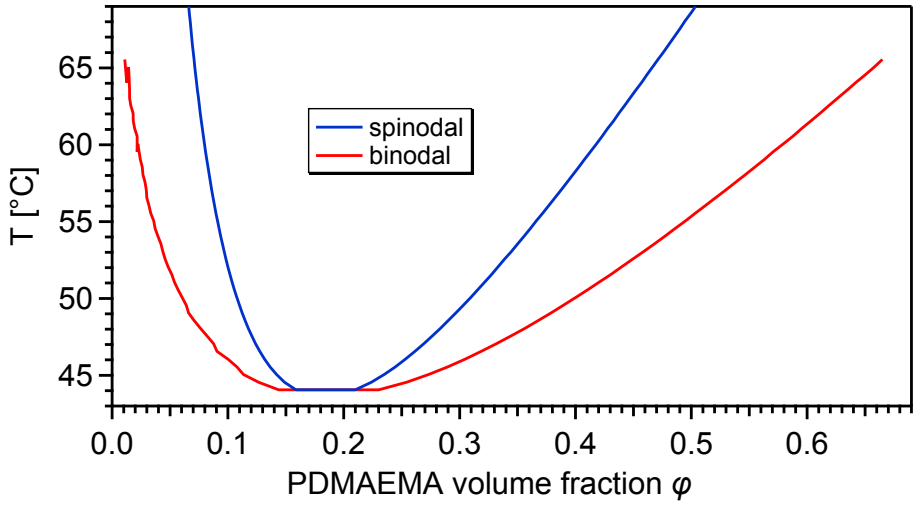

Figure 5.13: Stability line (spinodal) and coexistence line (binodal) of the monomer vdW gas. The critical point (LCST) is at 44 °C.

Thus, in the following the critical point in temperature is used to define the LCST of the PDMAEMA brush. The vertical phase separation for temperatures above the LCST, indicated by a sharp jump in the volume fraction profile, is directly visible in the respective SLD profiles (bottom part of Figure 5.3). The polymer brush exhibits a spatially separated structural high-low density coexistence of collapsed and stretched polymers.

The existence of a spatial separation into high-low density regions above the LCST is predicted theoretically within SCFT [124] and also confirmed experimentally for chemically different ATRP grown systems [125, 126]. For the PDMAEMA brush system investigated here, the resulting LCST is in line with the findings by Jia et al. who identified a phase transition for PDMAEMA brushes between 30 °C and 40 °C at slightly higher pH 10 [4]. Their identification of the phase transition was based purely on the evaluation of fitted box-model SLD profiles. In this work, using a theoretical approach to the analytical fitting of the NR data, the results are in addition thermodynamically consistent. The LCST is obtained from the extracted temperature dependency of $B_2(T)$ and thus directly based on the responsive structure of the polymer brush below the LCST.

Above the LCST high and low phases coexist in the brush in the vertical direction, i.e. as a function of distance from the grafting plane. The theoretical model expects a sharp

transition between the high density and the low density phase. In a real polymer brush local density fluctuations might occur. The latter are not accounted for in the current analytical description of the brush profile and thus the quality of the fits deteriorates for temperatures $> 40\,^{\circ}\mathrm{C}$ (Table 5.3).

Approaching $60\,^{\circ}\mathrm{C}$ in the phase diagram (Figure 5.13), the stable region of low density phase almost vanishes. The structure of the brush is expected to collapse to a condensed homogenous layer. In the experiment this was not observed. The analysis of the NR data at $60\,^{\circ}\mathrm{C}$ showed that the mass of the brush was not constant. Approximately $15\,\%$ of the polymer chains were detached from the interface. The complete collapse of the brush seems to be an unstable state. By the detachment of some of the polymer chains, the brush adopts a more relaxed and stable conformation (dashed black line in the bottom part of Figure 5.3).

5.5.3 Antagonistic effects of temperature and hydrostatic pressure

Just like the second virial coefficient B_2, the hydrostatic pressure P couples linearly to the monomer density via v_0. Thus, directly within the LC-DFT model, hydrostatic pressure exactly counteracts the structural hydrophobic collapse that is caused by increasing temperature. This relation and the linear dependency between temperature and the second virial coefficient $B_2(T)$ below the LCST allows for the calculation of a structural temperature-pressure equilibrium. All structural changes of a PDMAEMA brush for an increase of temperature $\Delta T = 1\,\mathrm{K}$ is directly canceled by increasing pressure by

$$\Delta P/\Delta T = |b| k_B T / v_0 \simeq (110 \pm 10)\,\mathrm{bar/K} \tag{5.8}$$

where $b = -0.12\,\mathrm{K}^{-1}$ is the slope of the linear dependency of $B_2(T)$ (equation 5.4). The $\approx 100\,$bar/K cancellation effect is a direct result of the analytical LC-DFT theory and based on independent measurements of the structural response of the PDMAEMA polymer brush to temperature and pressure.

This effect is directly visible in the experimental NR data, for instance in Figure 5.14. Two pairs of neutron reflectivity data for a PDMAEMA brush (S3) are shown for direct comparison. The first pair was measured at 1 bar, 20 °C (green) and 1000 bar, 30 °C and the second pair at 1 bar, 30 °C (green) and 1000 bar, 40 °C. Except for the position of the total reflection edge, which only reflects the compressibility of the D_2O solvent and a small shift of the reflectivity due to the reduced dPS sublayer thickness, both pairs perfectly match. The structure of the brush did not change when the temperature was increased by 10 K and simultaneously the pressure was raised by 1000 bar. To visualize the impact of non-brush specific pressure effects, namely compressibility of the dPS sublayer and the D_2O solvent, to the reflectivity, Figure 5.14 includes fits of the reflectivity (solid lines) with the respective SLD profiles in Figure 5.15. While the SLD profiles differ due to the compressibility effects of sublayer and sub-phase, the extracted volume fraction profiles of the brush, Figure 5.16, match and directly support the $\approx 100\,$bar/1 K cancellation.

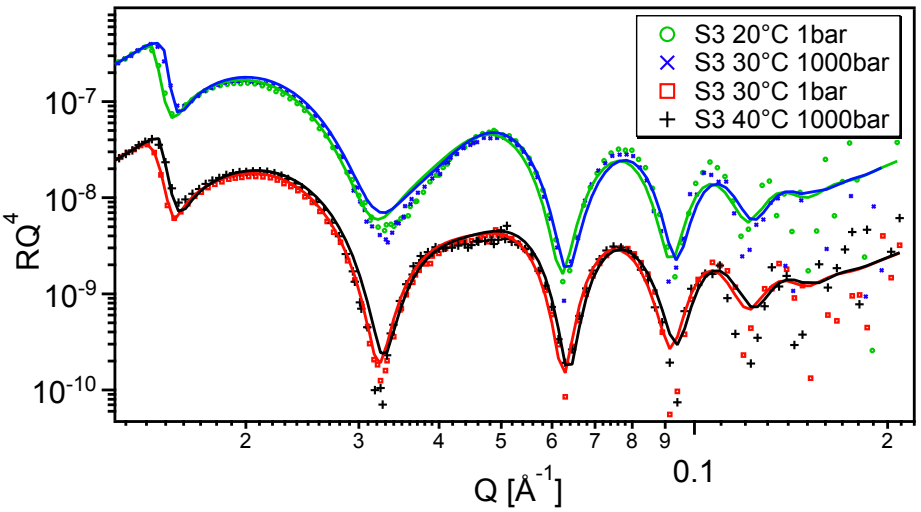

Figure 5.14: Neutron reflectivity data and fits from a PDMEAMA brush (S3) at a grafting density of $\sigma = 0.22\,\mathrm{nm}^{-2}$ as a function of pressure and temperature. Reflectivity data from measurements at 1 bar and temperatures of 20 °C and 30 °C is paired with the respective data at 1000 bar and a simultaneous temperature increase of 10 K.

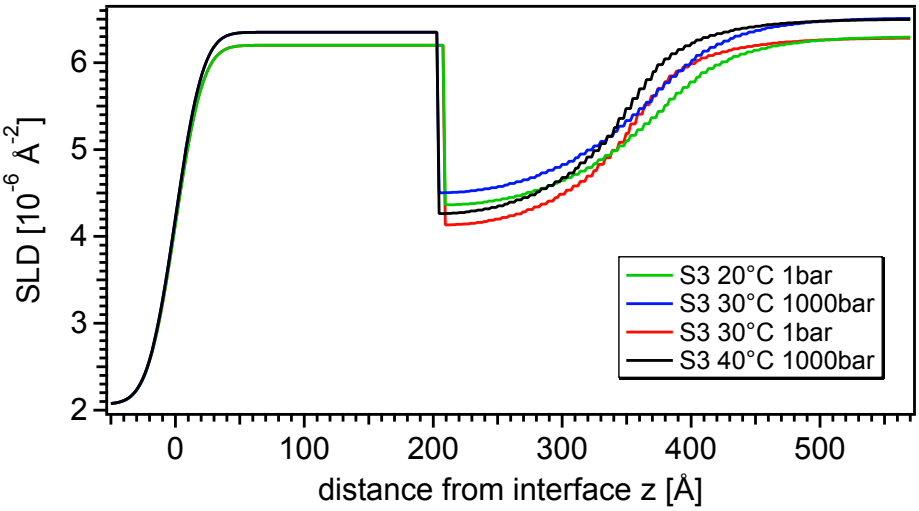

Figure 5.15: Scattering length density profile from the reflectivity fits of Figure 5.14. Differences in the SLD profiles are exclusively caused by the compressibility of D_2O and dPS.

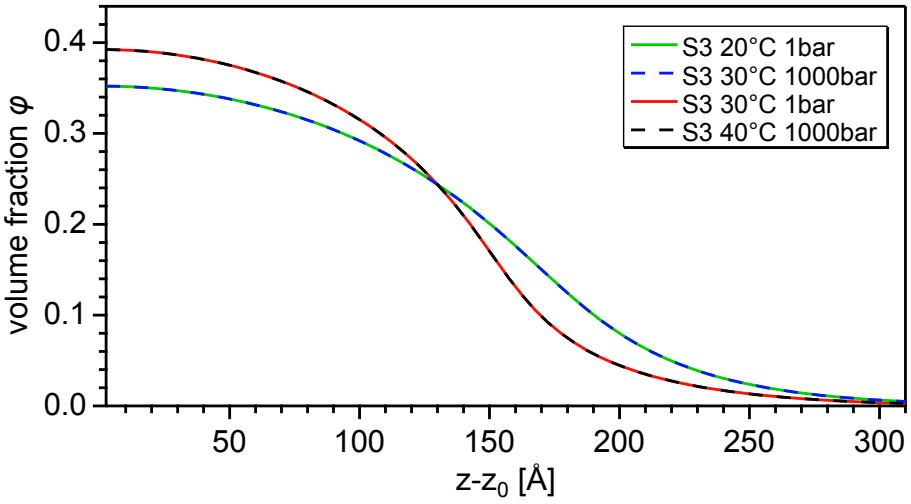

Figure 5.16: Pairwise matching PDMAEMA brush volume fraction profiles that were extracted from the SLD profiles of Figure 5.15.

5.5.4 Confinement effects

Confinement effects were analyzed by comparing the results of the samples S3, S5 and S6. The extracted grafting densities $\sigma = 0.11\,\mathrm{nm}^{-2}$ for S5 and $\sigma = 0.32\,\mathrm{nm}^{-2}$ for S6 confirm the successful preparation and transfer of the brushes. Qualitatively, the volume fraction profiles of S5 and S6 (Figure 5.11) showed the same response to temperature and pressure as the brushes measured at intermediate grafting density $\sigma = 0.22\,\mathrm{nm}^{-2}$ (S1-S4). An increase of temperature from 20 to 40 °C caused a hydrophobic collapse of the brushes that is partly counterbalanced by increasing hydrostatic pressure.

However, small differences in the brush structures due confinement effects are visible and are quantified by the extracted fitting parameters of the analytical LC-DFT model (Table 5.5). With increasing grafting density the thickness H_0 also increases. Theoretically, H_0 is the thickness of the undisturbed ideal brush that is independent of the grafting density. The stretching of a brush with increasing grafting density is accounted for the impact of the third virial coefficient B_3, which includes hard-core packing effects. The latter are not strong enough to completely describe the observed stretching of the brush with increasing grafting density. In our pragmatic approach additional forces on the PDMAEMA brush, that are not explicitly included in the analytical model, are absorbed into H_0. A likely additional contribution which is not covered by the LC-DFT is the electrostatic interaction. The $\mathrm{pK_a}$ of PDMAEMA is 7.5 ± 0.5 and thus at pH = 9.3 approximately 2-3% of the monomers' amine groups are positively charged [53, 127]. For higher grafting densities with an increased packing fraction of charged monomers, electrostatic repulsion might explain the observed increase in H_0.

A small change of the second virial coefficients has been observed as well. With increasing grafting density, $B_2(T)$ consistently shifts to more negative values that result in increasing hydrophobic interactions at comparable temperatures. This indicates a reduction of the LCST for more densely grafted brushes. For sample S6 with the highest grafting density $\sigma = 0.32\,\mathrm{nm}^{-2}$, the volume fraction profile at 40 °C and ambient pressure exhibits the characteristic signature of a vertical phase separation for a brush above the LCST. In this work, the LCST is defined by the critical point of the polymer brush phase diagram, that is the minimum of the binodal and spinodal. The latter is constructed by the minimum and the

maximum of the isotherms above the critical point in temperature. The equation of state for the brush system (equation 5.5) is

$$\beta P = \rho + B_2(T)\rho^2 + B_3\rho^3$$

The minima and maxima are defined by the root of the derivation $\partial/\partial\rho$:

$$0 = \rho^2 + \frac{2B_2}{3B_3}\rho + \frac{1}{3B_3} \tag{5.9}$$

$$\Rightarrow \rho = -\frac{B_2}{3B_3} \pm \sqrt{\frac{{B_2}^2}{9{B_3}^2} - \frac{1}{3B_3}} \tag{5.10}$$

Thus, the critical point is given for

$$\sqrt{\frac{B_2^2}{9B_3^2} - \frac{1}{3B_3}} = 0 \tag{5.11}$$

which leads to the relation between the virial coefficients

$$B_2 = \pm\sqrt{3B_3} \tag{5.12}$$

and a critical density of

$$\rho_c = \frac{1}{\sqrt{3B_3}} \tag{5.13}$$

For ${B_3}/{v_m}^2 = 10$ (equation 5.3), the values at the critical point are

$$\frac{B_2}{v_m} = 5.48 \tag{5.14}$$

$$\frac{\rho_c}{v_m} = \varphi_c = 0.18 \tag{5.15}$$

For $B_2/v_m < 5.48$ the brush is below the LCST and exhibits a continuous density profile. Crossing the critical point at $B_2/v_m > 5.48$, for temperatures above the LCST, the brush vertically separates into a high density region at the grafting plane and a low density region towards the sub-phase. With a value of $B_2/v_m = 5.6$ at 40 °C, the PDMAEMA brush of sample S6 with the highest grafting density $\sigma = 0.32\,\mathrm{nm}^{-2}$ is above the critical point. At the

same temperature of 40 °C, the brushes with a lower grafting density $\sigma = 0.11\,\mathrm{nm}^{-2}$ (S5: $B_2/v_m = 4.8$) and $\sigma = 0.22\,\mathrm{nm}^{-2}$ (S3: $B_2/v_m = 5.0$) are below the critical point (Table 5.5) and thus exhibit a continuous volume fraction profile (Figure 5.11).

From the increase of $B_2(40\,^\circ\mathrm{C})$, with increasing grafting density (Table 5.5), it can be concluded that it is possible to tune the LCST with the density of the grafted polymer chains. In fact, Plamper et al. also observed a reduction of the LCST for PDMAEMA star polymers with increasing branching number or increasing polymer concentration [53]. Conducting titration curve measurements, they determined a decreasing apparent pK_a with increasing branching number. The latter is consistent with findings on other weak polyelectrolytes such as polyacrylic acid [128].
The LCST of PDMAEMA is pH-tunable and the apparent pK_a was found to decrease for increasing PDMAEMA density. Thus, the observed reduction of the LCST for PDMAEMA brushes with increasing grafting density is in accordance with the results on other PDMAEMA structures.

The response to hydrostatic pressure is related to the SIC volume v_0. The pressure induced re-swelling of the polymer brush for sample S5 ($\sigma = 0.11\,\mathrm{nm}^{-2}$) could be modeled with $v_0/v_m = 0.2$, consistent with the results on S3 and S4. For sample S6 ($\sigma = 0.32\,\mathrm{nm}^{-2}$) the SIC volume had to be reduced to $v_0/v_m = 0.1$. For the highest grafting density elevated pressure seems to be less effective. This result can be consistently explained by taking into account that for the brushes of sample S6 the LCST is below 40 °C. The measurements on S1 and S2 revealed a distinctive flattening of the linear dependency of $B_2(T)$ for temperatures above the LCST (Figure 5.5). Hydrostatic pressure counterbalances the response to temperature, described by $B_2(T)$. Thus, above the LCST, the reduction of v_0 in combination with the decreased dependency of $B_2(T)$ for T > LCST can be still consistent with a 100 bar/K cancellation effect.

Temperature and pressure are linearly related to the volume fraction (equation 5.1). The response to pressure can be also seen as a change of an effective B_2. For sample S6 with

$v_0/v_m = 0.1$ an elevated pressure of 1000 bar reduces B_2 by $\Delta B_2/v_m = 0.52$. This leads to an effective value of the second virial coefficient for sample S6 at 40 °C and 1000 bar of $B_2/v_m \approx 5.1$ which is below the value at the the critical point of $B_2/v_m = 5.48$. In conclusion, the results on sample S6 directly demonstrate the possibility to cross the LCST by applying elevated hydrostatic pressure.

5.6 Summary

Planar multi stimuli responsive PDMAEMA brushes from diblock copolymer Langmuir layers with varied grafting density were prepared by Langmuir-Schäfer transfer. Utilizing neutron reflectometry, the samples were analyzed at the solid-liquid interface in a temperature range of 20 to 60 °C for hydrostatic pressures from 1 to 1000 bar. A novel theoretical model of the brush density profile as a function of σ, T and P was used to fit the experimental NR data. Within this model, temperature and pressure effects are described independently. Increasing temperature caused a continuous decrease of polymer brush thickness. The reason for this response of the brush is a hydrophobic coil to globule transition of the polymer chains. When crossing the LCST the brushes collapsed into a high density polymer layer near the grafting plane and a low density Gaussian tail towards the liquid fronting phase. The new model intrinsically includes the observed vertical phase separation and yields the correct position of the LCST in a thermodynamically consistent way, exclusively based on structural data. Hydrostatic pressure was found to act perfectly antagonistic to temperature. The hydrophobic collapse of the PDMAEMA brush that is caused by a temperature increase of 10 K is exactly counterbalanced by a pressure increase of 1000 bar. While the value of the LCST of the polymer brush is found to decrease with the grafting density, the antagonistic effect of hydrostatic pressure is not affected.

APPENDIX A

Appendix

A.1 Abbreviations

AMOR	time-of-flight neutron reflectometer at PSI
ATRP	atom transfer radical polymerization
BSA	bovine serum albumin
dPS	perdeuterated polystyrene
EROS	time-of-flight neutron reflectometer at LLB
FIGARO	time-of-flight neutron reflectometer at ILL
HZB	Helmholtz-Zentrum Berlin
IEP	isoelectric point
ILL	Institute Laue-Langevin
LC-DFT	local cavity density functional theory (Chapter 2.3)
LCST	lower critical solution temperature
LEA	local electroneutrality approximation
LLB	Laboratoire Leon Brillouin
LS	Langmuir-Schäfer
MES	buffering agent 2-(N-morpholino)ethanesulfonic acid
NR	neutron reflectometry
PAA	polyacrylic acid
PDI	polydispersity index
PDMAEMA	poly(N,N-dimethylaminoethyl methacrylate)
PS	polystyrene
PSI	Paul Scherrer Institut

PE	polyelectrolyte
SCF	self-consistent field
SIC	solvent inaccessible cavities
SLD	scattering length density
SPB	spherical polyelectrolyte brush
TOF	time-of-flight
V6	monochromatic neutron reflectometer at HZB

A.2 Variable declarations

Å	length unit [10^{-10} m]
a	effective monomer diameter
B_2	2nd virial coefficient
B_3	3rd virial coefficient
$c_m(z)$	brush monomer density profile
d	layer thickness
d_p	averaged grafted polymer-polymer distance
H_0	ideal brush thickness
H	(brush) height / thickness
$\mathrm{M_W}$	weight-average molar mass
N	degree of polymerization
P	hydrostatic pressure
pH	$-\log_{10}(\mathrm{c_{H^+}})$ hydrogen ion concentration
pD	$-\log_{10}(\mathrm{c_{D^+}})$ deuterium ion concentration
Q	scattering vector / scattering momentum transfer
R_F	averaged end-to-end distance of random coiled polymers
$R(Q)$	(specular) reflectivity
s	grafting area per polymer chain
SLD(z)	scattering length density profile
T	temperature
v_0	monomer-monomer solvent-inaccessible cavity volume
v_m	monomer volume
z_0	thickness of the dPS sublayer
$\tilde{z}$	$= z - z_0$

$\alpha(z)$	relative monomer charge profile
β	$= \frac{1}{k_B T}$ energy normalization factor
Γ	adsorbed mass of BSA per surface area
θ	scattering angle
κ	bound BSA proteins per grafted PAA monomer
λ	wavelength
ω	Gaussian brush thickness
Σ	interface roughness
σ	grafting density
φ_0	polymer brush volume fraction at the grafting plane
$\varphi(z)$	volume packing fraction profile
$\rho(z)$	mass density profile

A.3 Reflectometry instrumental setup

A.3.1 X-ray reflectometry

The X-ray reflectometer used for characterization of substrates and transferred brushes in dry state was a home build instrument with horizontal $\theta - 2\theta$ geometry and a resolution $\Delta Q = 0.003\,\text{Å}^{-1}$ at a wavelength of 1.541 Å generated by a Cu anode. The geometry of the beam was defined by a (0.004 x 8.000) mm slit in front of the sample, followed by a (2 x 10) mm slit after the sample position [129].
At the data reduction, the X-ray raw data was footprint corrected and normalized to the intensity of the direct beam [130].

A.3.2 Neutron reflectometry

A.3.2.1 AMOR

AMOR is a horizontal time-of-flight reflectometer at SINQ/PSI (Villigen, Switzerland) [90]. A full reflectivity run consisted of measurements at incident angles $\theta_1 = 0.4\,^\circ$; $\theta_2 = 0.8\,^\circ$ and $\theta_3 = 1.6\,^\circ$ of the white beam on the samples planar solid-liquid interface through the silicon backing. Those measurements covered a Q-range of 0.008 to $0.174\,\text{Å}^{-1}$, consuming 7 h of beam-time with a resolution $\Delta Q/Q = 7\%$ as defined by chopper system and slits.

Data reduction

For evaluation of the measured neutron reflectivity, the raw data was at first normalized to the measured incident intensity spectra I_0 through the Si wafer at $\theta = 0\,^\circ$. Due to problems in precisely positioning the neutron diaphragms on the incident side we found this simple normalization not exact. The region of total reflection was higher than unity and not constant. There was also a shift of the total reflection edge to lower Q_z values than expected for a measurement against a liquid D_2O fronting with an SLD of $\rho_{D_2O} = 6.36 \cdot 10^{-6}\,\text{Å}^{-2}$. For compensating the experimental deficiencies, the raw data was renormalized as followed: The reflectivity for total reflection near the total reflection edge was normalized to 1. For all spectra measured at $\theta_1 = 0.4\,^\circ$ the normalization of the raw data was applied with an individual

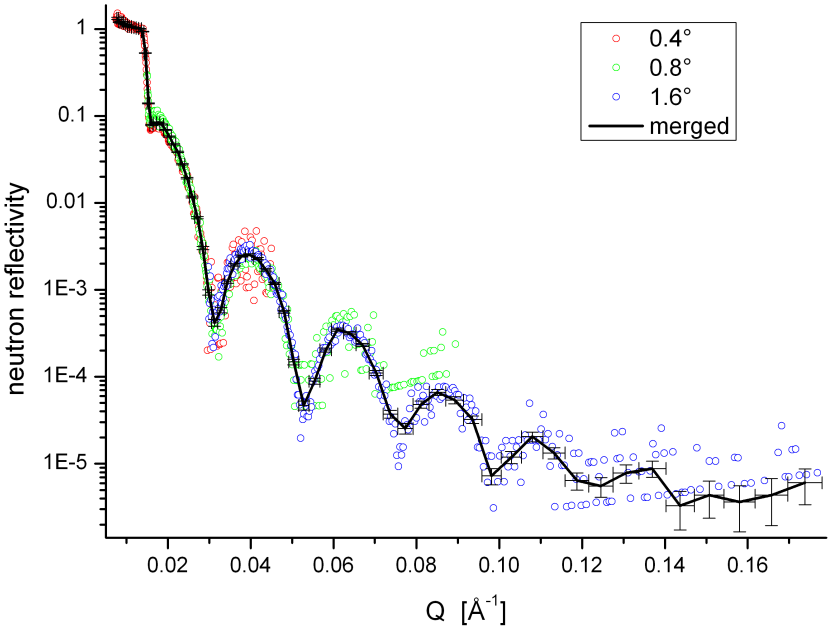

Figure A.1: Normalized raw data

shift $\Delta\theta_1$ to match the theoretical value of the total reflection edge for a measurement against D_2O. The respective spectra measured at $\theta_2 = 0.8^\circ$ and $\theta_3 = 1.6^\circ$ were also normalized with shifts $\Delta\theta_2$, $\Delta\theta_3$ and respective intensity scale factors to best possible overlap in reflectivity. Averaged global shifts $\Delta\bar{\theta}_1 = 0.012 \pm 0.002$; $\Delta\bar{\theta}_2 = 0.018 \pm 0.003$ and $\Delta\bar{\theta}_3 = 0.025 \pm 0.004$ were calculated and applied to normalize all spectra. Finally minor intensity adjustments were made to optimize the overlap of the three different spectra. An example of a renormalized spectrum is shown in A.1. To fit the reflectivity, the three parts were merged using a grid with $\Delta Q/Q = 5\,\%$.

Error estimation

The resulting SLD profiles from the fitted X-ray and neutron reflectivity measurements are afflicted by systematical errors concerning the renormalization of the data and statistical errors from the fitting process including the resolution of the instrument. The statistical error for a single fit derived within Motofit for all measurements was $\Delta\rho(z)_{\text{fit}} \leq \pm 0.2 \cdot 10^{-6}\,\text{Å}^{-2}$. To examine the error of the normalization process in case of neutron reflectivity, the raw

data measured at 0.8 ° incidence was shifted by ±10 % in intensity. Subsequently applied fitting revealed variations in the SLD profiles of $\Delta\rho(z)_{\text{norm}} \leq \pm 0.1 \cdot 10^{-6}\,\text{Å}^{-2}$. Identical uncertainties were found for the small applied shifts in θ that were required for the systematical error in sample alignment. Finally all errors sum up to a maximum error of $\Delta\rho(z) \leq \pm 0.4 \cdot 10^{-6}\,\text{Å}^{-2}$. For SLD's in the range of 4 to $6.57 \cdot 10^{-6}\,\text{Å}^{-2}$ the relative error of the extracted values is less than 10 %.

A.3.2.2 V6

V6 is a horizontal monochromatic reflectometer V6 at HZB (Helmholtz-Zentrum Berlin, Germany) [85]. The wavelength resolution as defined by a pyrolithic graphite monochromator is $\Delta\lambda/\lambda = 2\,\%$. The incident neutron beam with $\lambda = 4.66\,\text{Å}$ was collimated by two rectangular diaphragms achieving a constant resolution ΔQ of $0.001\,\text{Å}^{-1}$ in the range of $0.005 < Q < 0.06\,\text{Å}^{-1}$ and $0.002\,\text{Å}^{-1}$ in the range $0.06 < Q < 0.14\,\text{Å}^{-1}$. Those measurements covered a Q-range of 0.005 to $0.146\,\text{Å}^{-1}$, consuming 7 h of beam-time.
All V6 raw data were footprint corrected and normalized to time and incident beam intensity [130].

A.3.2.3 FIGARO

FIGARO is a horizontal time-of-flight reflectometer at ILL (Institute Laue-Langevin, Grenoble, France). The reflectivity, measured with a white beam of wavelengths 2-20 Å at fixed incident angles 0.824 ° and 2.2 °, respectively, covered a momentum transfer range of $0.01 < Q < 0.2\,\text{Å}^{-1}$.The resolution $\Delta Q/Q$, defined by chopper settings and slits, was in the range of 5 - 6 %. Due to the higher neutron flux at ILL, one measurement in a Q-range of 0.01 to $0.21\,\text{Å}^{-1}$ consumed only 2.5 h of beam time.
For conversion and reduction of the FIGARO time of flight data into $R(Q)$ data sets the COSMOS tool of the ILL data reduction software LAMP was used [131].

A.4 Source code for analytical fitting within Motofit

```
#pragma rtGlobals=1      // Use global access method.
#include "MOTOFIT_all_at_once"

Function LC-DFT_brush_conv_dq(coefs,rr,qq,dq):fitfunc
    wave coefs,rr,qq,dq

    //parameters that describe the physical system
    //coefs[0] = maximum brush length
    //coefs[1] = box thickness
    //coefs[2] = SLD solvent
    //coefs[3] = background
    //coefs[4] = thickness sublayer
    //coefs[5] = SLD sublayer
    //coefs[6] = roughness to silicon
    //coefs[7] = H0 [A]
    //coefs[8] = grafting density [1/nm^2] <= normalization
    //coefs[9] = V0 [A^3]
    //coefs[10] = P [bar]
    //coefs[11] = T [degree C]
    //coefs[12] = monomer length [A]
    //coefs[13] = B2 [A^3]
    //coefs[14] = B3 [A^6]
    //coefs[15] = convolution roughness

    //first these parameters have to be translated to a layer
        model that can be used to calculate reflectivity

    virialbrush_conv_dqtoRef(coefs)          //function for
       parameter conversion
    Wave W_forReflectivity                   //parameters for
       layer model
    Motofit_smeared(W_forreflectivity,RR,qq,dq) //calculation
        of the reflectivity

End
```

```
Function LC-DFT_brush_conv_dqtoRef(coefs)        //converts
    the analytical description parameters into box-model
    parameters that can be used to calculate the reflectivity
    Wave coefs

    variable int_conv_layer = round(abs(coefs[15])*5/coefs
        [1])  //needed for convolution of the sublayer-brush
        interface
    variable boxlayers = coefs[0]/coefs[1] + int_conv_layer
          //number of layers to model the brush

    make/o/d/n=(boxlayers*4+10) W_forReflectivity
        //initialize layer model parameter wave

    //set first parameters
    W_forReflectivity[0] = boxlayers+1       //number of
        layers
    W_forreflectivity[1] = 1              //normalization
    W_forreflectivity[2] = 2.07           //SLD top (Si)
    W_forreflectivity[3] = coefs[2]           //SLD bottom (
        subphase)
    W_forreflectivity[4] = coefs[3]           //background
    W_forreflectivity[5] = 0              //roughness to
        subphase

    //dPS layer (without convoluted area)
    W_forreflectivity[6] = coefs[4] - int_conv_layer*coefs[1]
    W_forreflectivity[7] = coefs[5]
    W_forreflectivity[8] = 0
    W_forreflectivity[9] = coefs[6]

    variable k=10
    variable i=0
    variable j=0
    variable initgd=0


//calculations of the analytical volume fraction profile
    according to the fit parameters
//as there is no explicit function for the profile, it has to
    be solved self-consistently
```

```
//that includes finding the root for a given phi0 and
   subsequent normalization to the grafting density
//=> solve the implicit equation self-consistently

    make/o/d/n=(boxlayers) phiy, phiz
    make/o/d/n=9 rootcoefs

    rootcoefs[1]=coefs[7]    //H0
    rootcoefs[2]=0.5     //gd => phi0
    rootcoefs[3]=coefs[9]    //v0
    rootcoefs[4]=coefs[10]   //P
    rootcoefs[5]=coefs[11]   //T
    rootcoefs[6]=coefs[12]   //vm
    rootcoefs[7]=coefs[13]   //B2
    rootcoefs[8]=coefs[14]   //B3

    for(i=0;i<boxlayers;i=i+1)
        phiz[i] = i*coefs[1] + coefs[1]/2
    endfor

//self consistent iteration to find the right phi0
    do
        if (j>100)       //breakpoint for max iterations steps
            print "break "
            print initgd
            break
        endif

        j+=1

        initgd=0

        for(i=0;i<boxlayers;i=i+1)
            rootcoefs[0]=phiz[i]
            FindRoots /L=0 /H=1 /Q phiroot, rootcoefs
            phiy[i] = V_Root
            initgd += phiy[i]*coefs[1]/(coefs[12]*113)*100
        endfor

        //normalization with desired grafting density
```

```
        //for better conversion, the new phi0 for the next
           iteration
        //is the mean value of the old phi0 value and the
           normalized value
        rootcoefs[2] *= 2*coefs[8]/(initgd+coefs[8])

    while (abs(initgd-coefs[8])>0.0001)

//final normalization
    phiy *= (coefs[8]/initgd)

//define gaussian function for convolution
    killwaves convgauss
    make/o/d/n=(2*int_conv_layer+1) convgauss
    i=0

    convgauss=0

    if(abs(coefs[15])>0)
        for(i=0;i<int_conv_layer+2;i+=1)
            convgauss[i] = 1/(SQRT(2*PI)*abs(coefs[15])) *
               exp( -( (int_conv_layer-i) *coefs[1])^2/ (2*
               abs(coefs[15])^2) )
            convgauss[2*int_conv_layer-i] = 1/(SQRT(2*PI)*abs
               (coefs[15])) * exp( -( (int_conv_layer-i) *
               coefs[1])^2/ (2*abs(coefs[15])^2) )
        endfor
    else
        convgauss[0]=1
    endif
    variable normalize = sum(convgauss)
    convgauss/=normalize

//calculation of convoluted brush profile (convphiy)
    make/o/d/n=(boxlayers) convphiy
    i=0
    k=0
    convphiy = 0

    for(i=0;i<boxlayers;i+=1)
        for(k=0;k<2*int_conv_layer+1;k+=1)
```

```
            if ((i+k+1)>2*int_conv_layer)
                convphiy[i] += phiy[i-2*int_conv_layer+k]*
                   convgauss[k]
            endif
        endfor
    endfor

//reflectivity model parameters for convoluted part of
   sublayer
    for(k=10;k<(10+4*int_conv_layer);k=k+4)
        W_forreflectivity[k] = coefs[1]
        W_forreflectivity[k+1] = (1-convphiy[(k-10)/4])*coefs
           [5]+(convphiy[(k-10)/4])*0.8
        W_forreflectivity[k+2] = 0
        W_forreflectivity[k+3] = 0
    endfor

//reflectivity model parameters for the brush
    for(k=(10+4*int_conv_layer);k<((boxlayers*4)+10);k=k+4)
        W_forreflectivity[k] = coefs[1]
        W_forreflectivity[k+1] = 0.8
        W_forreflectivity[k+2] = (1-convphiy[(k-10)/4])*100
        W_forreflectivity[k+3] = 0
    endfor

End



function phiroot(rootcoefs,phi)

//rootcoefs[0] = z
//rootcoefs[1]=coefs[7] //H0
//rootcoefs[2]=0.5 //gd => phi0
//rootcoefs[3]=coefs[9] //v0
//rootcoefs[4]=coefs[10] //P
//rootcoefs[5]=coefs[11] //T
//rootcoefs[6]=coefs[12] //vm
//rootcoefs[7]=coefs[13] //B2
//rootcoefs[8]=coefs[14] //B3
```

```
wave rootcoefs
variable phi

//analytical description:
variable b = 1/( (rootcoefs[5]+273.15) * 1.3806503*10^-3 )
variable x = 2*rootcoefs[7] + 2*b*rootcoefs[4]*rootcoefs[3]*
   rootcoefs[6]*10^(-5)

return phi - rootcoefs[2]*exp( -(rootcoefs[0]^2) / rootcoefs
   [1]^2 )*exp(-x*phi - 3/2*rootcoefs[8]*phi^2)

End
```

Bibliography

[1] S. T. Milner. “Polymer Brushes”. In: *Science* 251.4996 (1991), pp. 905–914. DOI: 10.1126/science.251.4996.905 (cit. on pp. 1, 8).

[2] Jürgen Rühe et al. “Polyelectrolyte Brushes”. In: *Polyelectrolytes with Defined Molecular Architecture I*. Ed. by Manfred Schmidt. Vol. 165. Advances in Polymer Science. Springer Berlin Heidelberg, 2004, pp. 79–150. ISBN: 978-3-540-00528-5. DOI: 10.1007/b11268 (cit. on pp. 1, 8).

[3] H. Yim et al. “Temperature-Dependent Conformational Change of PNIPAM Grafted Chains at High Surface Density in Water”. In: *Macromolecules* 37.5 (2004), pp. 1994–1997. DOI: 10.1021/ma0354290 (cit. on p. 1).

[4] Haidong Jia, Andrew Wildes, and Simon Titmuss. “Structure of pH-Responsive Polymer Brushes Grown at the Gold-Water Interface: Dependence on Grafting Density and Temperature”. In: *Macromolecules* 45.1 (2012), pp. 305–312. DOI: 10.1021/ma201839y (cit. on pp. 1, 3, 67, 74, 90).

[5] S. Sanjuan et al. “Synthesis and Swelling Behavior of pH-Responsive Polybase Brushes”. In: *Langmuir* 23.10 (2007), pp. 5769–5778. DOI: 10.1021/la063450z (cit. on p. 1).

[6] Dennis Aulich et al. “In Situ Studies on the Switching Behavior of Ultrathin Poly(acrylic acid) Polyelectrolyte Brushes in Different Aqueous Environments”. In: *Langmuir* 26.15 (2010), pp. 12926–12932. DOI: 10.1021/la101762f (cit. on p. 1).

[7] Heiko Ahrens, Stephan Förster, and Christiane A. Helm. “Charged Polymer Brushes: Counterion Incorporation and Scaling Relations”. In: *Phys. Rev. Lett.* 81 (19 Nov. 1998), pp. 4172–4175. DOI: 10.1103/PhysRevLett.81.4172 (cit. on p. 1).

[8] M. Biesalski, D. Johannsmann, and J. Rühe. “Synthesis and swelling behavior of a weak polyacid brush”. In: *The Journal of Chemical Physics* 117.10 (2002), pp. 4988–4994. DOI: 10.1063/1.1490924 (cit. on p. 1).

[9] Sergiy Minko. “Responsive Polymer Brushes”. In: *Journal of Macromolecular Science, Part C: Polymer Reviews* 46.4 (2006), pp. 397–420. DOI: 10.1080/15583720600945402 (cit. on pp. 1, 8, 9).

[10] Nikolay Houbenov, Sergiy Minko, and Manfred Stamm. “Mixed Polyelectrolyte Brush from Oppositely Charged Polymers for Switching of Surface Charge and Composition in Aqueous Environment”. In: *Macromolecules* 36.16 (2003), pp. 5897–5901. DOI: 10.1021/ma0341869 (cit. on p. 1).

[11] Feng Zhou and Wilhelm T. S. Huck. “Three-stage switching of surface wetting using phosphate-bearing polymer brushes”. In: *Chem. Commun.* (48 2005), pp. 5999–6001. DOI: 10.1039/B512106J (cit. on p. 1).

[12] C. Czeslik et al. “Salt-induced protein resistance of polyelectrolyte brushes studied using fluorescence correlation spectroscopy and neutron reflectometry”. In: *Phys. Chem. Chem. Phys.* 6 (24 2004), pp. 5557–5563. DOI: 10.1039/B410805A (cit. on p. 1).

[13] Parul Jain, Gregory L. Baker, and Merlin L. Bruening. "Applications of Polymer Brushes in Protein Analysis and Purification". In: *Annual Review of Analytical Chemistry* 2.1 (2009). PMID: 20636068, pp. 387–408. DOI: 10.1146/annurev-anchem-060908-155153 (cit. on p. 1).

[14] A. Wittemann, B. Haupt, and M. Ballauff. "Controlled Release of Proteins Bound to Spherical Polyelectrolyte Brushes". In: *Zeitschrift für Physikalische Chemie* 221.1 (Jan. 2007), pp. 113–126. ISSN: 0942-9352. DOI: 10.1524/zpch.2007.221.1.113 (cit. on pp. 1–3).

[15] K Heremans. "High Pressure Effects on Proteins and other Biomolecules". In: *Annual Review of Biophysics and Bioengineering* 11.1 (1982). PMID: 7049058, pp. 1–21. DOI: 10.1146/annurev.bb.11.060182.000245 (cit. on p. 1).

[16] Michael Gross and Rainer Jaenicke. "Proteins under pressure". In: *European Journal of Biochemistry* 221.2 (1994), pp. 617–630. ISSN: 1432-1033. DOI: 10.1111/j.1432-1033.1994.tb18774.x (cit. on p. 1).

[17] Claude Balny, Patrick Masson, and Karel Heremans. "High pressure effects on biological macromolecules: from structural changes to alteration of cellular processes". In: *Biochimica et Biophysica Acta (BBA) - Protein Structure and Molecular Enzymology* 1595.1-2 (2002), pp. 3–10. ISSN: 0167-4838. DOI: 10.1016/S0167-4838(01)00331-4 (cit. on p. 1).

[18] R. Winter and W. Dzwolak. "Exploring the temperature-pressure configurational landscape of biomolecules: from lipid membranes to proteins". In: *Philosophical Transactions of the Royal Society A: Mathematical,Physical and Engineering Sciences* 363.1827 (2005), pp. 537–563. DOI: 10.1098/rsta.2004.1507 (cit. on p. 1).

[19] N. K. Rastogi et al. "Opportunities and Challenges in High Pressure Processing of Foods". In: *Critical Reviews in Food Science and Nutrition* 47.1 (2007). PMID: 17364696, pp. 69–112. DOI: 10.1080/10408390600626420 (cit. on p. 1).

[20] M. S. Kuster et al. "Joint load considerations in total knee replacement". In: *Journal of Bone and Joint Surgery, British Volume* 79-B.1 (1997), pp. 109–113. DOI: 10.1302/0301-620X.79B1.6978 (cit. on p. 1).

[21] ManuelaT. Raimondi and Riccardo Pietrabissa. "Contact pressures at grafted cartilage lesions in the knee". English. In: *Knee Surgery, Sports Traumatology, Arthroscopy* 13 (6 2005), pp. 444–450. ISSN: 0942-2056. DOI: 10.1007/s00167-004-0529-1 (cit. on p. 1).

[22] Nolwennig Rivalain, Jean Roquain, and Gérard Demazeau. "Development of high hydrostatic pressure in biosciences: Pressure effect on biological structures and potential applications in Biotechnologies". In: *Biotechnology Advances* 28.6 (2010), pp. 659–672. ISSN: 0734-9750. DOI: 10.1016/j.biotechadv.2010.04.001 (cit. on p. 1).

[23] Katsuto Otake et al. “Pressure effects on the aggregation of poly(N-isopropylacrylamide) and poly(N-isopropylacrylamide-co-acrylic acid) in aqueous solutions”. In: *Macromolecules* 26.9 (1993), pp. 2194–2197. DOI: 10.1021/ma00061a008 (cit. on pp. 2, 3).

[24] S. Kunugi et al. “Effects of Pressure on the Behavior of the Thermoresponsive Polymer Poly(N-vinylisobutyramide) (PNVIBA)”. In: *Macromolecules* 30.15 (1997), pp. 4499–4501. DOI: 10.1021/ma961770r (cit. on pp. 2, 3).

[25] Mitsuhiro Shibayama et al. “SANS Study on Pressure-Induced Phase Separation of Poly(N-isopropylacrylamide) Aqueous Solutions and Gels”. In: *Macromolecules* 37.8 (2004), pp. 2909–2918. DOI: 10.1021/ma0359685 (cit. on pp. 2, 3).

[26] Eiji Kato. “Thermodynamic study of a pressure-temperature phase diagram for poly(N-isopropylacrylamide) gels”. In: *Journal of Applied Polymer Science* 97.1 (2005), pp. 405–412. ISSN: 1097-4628. DOI: 10.1002/app.21764 (cit. on pp. 2, 3, 11, 81).

[27] Els Loozen et al. “The Influence of Pressure on the Lower Critical Solution Temperature Miscibility Behavior of Aqueous Solutions of Poly(vinyl methyl ether) and the Relation to the Compositional Curvature of the Volume of Mixing”. In: *The Journal of Physical Chemistry B* 110.15 (2006). PMID: 16610875, pp. 7793–7802. DOI: 10.1021/jp0574854 (cit. on pp. 2, 3).

[28] Juan-Jose Lietor-Santos et al. “Deswelling Microgel Particles Using Hydrostatic Pressure”. In: *Macromolecules* 42.16 (2009), pp. 6225–6230. DOI: 10.1021/ma9010654 (cit. on p. 2).

[29] Matthias Pühse et al. “Influence of pressure on the state of poly(N-isopropylacrylamide) and poly(N,N-diethylacrylamide) derived polymers in aqueous solution as probed by FTIR-spectroscopy”. In: *Polymer* 51.16 (2010), pp. 3653–3659. ISSN: 0032-3861. DOI: 10.1016/j.polymer.2010.06.011 (cit. on pp. 2, 3, 81).

[30] Juan Jose Lietor-Santos et al. “The effect of hydrostatic pressure over the swelling of microgel particles”. In: *Soft Matter* 7 (14 2011), pp. 6370–6374. DOI: 10.1039/C1SM05328K (cit. on p. 2).

[31] C. E. Miller et al. “Characterization of Biological Thin Films at the Solid-Liquid Interface by X-Ray Reflectivity”. In: *Phys. Rev. Lett.* 94 (23 June 2005), p. 238104. DOI: 10.1103/PhysRevLett.94.238104 (cit. on p. 2).

[32] Martin Kreuzer et al. “Pressure cell for investigations of solid–liquid interfaces by neutron reflectivity”. In: *Review of Scientific Instruments* 82.2, 023902 (2011), p. 023902. DOI: 10.1063/1.3505797 (cit. on pp. 2, 33, 35).

[33] Christoph Jeworrek et al. “High pressure cell for neutron reflectivity measurements up to 2500 bar”. In: *Review of Scientific Instruments* 82.2, 025106 (2011), p. 025106. DOI: 10.1063/1.3553392 (cit. on p. 2).

[34] P. Wang et al. “High-pressure and high-temperature neutron reflectometry cell for solid-fluid interface studies”. English. In: *The European Physical Journal Plus* 127 (7 2012), pp. 1–15. DOI: 10.1140/epjp/i2012-12076-0 (cit. on p. 2).

[35] Debora Foguel et al. “Hydrostatic pressure rescues native protein from aggregates”. In: *Biotechnology and Bioengineering* 63.5 (1999), pp. 552–558. ISSN: 1097-0290. DOI: 10.1002/(SICI)1097-0290(19990605)63:5<552::AID-BIT5>3.0.CO;2-8 (cit. on p. 2).

[36] Theodore W. Randolph, Matthew Seefeldt, and John F. Carpenter. “High hydrostatic pressure as a tool to study protein aggregationand amyloidosis”. In: *Biochimica et Biophysica Acta (BBA) - Protein Structure and Molecular Enzymology* 1595.1-2 (2002), pp. 224–234. ISSN: 0167-4838. DOI: 10.1016/S0167-4838(01)00346-6 (cit. on p. 2).

[37] Christian Reichhart and Claus Czeslik. “Native-like Structure of Proteins at a Planar Poly(acrylic acid) Brush”. In: *Langmuir* 25.2 (2009), pp. 1047–1053. DOI: 10.1021/la802905s (cit. on pp. 2, 3, 61, 63).

[38] Alexander Wittemann and Matthias Ballauff. “Secondary Structure Analysis of Proteins Embedded in Spherical Polyelectrolyte Brushes by FT-IR Spectroscopy”. In: *Analytical Chemistry* 76.10 (2004). PMID: 15144192, pp. 2813–2819. DOI: 10.1021/ac0354692 (cit. on pp. 2, 3, 61, 63).

[39] A. Wittemann, B. Haupt, and M. Ballauff. “Adsorption of proteins on spherical polyelectrolyte brushes in aqueous solution”. In: *Phys. Chem. Chem. Phys.* 5 (8 2003), pp. 1671–1677. DOI: 10.1039/B300607G (cit. on pp. 2, 57, 58).

[40] Claus Czeslik et al. “Protein Binding to Like-Charged Polyelectrolyte Brushes by Counterion Evaporation”. In: *The Journal of Physical Chemistry B* 108.35 (2004), pp. 13395–13402. DOI: 10.1021/jp0488766 (cit. on pp. 2, 40, 47, 56–58).

[41] Oliver Hollmann and Claus Czeslik. “Characterization of a Planar Poly(acrylic acid) Brush as a Materials Coating for Controlled Protein Immobilization”. In: *Langmuir* 22.7 (2006), pp. 3300–3305. DOI: 10.1021/la053110y (cit. on pp. 2, 3).

[42] A. Wittemann et al. “Interaction of dissolved proteins with spherical polyelectrolyte brushes”. In: *Macromolecular Symposia* 191.1 (2003), pp. 81–88. ISSN: 1521-3900. DOI: 10.1002/masy.200390017 (cit. on p. 2).

[43] S. Rosenfeldt et al. “Interaction of proteins with spherical polyelectrolyte brushes in solution as studied by small-angle x-ray scattering”. In: *Phys. Rev. E* 70 (6 Dec. 2004), p. 061403. DOI: 10.1103/PhysRevE.70.061403 (cit. on pp. 2, 57, 63).

[44] Katja Henzler et al. “Directed Motion of Proteins along Tethered Polyelectrolytes”. In: *Phys. Rev. Lett.* 100 (15 Apr. 2008), p. 158301. DOI: 10.1103/PhysRevLett.100.158301 (cit. on pp. 2, 63).

[45] Jinhua Dai et al. “High-Capacity Binding of Proteins by Poly(Acrylic Acid) Brushes and Their Derivatives”. In: *Langmuir* 22.9 (2006), pp. 4274–4281. DOI: 10.1021/la0600550 (cit. on p. 2).

[46] Oliver Hollmann, Thomas Gutberlet, and Claus Czeslik. “Structure and Protein Binding Capacity of a Planar PAA Brush”. In: *Langmuir* 23.3 (2007), pp. 1347–1353. DOI: 10.1021/la061881b (cit. on pp. 2, 40, 47, 57).

[47] Wiebe M. de Vos et al. "Adsorption of the Protein Bovine Serum Albumin in a Planar Poly(acrylic acid) Brush Layer As Measured by Optical Reflectometry". In: *Langmuir* 24.13 (2008). PMID: 18507422, pp. 6575–6584. DOI: 10.1021/la8006469 (cit. on pp. 2, 57, 58).

[48] Oliver Hollmann, Christian Reichhart, and Claus Czeslik. "Kinetics of Protein Adsorption at a Poly(Acrylic Acid) Brush Studied by Surface Plasmon Resonance Spectroscopy". In: *Zeitschrift für Physikalische Chemie* 222.1 (Jan. 2008), pp. 205–215. ISSN: 0942-9352. DOI: 10.1524/zpch.2008.222.1.205 (cit. on pp. 2, 57, 58).

[49] Eva Bittrich et al. "Protein adsorption on and swelling of polyelectrolyte brushes: A simultaneous ellipsometry-quartz crystal microbalance study". English. In: *Biointerphases* 5.4 (2010), pp. 159–167. ISSN: 1934-8630. DOI: 10.1116/1.3530841 (cit. on pp. 2, 57).

[50] Oliver Hollmann, Roland Steitz, and Claus Czeslik. "Structure and dynamics of [small alpha]-lactalbumin adsorbed at a charged brush interface". In: *Phys. Chem. Chem. Phys.* 10 (10 2008), pp. 1448–1456. DOI: 10.1039/B716264B (cit. on pp. 3, 51).

[51] B. Haupt et al. "Activity of Enzymes Immobilized in Colloidal Spherical Polyelectrolyte Brushes". In: *Biomacromolecules* 6.2 (2005), pp. 948–955. DOI: 10.1021/bm0493584 (cit. on p. 3).

[52] Mingming Zhang et al. "Double-responsive polymer brushes on the surface of colloid particles". In: *Journal of Colloid and Interface Science* 301.1 (2006), pp. 85–91. ISSN: 0021-9797. DOI: 10.1016/j.jcis.2006.05.004 (cit. on p. 3).

[53] Felix A. Plamper et al. "Tuning the Thermoresponsive Properties of Weak Polyelectrolytes: Aqueous Solutions of Star-Shaped and Linear Poly(N,N-dimethylaminoethyl Methacrylate)". In: *Macromolecules* 40.23 (2007), pp. 8361–8366. DOI: 10.1021/ma071203b (cit. on pp. 3, 74, 84, 89, 95, 97).

[54] Eiji Kato. "Volume-phase transition of N-isopropylacrylamide gels induced by hydrostatic pressure". In: *The Journal of Chemical Physics* 106.9 (1997), pp. 3792–3797. DOI: 10.1063/1.473432 (cit. on p. 3).

[55] W. Kauzmann. "Some Factors in the Interpretation of Protein Denaturation". In: ed. by Kenneth Bailey C.B. Anfinsen M.L. Anson and John T. Edsall. Vol. 14. Advances in Protein Chemistry. Academic Press, 1959, pp. 1–63. DOI: 10.1016/S0065-3233(08)60608-7 (cit. on p. 3).

[56] Gerhard Hummer et al. "The pressure dependence of hydrophobic interactions is consistent with the observed pressure denaturation of proteins". In: *Proceedings of the National Academy of Sciences* 95.4 (1998), pp. 1552–1555. DOI: 10.1073/pnas.95.4.1552 (cit. on pp. 3, 11, 81).

[57] Julien Roche et al. "Cavities determine the pressure unfolding of proteins". In: *Proceedings of the National Academy of Sciences* 109.18 (2012), pp. 6945–6950. DOI: 10.1073/pnas.1200915109 (cit. on pp. 3, 11).

[58] Cristiano L. Dias. "Unifying Microscopic Mechanism for Pressure and Cold Denaturations of Proteins". In: *Phys. Rev. Lett.* 109 (4 July 2012), p. 048104. DOI: 10.1103/PhysRevLett.109.048104 (cit. on pp. 3, 11).

[59] P.J. Flory. *Principles of polymer chemistry*. Cornell University Press, 1953. ISBN: 9780801401343 (cit. on pp. 5, 7, 9).

[60] P.G. de Gennes et al. "Remarks on polyelectrolyte conformation". In: *J. Phys. France* 37.12 (1976), pp. 1461–1473. DOI: 10.1051/jphys:0197600370120146100 (cit. on p. 7).

[61] P. G. de Gennes. "Conformations of Polymers Attached to an Interface". In: *Macromolecules* 13.5 (1980), pp. 1069–1075. DOI: 10.1021/ma60077a009 (cit. on p. 7).

[62] S. Alexander. "Polymer adsorption on small spheres. A scaling approach". In: *J. Phys. France* 38.8 (1977), pp. 977–981. DOI: 10.1051/jphys:0197700380809700 (cit. on p. 7).

[63] S. T. Milner, T. A. Witten, and M. E. Cates. "A Parabolic Density Profile for Grafted Polymers". In: *Europhysics Letters* 5.5 (1988), p. 413. DOI: 10.1209/0295-5075/5/5/006 (cit. on p. 7).

[64] S. T. Milner, T. A. Witten, and M. E. Cates. "Theory of the grafted polymer brush". In: *Macromolecules* 21.8 (1988), pp. 2610–2619. DOI: 10.1021/ma00186a051 (cit. on pp. 7, 40).

[65] Philip Pincus. "Colloid stabilization with grafted polyelectrolytes". In: *Macromolecules* 24.10 (1991), pp. 2912–2919. DOI: 10.1021/ma00010a043 (cit. on p. 8).

[66] O. V. Borisov, E. B. Zhulina, and T. M. Birshtein. "Diagram of the States of a Grafted Polyelectrolyte Layer". In: *Macromolecules* 27.17 (1994), pp. 4795–4803. DOI: 10.1021/ma00095a021 (cit. on p. 8).

[67] Yu. V. Lyatskaya et al. "Analytical Self-Consistent-Field Model of Weak Polyacid Brushes". In: *Macromolecules* 28.10 (1995), pp. 3562–3569. DOI: 10.1021/ma00114a009 (cit. on p. 8).

[68] E. B. Zhulina and O. V. Borisov. "Poisson-Boltzmann Theory of pH-Sensitive (Annealing) Polyelectrolyte Brush". In: *Langmuir* 27.17 (2011), pp. 10615–10633. DOI: 10.1021/la201456a (cit. on pp. 8, 51–54).

[69] Roland R. Netz and M. Schick. "Polymer Brushes: From Self-Consistent Field Theory to Classical Theory". In: *Macromolecules* 31.15 (1998), pp. 5105–5122. DOI: 10.1021/ma9717505 (cit. on pp. 8, 10, 51).

[70] Matthias Ballauff and Oleg Borisov. "Polyelectrolyte brushes". In: *Current Opinion in Colloid & Interface Science* 11.6 (2006), pp. 316–323. ISSN: 1359-0294. DOI: 10.1016/j.cocis.2006.12.002 (cit. on p. 8).

[71] M. Reinhardt et al. "Fine-tuning the structure of stimuli-responsive polymer films by hydrostatic pressure". In: *submitted to Macromolecules* (2013) (cit. on p. 9).

[72] F. Th. Hesselink. "Density distribution of segments of a terminally adsorbed macromolecule". In: *The Journal of Physical Chemistry* 73.10 (1969), pp. 3488–3490. DOI: 10.1021/j100844a061 (cit. on p. 10).

[73] Edmund A. DiMarzio and Frank L. McCrackin. “One-Dimensional Model of Polymer Adsorption”. In: *The Journal of Chemical Physics* 43.2 (1965), pp. 539–547. DOI: 10.1063/1.1696778 (cit. on pp. 10, 51, 54).

[74] A. Karim et al. “Neutron Reflectivity Study of the Density Profile of a Model End-Grafted Polymer Brush: Influence of Solvent Quality”. In: *Phys. Rev. Lett.* 73 (25 Dec. 1994), pp. 3407–3410. DOI: 10.1103/PhysRevLett.73.3407 (cit. on pp. 13, 51).

[75] P. Auroy, Y. Mir, and L. Auvray. “Local structure and density profile of polymer brushes”. In: *Phys. Rev. Lett.* 69 (1 July 1992), pp. 93–95. DOI: 10.1103/PhysRevLett.69.93 (cit. on pp. 13, 51).

[76] Felix Schacher et al. “New Block Copolymers with Poly(N,N-dimethylaminoethyl methacrylate) as a Double Stimuli-Responsive Block”. In: *Macromolecular Chemistry and Physics* 210.3-4 (2009), pp. 256–262. ISSN: 1521-3935. DOI: 10.1002/macp.200800557 (cit. on p. 15).

[77] Dirk W. Schubert and Thomas Dunkel. “Spin coating from a molecular point of view: its concentration regimes, influence of molar mass and distribution”. English. In: *Materials Research Innovations* 7 (5 2003), pp. 314–321. ISSN: 1432-8917. DOI: 10.1007/s10019-003-0270-2 (cit. on p. 17).

[78] G. Roberts. *Langmuir-Blodgett Films*. Springer, 1990. ISBN: 9780306433160 (cit. on p. 19).

[79] J. Daillant and A. Gibaud, eds. *X-ray and Neutron Reflectivity*. Lecture Notes in Physics Vol. 770. Springer Berlin Heidelberg, 2009. DOI: 10.1007/978-3-540-88588-7 (cit. on pp. 20, 25).

[80] R. Steitz. “Lecture notes on Reflectivity and GISAS”. In: *32. Berlin Neutron School*. Helmholtz-Zentrum Berlin. 2012 (cit. on p. 20).

[81] Varley F. Sears. “Neutron scattering lengths and cross sections”. In: *Neutron News* 3.3 (1992), pp. 26–37. DOI: 10.1080/10448639208218770 (cit. on pp. 21, 32, 41).

[82] L. Névot and P. Croce. “Caractérisation des surfaces par réflexion rasante de rayons X. Application à l’étude du polissage de quelques verres silicates”. In: *Rev. Phys. Appl. (Paris)* 15.3 (1980), pp. 761–779. DOI: 10.1051/rphysap:01980001503076100 (cit. on p. 26).

[83] L. G. Parratt. “Surface Studies of Solids by Total Reflection of X-Rays”. In: *Phys. Rev.* 95 (2 July 1954), pp. 359–369. DOI: 10.1103/PhysRev.95.359 (cit. on p. 27).

[84] F. Abeles. “La détermination de l’indice et de l’épaisseur des couches minces transparentes”. In: *J. Phys. Radium* 11.7 (1950), pp. 310–314. DOI: 10.1051/jphysrad:01950001107031000 (cit. on pp. 28, 41).

[85] F. Mezei et al. “Focussed beam reflectometer for solid and liquid surfaces”. In: *Physica B: Condensed Matter* 213–214 (1995), pp. 898–900. ISSN: 0921-4526. DOI: 10.1016/0921-4526(95)00317-3 (cit. on pp. 29, 107).

[86] M. Strobl et al. “BioRef: A versatile time-of-flight reflectometer for soft matter applications at Helmholtz–Zentrum Berlin”. In: *Review of Scientific Instruments* 82.5, 055101 (2011), p. 055101. DOI: 10.1063/1.3581210 (cit. on p. 30).

[87] James E. Mark. *Polymer data handbook*. Oxford University Press, 1999. ISBN: 0195107896 (alk. paper) (cit. on pp. 32, 40, 41, 44, 52).

[88] Tadanori Koga et al. “The Role of Elasticity in the Anomalous Swelling of Polymer Thin Films in Density Fluctuating Supercritical Fluids”. In: *Macromolecules* 36.14 (2003), pp. 5236–5243. DOI: 10.1021/ma021265w (cit. on p. 33).

[89] Jonathan R. Howse et al. “Critical adsorption and boundary layer structure of 2-butoxyethanol + D_2O mixtures at a hydrophilic silica surface”. In: *The Journal of Chemical Physics* 116.16 (2002), pp. 7177–7188. DOI: 10.1063/1.1463398 (cit. on p. 34).

[90] Mukul Gupta et al. “AMOR - the time-of-flight neutron reflectometer at SINQ/PSI”. English. In: *Pramana* 63.1 (2004), pp. 57–63. ISSN: 0304-4289. DOI: 10.1007/BF02704051 (cit. on pp. 35, 105).

[91] E. P. K. Currie et al. “Weak Polyacid Brushes: Preparation by LB Deposition and Optically Detected Titrations”. In: *Langmuir* 15.21 (1999), pp. 7116–7118. DOI: 10.1021/la990689p (cit. on p. 37).

[92] Y. Tran, P. Auroy, and L-T. Lee. “Determination of the Structure of Polyelectrolyte Brushes”. In: *Macromolecules* 32.26 (1999), pp. 8952–8964. DOI: 10.1021/ma990443r (cit. on p. 40).

[93] Andrew Nelson. “Co-refinement of multiple-contrast neutron/X-ray reflectivity data using *MOTOFIT*”. In: *Journal of Applied Crystallography* 39.2 (Apr. 2006), pp. 273–276. DOI: 10.1107/S0021889806005073 (cit. on p. 41).

[94] T.P. Russell. “On the reflectivity of polymers: Neutrons and X-rays”. In: *Physica B: Condensed Matter* 221.1–4 (1996). Proceedings of the Fourth International Conference on Surface X-ray and Neutron Scatterin, pp. 267–283. ISSN: 0921-4526. DOI: 10.1016/0921-4526(95)00937-X (cit. on p. 41).

[95] R. W. Warfield. “Compressibility of bulk polymers”. In: *Polymer Engineering & Science* 6.2 (1966), pp. 176–180. ISSN: 1548-2634. DOI: 10.1002/pen.760060216 (cit. on pp. 45, 83).

[96] A. Quach and Robert Simha. “Pressure-Volume-Temperature Properties and Transitions of Amorphous Polymers; Polystyrene and Poly (orthomethylstyrene)”. In: *Journal of Applied Physics* 42.12 (1971), pp. 4592–4606. DOI: 10.1063/1.1659828 (cit. on pp. 45, 83).

[97] Daniel C. Carter and Joseph X. Ho. “Structure of Serum-Albumin”. English. In: *Advances in Protein Chemistry*. Vol. 45. Advances in Protein Chemistry. Academic Press Inc, 1994, pp. 153–203 (cit. on pp. 47, 48, 60, 63).

[98] J. F. J. Dippy, S. R. C. Hughes, and A. Rozanski. “498. The dissociation constants of some symmetrically disubstituted succinic acids”. In: *J. Chem. Soc.* (1959), pp. 2492–2498. DOI: 10.1039/JR9590002492 (cit. on p. 52).

[99] Tohru Miyajima et al. “On the Complexation of Cd(II) Ions with Polyacrylic Acid”. In: *Journal of Colloid and Interface Science* 184.1 (1996), pp. 279–288. ISSN: 0021-9797. DOI: 10.1006/jcis.1996.0621 (cit. on p. 52).

[100] Roland Steitz et al. “Nanobubbles and Their Precursor Layer at the Interface of Water Against a Hydrophobic Substrate”. In: *Langmuir* 19.6 (2003), pp. 2409–2418. DOI: 10.1021/la026731p (cit. on p. 54).

[101] Hideki Matsuoka et al. “Critical Brush Density for the Transition between Carpet-Only and Carpet/Brush Double-Layered Structures. 2. Hydrophilic Chain Length Dependence”. In: *Macromolecules* 40.3 (2007), pp. 766–769. DOI: 10.1021/ma061789m (cit. on pp. 54, 55).

[102] H. Yim et al. “Conformation of End-Tethered PNIPAM Chains in Water and in Acetone by Neutron Reflectivity”. In: *Macromolecules* 36.14 (2003), pp. 5244–5251. DOI: 10.1021/ma021548o (cit. on p. 55).

[103] Hideki Matsuoka et al. “Critical Brush Density for the Transition between Carpet-Only and Carpet/Brush Double-Layered Structures”. In: *Langmuir* 21.15 (2005), pp. 6842–6845. DOI: 10.1021/la047188a (cit. on p. 55).

[104] Katja Henzler et al. “Adsorption of beta-Lactoglobulin on Spherical Polyelectrolyte Brushes: Direct Proof of Counterion Release by Isothermal Titration Calorimetry”. In: *Journal of the American Chemical Society* 132.9 (2010). PMID: 20143809, pp. 3159–3163. DOI: 10.1021/ja909938c (cit. on pp. 56, 57).

[105] Rex M. C. Dawson, D.C. Elliott, and W.H. Elliott. *Data for Biochemical Research*. Oxford Science Publications. Clarendon Press, 1989. ISBN: 9780198552994 (cit. on p. 57).

[106] P. Maarten Biesheuvel and Alexander Wittemann. “A Modified Box Model Including Charge Regulation for Protein Adsorption in a Spherical Polyelectrolyte Brush”. In: *The Journal of Physical Chemistry B* 109.9 (2005), pp. 4209–4214. DOI: 10.1021/jp0452812 (cit. on p. 57).

[107] P. Maarten Biesheuvel, Frans A. M. Leermakers, and Martien A. Cohen Stuart. “Self-consistent field theory of protein adsorption in a non-Gaussian polyelectrolyte brush”. In: *Phys. Rev. E* 73 (1 Jan. 2006), p. 011802. DOI: 10.1103/PhysRevE.73.011802 (cit. on p. 57).

[108] Katja Henzler et al. “Adsorption of beta-Lactoglobulin on Spherical Polyelectrolyte Brushes: Direct Proof of Counterion Release by Isothermal Titration Calorimetry”. In: *Journal of the American Chemical Society* 132.9 (2010). PMID: 20143809, pp. 3159–3163. DOI: 10.1021/ja909938c (cit. on p. 57).

[109] A. Halperin. “Polymer Brushes that Resist Adsorption of Model Proteins: Design Parameters”. In: *Langmuir* 15.7 (1999), pp. 2525–2533. DOI: 10.1021/la981356f (cit. on pp. 60, 63).

[110] M. Luisa Ferrer et al. “The Conformation of Serum Albumin in Solution: A Combined Phosphorescence Depolarization-Hydrodynamic Modeling Study”. In: *Biophysical Journal* 80.5 (2001), pp. 2422–2430. ISSN: 0006-3495. DOI: 10.1016/S0006-3495(01)76211-X (cit. on p. 60).

[111] F. Luis Gonzalez Flecha and Valeria Levi. “Determination of the molecular size of BSA by fluorescence anisotropy”. In: *Biochemistry and Molecular Biology Education* 31.5 (2003), pp. 319–322. ISSN: 1539-3429. DOI: 10.1002/bmb.2003.494031050261 (cit. on p. 60).

[112] D. Goodsell. “Serum Albumin - Molecule of the Month January 2003”. In: *RCSB Protein Data Base* (2003) (cit. on p. 60).

[113] Isao Hayakawa et al. “Denaturation of Bovine Serum Albumin (BSA) and Ovalbumin by High Pressure, Heat and Chemicals”. In: *Journal of Food Science* 57.2 (1992), pp. 288–292. ISSN: 1750-3841. DOI: 10.1111/j.1365-2621.1992.tb05478.x (cit. on p. 65).

[114] Arthur K. Covington et al. “Use of the glass electrode in deuterium oxide and the relation between the standardized pD (paD) scale and the operational pH in heavy water”. In: *Analytical Chemistry* 40.4 (1968), pp. 700–706. DOI: 10.1021/ac60260a013 (cit. on p. 70).

[115] S. W. An et al. “Structure of a Diblock Copolymer Adsorbed at the Hydrophobic Solid/Aqueous Interface: Effects of Charge Density on a Weak Polyelectrolyte Brush”. In: *Macromolecules* 32.8 (1999), pp. 2731–2738. DOI: 10.1021/ma981146+ (cit. on p. 72).

[116] G Hummer et al. “An information theory model of hydrophobic interactions”. In: *Proceedings of the National Academy of Sciences* 93.17 (1996), pp. 8951–8955. DOI: 10.1073/pnas.93.17.8951 (cit. on p. 81).

[117] Wely Brasil Floriano and Marco Antonio Chaer Nascimento. “Dielectric constant and density of water as a function of pressure at constant temperature”. en. In: *Brazilian Journal of Physics* 34 (Mar. 2004), pp. 38–41. ISSN: 0103-9733. DOI: 10.1590/S0103-97332004000100006 (cit. on p. 83).

[118] D.R. Lide. *Handbook of Chemistry and Physics: 2000-2001 : a Ready-reference Book of Chemical and Physical Data*. CRC Handbook of Chemistry & Physics. CRC Press, 2000. ISBN: 9780849304811 (cit. on p. 83).

[119] J.A. Schellman. “Temperature, stability, and the hydrophobic interaction”. In: *Biophysical Journal* 73.6 (1997), pp. 2960–2964. ISSN: 0006-3495. DOI: 10.1016/S0006-3495(97)78324-3 (cit. on p. 88).

[120] Susanna Lüdemann et al. “The Temperature-Dependence of Hydrophobic Association in Water. Pair versus Bulk Hydrophobic Interactions”. In: *Journal of the American Chemical Society* 119.18 (1997), pp. 4206–4213. DOI: 10.1021/ja953439d (cit. on p. 88).

[121] Seishi Shimizu and Hue Sun Chan. “Temperature dependence of hydrophobic interactions: A mean force perspective, effects of water density, and nonadditivity of thermodynamic signatures”. In: *The Journal of Chemical Physics* 113.11 (2000), pp. 4683–4700. DOI: 10.1063/1.1288922 (cit. on p. 88).

[122] L.E. Reichl. *A Modern Course in Statistical Physics*. Physics Textbook. Wiley, 2009. ISBN: 9783527407828 (cit. on p. 88).

[123] A. Mulero. *Theory and Simulation of Hard-Sphere Fluids and Related Systems*. Lecture Notes in Physics. Springer, 2008. ISBN: 9783540787662. DOI: 10.1007/978-3-540-78767-9 (cit. on p. 89).

[124] Vladimir A. Baulin, Ekaterina B. Zhulina, and Avi Halperin. "Self-consistent field theory of brushes of neutral water-soluble polymers". In: *The Journal of Chemical Physics* 119.20 (2003), pp. 10977–10988. DOI: 10.1063/1.1619934 (cit. on p. 90).

[125] H. Yim et al. "Evidence for vertical phase separation in densely grafted, high-molecular-weight poly(*N*-isopropylacrylamide) brushes in water". In: *Phys. Rev. E* 72 (5 Nov. 2005), p. 051801. DOI: 10.1103/PhysRevE.72.051801 (cit. on p. 90).

[126] Xavier Laloyaux et al. "Surface and Bulk Collapse Transitions of Thermoresponsive Polymer Brushes". In: *Langmuir* 26.2 (2010). PMID: 19842635, pp. 838–847. DOI: 10.1021/la902285t (cit. on p. 90).

[127] Hoyoung Lee et al. "A Discussion of the pH-Dependent Protonation Behaviors of Poly(2-(dimethylamino)ethyl methacrylate) (PDMAEMA) and Poly(ethylenimine-ran-2-ethyl-2-oxazoline) (P(EI-r-EOz))". In: *The Journal of Physical Chemistry B* 115.5 (2011), pp. 844–860. DOI: 10.1021/jp109151s (cit. on p. 95).

[128] Felix A. Plamper et al. "Synthesis, Characterization and Behavior in Aqueous Solution of Star-Shaped Poly(acrylic acid)". In: *Macromolecular Chemistry and Physics* 206.18 (2005), pp. 1813–1825. ISSN: 1521-3935. DOI: 10.1002/macp.200500238 (cit. on p. 97).

[129] Florian Rehfeldt et al. "Reversible Activation of Diblock Copolymer Monolayers at the Interface by pH Modulation, 1: Lateral Chain Density and Conformation". In: *The Journal of Physical Chemistry B* 110.18 (2006). PMID: 16671730, pp. 9171–9176. DOI: 10.1021/jp054532j (cit. on p. 105).

[130] Ilja K. Voets et al. "Internal Structure of a Thin Film of Mixed Polymeric Micelles on a Solid/Liquid Interface". In: *The Journal of Physical Chemistry B* 112.23 (2008). PMID: 18489139, pp. 6937–6945. DOI: 10.1021/jp709758p (cit. on pp. 105, 107).

[131] D. Richard, M. Ferrand, and G. J. Kearley. "Analysis and visualisation of neutron-scattering data". In: *Journal of Neutron Research* 4.1-4 (1996), pp. 33–39. DOI: 10.1080/10238169608200065 (cit. on p. 107).

List of Figures